Faculty of Mathematics and Physics
Charles University in Prague

HABILITATION THESIS

RNDr. Zdeněk Futera, Ph.D.

Computational Approaches to Electron Transfer Processes: From Ionic Solutions to Nanobioelectronic Devices

Prague 2023

Computational Approaches to Electron Transfer Processes:
From Ionic Solutions to Nanobioelectronic Devices

Habilitation Thesis

Zdeněk Futera
Prague 2023

zfutera@prf.jcu.cz

University of South Bohemia
Faculty of Science
Department of Physics
Branišovská 1760
370 05 České Budějovice

Acknowledgments

I would like to express my thanks and gratitude to my academic mentor Prof. Jochen Blumberger who has greatly inspired me and motivated me in research of charge transfer phenomena. Special thanks go to my family, especially my wife Ola, for all the support.

Contents

Preface

The habilitation thesis presents the development and application of advanced computational techniques used for the investigation of charge transfer processes by means of computer simulations, in particular for biologically relevant systems. The author studied this research area during his postdoctoral stays at the National Institute for Materials Sciences (NIMS) in Japan, University College Dublin (UCD) in Ireland, and University College London (UCL) in the United Kingdom, and further elaborated at the Faculty of Science of the University of South Bohemia (USB) in České Budějovice, where he recently established his research group after returning to the Czech Republic. The main achievements in this research field are demonstrated by collections of representative articles published in international scientific journals during the last ten years.

The charge transfer, in general, can proceed by very different mechanisms. The author, motivated by his interest in quantum phenomena in soft matter, focuses predominantly on electronic transitions in molecular systems. These are typically realized by incoherent hopping events, like in redox-active proteins, which can be computationally simulated by hybrid quantum-mechanical/molecular-mechanical (QM/MM) approaches and statistical techniques based on molecular dynamics (MD). However, the situation becomes more complex when the molecules get in touch with electrified metal surfaces, like at solid/liquid interfaces in electrochemistry or protein junctions in nanobioelectronic devices. These interactions can dramatically change the electronic behavior of the molecules and the transport mechanism as well. Coherent tunneling, usual for charge transfer in solid matter, plays a more important role on such interfaces, requiring full-quantum computational descriptions, typically based on density functional theory (DFT).

The theory of (in)coherent electron transfer (ET) is briefly reviewed in the first part of the thesis, together with the computational approaches and techniques suitable for their investigation. Then, the author demonstrates the applicability and performance of these methods in several case examples. Special focus is given to biologically relevant problems such as the ergodicity of ET in redox proteins, long-range ET efficiency in redox chains, interactions of biomolecules with metal electrodes, and tunneling conductance of protein junctions. Other applications, such as redox-state transitions in solvated molecules, electronic transfer on solvated semiconductor electrode interfaces, or external-field-induced superionic transitions in ice systems, are mentioned in the last part of the thesis. The thesis is supplemented by reprints of the author's 14 most relevant scientific articles on the presented research topic.

1 Introduction

Charge transfer reactions are ubiquitous not only in chemistry, industry, and electronic technologies but also in biology. For example, photosynthesis, respiration cycle, and nitrogen fixation are just the most famous natural processes maintained by living cells, where the electronic charges are transferred through complex redox cascades to support other chemical reactions [1–12]. The charge transfer is mediated by redox-active proteins like cytochromes or cupredoxins, which have suitable electronic structures to trap and release electrons, and it is further supported by various organic compounds shuttling the charge between such proteins. In contrast to inorganic solid-state matter, the range of biomolecular structures is much richer, more flexible, and more complex.

In biology, electrons typically localize on an available redox site until they gain enough energy from the molecular thermal movements to overcome a free energy barrier and transfer to another place [11,13–15]. This mechanism is known as incoherent hopping [16]. The resident time of the electrons is often long enough to allow complete relaxation of the redox site and its neighborhood to a changed electrostatic potential upon the electron transfer event. The free energy connected with such relaxation, together with the energy differences between the related sites, determines the barrier preventing the hops, and so the kinetics of the overall process. Biomolecules such as redox proteins are usually optimized by evolution to allow efficient electron transfer over long-range distances [6,13,17] They often utilize transition metals and aromatic organic cofactors in their redox sites to tune the electronic-state positions and couplings.

However, experimental detection of individual hopping events in native biomolecules is challenging. Typically, protein must be labeled by suitable organic dye near the specific redox site, which is then used for controlled electron injection during ultrafast transient spectroscopy measurements, known as pump-probe [18–21] More often, biomolecular redox properties are studied by electrochemical approaches [22–24], which are less specific but easier to perform. For example, in protein film voltammetry [25–28], an electric current-voltage (I-V) response is probed on a monolayer of proteins adsorbed on the electrode surface in solution. The specific shape of the resulting I-V curves contains information about redox site energies and transfer kinetics, averaged over all the involved proteins. Nevertheless, electronic interactions of the probed proteins with the metallic electrode states and the external electric fields present during the measurements can affect the molecular properties and the transfer mechanism in a considerable way.

Single-molecular probe techniques have recently been developed, allowing measurements of current-voltage characteristics on individual peptides and proteins [29–33]. These

methods are based on scanning tunneling microscopy (STM) or conductive atomic force microscopy (AFM) [34], where the probed molecule is adsorbed on an electrode substrate, and the current is measured via a sharp metal tip approaching the molecule from the other side. The atomic resolution of these methods allows investigations of relations between the adsorption geometries, electron structures, and transport properties of the biomolecules. Yet, the interpretation of these data is not straightforward. The shapes, magnitudes, and temperature dependencies of the detected I-V curves cannot be explained by the incoherent hopping mechanism [35, 36]. Instead, coherent tunneling, a typical mechanism for solid-state transport processes, has been suggested to explain measured data [33, 35–41]. On the other hand, efficient, coherent transport over large and flexible biomolecules is challenging our understanding of tunneling phenomena as well.

The lack of detailed experimental data at the single-molecular level and their difficult interpretation call for accurate atomistic simulations of such systems. Last four decades, there has been significant progress in the development of computational methods and techniques able to predict key parameters for incoherent transport, elucidate the related experimental data, and understand the electron transfer in native biological environments [11]. However, simulations of the coherent processes are still challenging because they typically occur on, often solvated, bio/metallic interfaces with complex atomistic and electronic structures. Moreover, the quantum nature of coherent tunneling requires the treatment of these models fully at the quantum-mechanical level, which increases the complexity of the theoretical description and the cost of the performed simulations [36, 41]. Yet, a detailed understanding of these phenomena is desired not only from the fundamental point of view but also for further development of the rapidly growing field of nanobioelectronics [42–45].

2 Theory of electron transfer

Electronic charge is transferred through various materials via different mechanisms depending on positions, densities, and fluctuations of available electronic states. While in metals and inorganic semiconductors, which are extended and rigid, the electrons move through conduction bands of densely packed empty states, the electron hopping among energetically and spatially well-separated states of redox-active species occurs in solutions in flexible biomolecules.

2.1 Incoherent hopping

When the electronic charge, i.e. either electron or electron hole, is localized in spatially well-defined region and looses its initial phase before moving to another site, we talk about an incoherent hopping mechanism. The two sites participating in the electron transfer reaction are known as an electron donor (D) and acceptor (A). This type of charge transfer mechanism is typical for electron transitions between solvated ions or organic species, charged vacancies or defects in metal oxides, and redox sites in the biomolecular systems like peptide and proteins.

2.1.1 Marcus theory of electron transfer

Theory of the incoherent, non-adiabatic electron hopping was formulated by Marcus [46, 47] and Hush [48, 49]. The initial state D^-A of the electron-transfer reaction is supposed to be surrounded by thermally-fluctuating molecular environment which eventually brings the energies of the D/A sites to the same level (Fig. 1). When these energy states are aligned (at the so-called transition state of the reaction) the electron transfers from D to A. Consequently, the system relaxes to the final state DA^-.

Within the Marcus-Hush theory, the diabatic free energy surfaces corresponding to the initial and final states, further labeled as a and b, are parabolic, as it is shown in Fig. 2. The two minima of these parabolas correspond to the equilibrium states and their vertical difference has a meaning of the reaction free energy or driving force

$$\Delta G = G_b(\xi_b) - G_a(\xi_a). \tag{1}$$

Steepness or curvature of the energy surfaces are characterized by the reorganization free

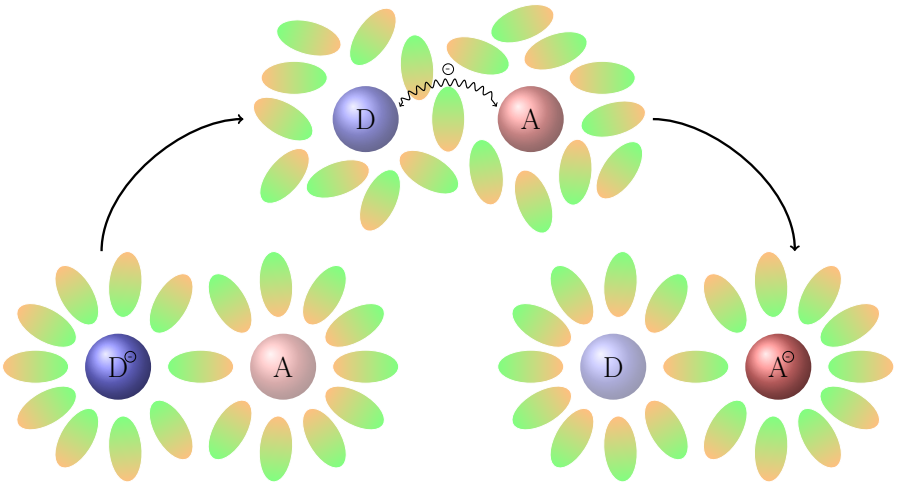

Figure 1: The schematic illustration of the electron transfer between the donor (D) and acceptor (A) species in solution. Initial equilibrium state $D^{\ominus}A$ is perturbed by thermal motion of the solvent to the transition state where the electron transfers from D to A and, afterwards, the system is relaxed to the final state $DA^{\ominus}$.

energies, which are defined as

$$\lambda_a = G_a(\xi_b) - G_a(\xi_a) \tag{2a}$$

$$\lambda_b = G_b(\xi_a) - G_b(\xi_b) \tag{2b}$$

The reorganization energy is related to relaxation processes upon the vertical charge transitions between the surfaces G_a and G_b. Within the Marcus-Hush theory, which is based on the linear response approximation, the reorganization energies for the forward and backward reaction are the same, i.e. $\lambda_a = \lambda_b = \lambda$.

The reorganization free energy can be decomposed to the inner and outer parts

$$\lambda = \lambda_i + \lambda_o. \tag{3}$$

The inner-part contribution comes from the polarization and the internal vibrational movements of the D/A sites, which change when the electronic charge is transferred [50]. This part of the reorganization free energy depends only weakly on the molecular environment [51]. On the other hand, the outer-part contribution characterizes the relaxation of the D/A surroundings (both molecular and electronic) and it grows with the increasing distance R_{DA} between the donor and the acceptor

$$\lambda_o = \frac{1}{4\pi}\left(\frac{1}{\epsilon_o} - \frac{1}{\epsilon_s}\right)\left(\frac{1}{2r_D} + \frac{1}{2r_A} - \frac{1}{R_{DA}}\right)(\Delta q)^2. \tag{4}$$

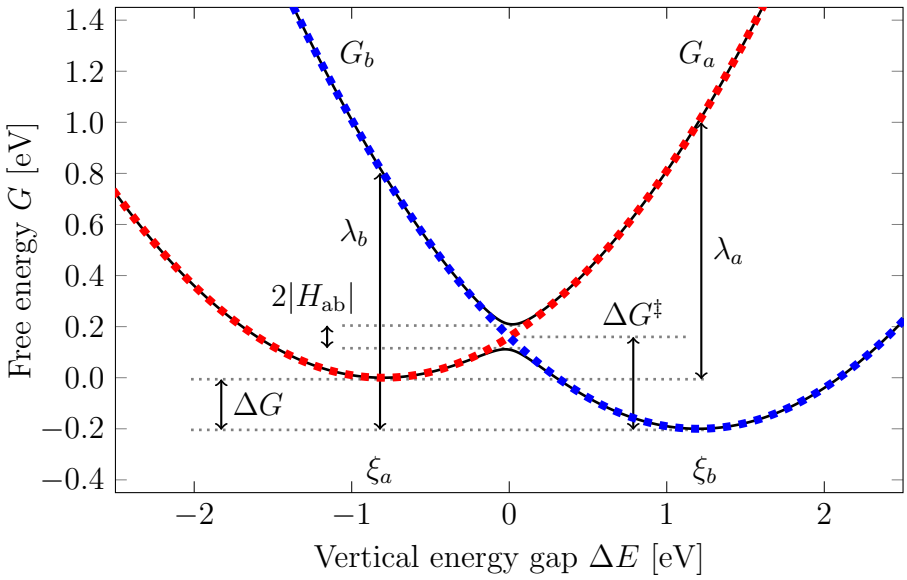

Figure 2: The schematic illustration of the Marcus free energy diabatic surfaces G_a, G_b (dashed red and blue curves) with indicated driving force ΔG, reorganization free energy λ, free energy barrier $\Delta G^{\ddagger}$, and crossing-region splitting caused by electronic coupling H_{ab}. The adiabatic surfaces G_0, G_1 of the system ground state and the first excited state, respectively, are shown by underlying solid black curves. The vertical energy gap ΔE plays the role of the reaction coordinate ξ. The parameters used to draw the scheme are ΔG = -0.2 eV, $\lambda_a = \lambda_b$ = 1.0 eV, and $|H_{ab}|$ = 0.05 eV.

Here, the r_D and r_A are radii of approximately-spherical D/A sites, and Δq is the transferred charge. The environmental prefactor expressed as the difference of reciprocal values of the optical and static dielectric constants, ϵ_o and ϵ_s, respectively, is known as the Pekar factor.

Thanks to the parabolic shape of the energy surfaces, the free energy barrier at the crossing, transition-state region can be expressed by a simple formula [52]

$$\Delta G^{\ddagger} = \frac{(\Delta G + \lambda)^2}{4\lambda} \tag{5}$$

Assuming that the transition rate can be well described by the first-order time-dependent perturbation theory, the rate constant of the given electron-transfer reaction is expressed as

$$k_{\mathrm{ET}} = \frac{2\pi}{\hbar} |H_{ab}|^2 \frac{1}{\sqrt{4\pi\lambda k_B T}} \exp\left[-\frac{\Delta G^{\ddagger}}{k_B T}\right] \tag{6}$$

The rate constant grows with the increasing reaction free energy until it reaches its maximum for the activation-less process where $\Delta G = -\lambda$. Further increase of the driving force then leads to the decrease of the rate constant. This effect is known as the Marcus

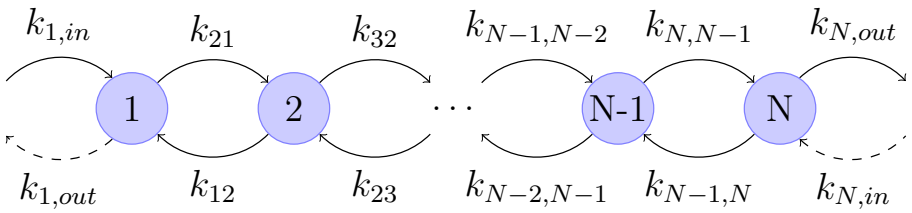

Figure 3: Linear-chain model of tightly-bound redox sites where the electron transfer proceeds only between the adjacent sites.

inverted region and it served for experimental validation of this ET theory [53].

Marcus–Hush theory was then successfully applied to describe electron transfer in redox molecular complexes [54–57], wide range of biomolecules [1, 5, 11, 16, 17, 51, 58–68], long-range redox chains [13, 21, 69–72], microbial films [73, 74], inorganic and some organic semiconductors [75–84], and also on electrochemical interfaces [85–88]. However, systems where this theory is not applicable are well known too. Typical violations of the Marcus assumptions are non-Gaussian energy-gap fluctuations caused by structural changes occurring during the charge-transfer processes [11, 89–93], nonergodic behavior due to the different time scales of electron transfer and molecular movements [64, 94–101].

2.1.2 Electronic current

The system of interest where the electronic charge is moving by the incoherent hopping mechanism can be described by the chain redox-site models [102] like in Fig. 3, where the allowed transitions with the corresponding rate constants are indicated. In the simplest case, the electron passes through the system in a linear fashion and only the transitions between the nearest neighbours are considered, however, more complex models can be designed to capture the ET pathways in particular systems [36, 72, 103].

Considering the linear-chain model shown in Fig. 3, the change of the electron population $P_i \in [0, 1]$ on the redox site i is given by difference between electron injection and ejection to/from that site

$$\frac{dP_i}{dt} = \left[k_{i,i-1}P_{i-1} + k_{i,i+1}P_{i+1}\right](1 - P_i) - \left[k_{i,i-1}(1 - P_{i-1}) + k_{i+1,i}(1 - P_{i+1})\right]P_i \qquad (7)$$

at specific time t. Under the steady-state conditions, when the site populations do not

change any more, the kinetics of the system is described by the following set of equations

$$\begin{aligned} k_{1,in}(1-P_1) + k_{12}P_2(1-P_1) &= k_{21}P_1(1-P_2) && \text{(8a)} \\ k_{i,i-1}P_{i-1}(1-P_i) + k_{i,i+1}P_{i+1}(1-P_i) &= k_{i-1,i}P_i(1-P_{i-1}) + k_{i+1,i}P_i(1-P_{i+1}) && \text{(8b)} \\ k_{N,N-1}P_{N-1}(1-P_N) &= k_{N-1,N}P_N(1-P_{N-1}) + k_{N,out}P_N && \text{(8c)} \end{aligned}$$

where the first and third equation describes the electron injection/ejection to/from the first/last site, respectively. By solving these equations, the equilibrium site populations are obtained by recursive formulas

$$P_1 = \frac{k_{12}P_2 + k_{1,in}}{(k_{12} - k_{21})P_2 + k_{1,in} + k_{21}} \tag{9a}$$

$$P_i = \frac{k_{i,i-1}P_{i-1} + k_{i,i+1}P_{i+1}}{(k_{i,i-1} - k_{i-1,i})P_{i-1} + (k_{i,i+1} - k_{i+1,i})P_{i+1} + k_{i-1,i} + k_{i+1,i}} \tag{9b}$$

$$P_N = \frac{k_{N,N-1}P_{N-1}}{(k_{N,N-1} - k_{N-1,N})P_{N-1} + k_{N,out} + k_{N-1,N}} \tag{9c}$$

The electronic flux is then given by the populations of the frontier sites

$$J = k_{1L}(1 - P_1) = k_{RN}P_N. \tag{10}$$

2.1.3 Metal/molecule interfaces

While in original Marcus theory charge transfer between two redox states is treated, at heterogeneous interfaces between metal electrodes and molecules interaction of the redox state with continuum of metallic states need to be considered [104–108]. This problem was investigated by Chidsey [86], who modified the Marcus rate-constant formula for the oxidation (k_{Mi}) and reduction (k_{iM}) of molecular species on metal surfaces

$$\begin{aligned} k_{Mi} &= \tfrac{\Gamma}{\hbar}\sqrt{\tfrac{k_BT}{4\pi\lambda_i}}\int_{-\infty}^{\infty}\exp\left[-\left(x - \tfrac{\lambda_i + e(\epsilon_i - \mu_M)}{k_BT}\right)^2 \tfrac{k_BT}{4\lambda_i}\right] / \left[1 + \exp(x)\right] dx && \text{(11a)} \\ k_{iM} &= \tfrac{\Gamma}{\hbar}\sqrt{\tfrac{k_BT}{4\pi\lambda_i}}\int_{-\infty}^{\infty}\exp\left[-\left(x - \tfrac{\lambda_i + e(\mu_M - \epsilon_i)}{k_BT}\right)^2 \tfrac{k_BT}{4\lambda_i}\right] / \left[1 + \exp(x)\right] dx && \text{(11b)} \end{aligned}$$

where

$$\Gamma = 2\pi \left\langle |H_{iM}|^2 \rho \right\rangle \tag{12}$$

is the average interfacial coupling of the site i with the electrode M, assuming wide band approximation. Fermi potential μ_M of the electrode is a material property, which is, under

open-circuit conditions, determined by the surface structure.

Besides the direct electronic interaction of the redox species with the electrode states, the electrochemical interfaces are affected by the applied bias potential, which effectively shifts the Fermi potential of the electrode. The electrode charging, and the corresponding electric field, are on the solvent side of the interface compensated by the electric double layer form by mobile ionic species [109–111]. Finally, the resulting local electric fields and increased ionic concentration influence the molecular electronic states and sometimes even structural conformations [112–114]. Due to these complex effects, theoretical investigations of charge transfer at electrochemical interfaces are not straightforward and applications of state-of-the-art computational approaches, like band-alignment corrections [115–124], non-equilibrium molecular dynamics [125–128], and special bias-potential-control techniques [129–135], are often required.

2.2 Coherent tunneling

Coherent tunneling is a type of quantum transport where the charge passes through the potential region exceeding its available energy while the phase of its wavefunction does not change during such process. The charge particle thus does not significantly interact with its environment or other (quasi)particles. Therefore, the coherent tunneling typically proceed balistically or in weak-interaction regime where inelastic scattering is negligible [136–138].

2.2.1 Landauer-Büttiker formalism

The Landauer-Büttiker formalism [139,140], known also as the scattering method, relates the transport properties to the electron transmission through the considered material. In this formalism, the tunneling current can be obtained by integration of transmission function $T(E)$ within the so-called Fermi window

$$I(V) = \frac{e}{\pi\hbar} \int T(E) \left[f_L(E,V) - f_R(E,V) \right] dE \tag{13}$$

The Fermi window is given by the difference of Fermi–Dirac distributions f_M, characterized by Fermi potentials μ_M, of the two contacts ($M = L,\ R$)

$$f(E) = \frac{1}{\exp\left(\frac{E-\mu}{k_B T}\right) + 1} \tag{14}$$

The transmission function describes the probability that an electron tunnels from the

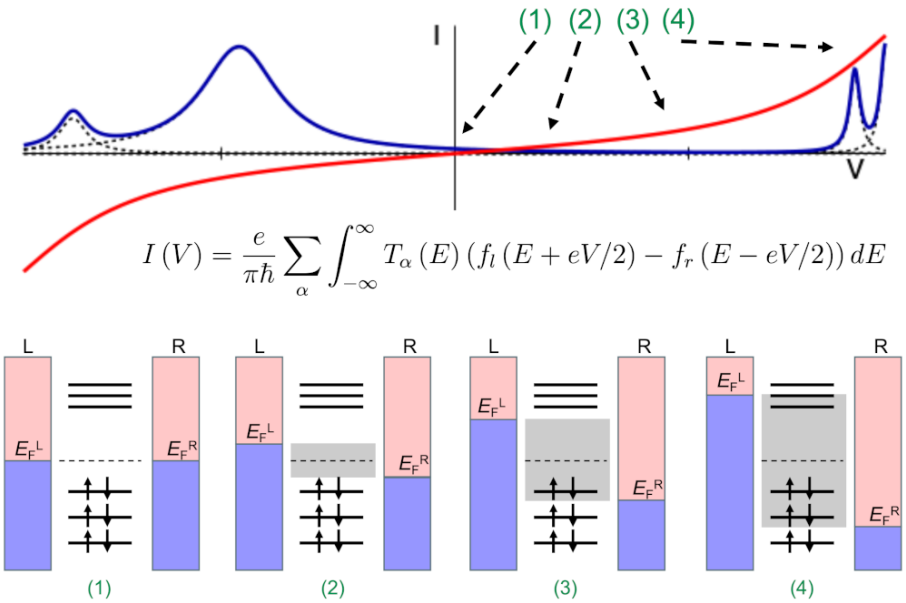

Figure 4: Schematic illustration of Landauer integration of transmission function for molecular system where the equilibrium Fermi level of the contacts is located in the HOMO–LUMO gap. Occupied and empty states of the left (L) and right (R) metal contact are shown in blue and red colors, respectively.

left contact region L via the scattering region S to the right contact R at energy level E. In the Breit-Wigner approximation, where the electronic states within the scattering region are regarded as independent and non-interacting, the transmission function is written as a sum of single Lorentzian peaks [141, 142]

$$T(E) = \sum_{j \in S} \frac{\Gamma_j^{(L)}(E)\Gamma_j^{(R)}(E)}{[E - \epsilon_j]^2 + [\Gamma_j^{(L)}(E) + \Gamma_j^{(R)}(E)]^2/4} \tag{15}$$

The Γ functions, known as spectral densities, are responsible for the molecular state broadening due to their interactions with the metal contacts. The functions are related to the electronic coupling elements between the molecular state j from the scattering region S and metallic states m, H_{mj}, weighted by their densities ρ_M

$$\Gamma_j^{(M)}(E) = 2\pi \left[|H_{mj}|^2 \rho_M(\epsilon_{M,m})\right]_{\epsilon_{M,m}=E} \tag{16}$$

For the interpretation of experimentally measured tunneling current–voltage (I-V) curves, this formalism is usually further simplified [35]. However, the Landauer-Büttiker formalism can be used to predict the tunneling current magnitudes directly from the *ab initio* data [143], typically obtained by the tight-binding (TB) potentials or density-

functional theory (DFT). In these cases, full all-to-all transmission matrix is usually considered as a generalization of the simplified Breit-Wigner transmission function. Further, the formalism allows description of devices with more than two contacts to the scattering region [139, 144], which makes it popular for theoretical description of various electronics components and molecular junctions [145–149]. Recently, this methodology and its modifications was also applied to investigation of extended biomolecular junctions [36, 41, 150].

2.2.2 Green's function description

Alternatively, the transport problem can be mathematically formulated using Green functions, which are more suitable for description of open and non-equilibrium systems. The retarded ($\hat{G}$) and advanced ($\hat{G}^\dagger$) Green functions are propagators describing system evolution, i.e. solution of the time-dependent Schrödinger's equation

$$i\hbar\frac{\partial\left|\psi(t)\right\rangle}{\partial t} = \hat{H}\left|\psi(t)\right\rangle \tag{17}$$

in time

$$\left|\psi(t)\right\rangle = i\hbar\hat{G}(t-t_0)\left|\psi(t_0)\right\rangle, \qquad t > t_0 \tag{18}$$

or back in time

$$\left|\psi(t)\right\rangle = -i\hbar\hat{G}^\dagger(t-t_0)\left|\psi(t_0)\right\rangle, \qquad t < t_0 \tag{19}$$

In energy representation, which is connected with the time representation by the Fourier transform, the retarded Green function has the traditional form

$$\hat{G}(E) = \left[(E+i\eta)\hat{I} - \hat{H}\right]^{-1} \tag{20}$$

where η is small real number offsetting the energies to complex plane to avoid divergencies at Hamiltonian poles ϵ_j. In the spectral representation, convenient for numerical calculations, the retarded Green function has the form

$$\hat{G}(E) = \sum_n \frac{\left|\psi_n\right\rangle\left\langle\psi_n\right|}{E-\epsilon_n+i\eta} \tag{21}$$

where ψ_n and ϵ_n are eigenfunctions and eigenvalues of the Hamiltonian $\hat{H}$, respectively.

The scattering can be then captured in perturbation fashion by Lippmann-Schwinger equation [151]

$$\hat{G}(E) = \hat{G}_0(E) + \hat{G}(E)\hat{V}\hat{G}_0(E) \tag{22}$$

where $\hat{G}_0$ describes the incoming particle, $\hat{G}$ the scattered particle, and the scattering potential is described by the operator $\hat{V}$. Finally, using the Fisher–Lee relation between the Green function and the scattering matrix [152], the transmission function can be expressed as [153, 154]

$$T(E) = \mathrm{Tr}\left[\hat{\Gamma}^{(L)}(E)\hat{G}^{(S)\dagger}(E)\hat{\Gamma}^{(R)}(E)\hat{G}^{(S)}(E)\right] \tag{23}$$

where $\hat{G}^{(S)}$ is the Green function operator of the scattering region where the interaction with the contacts is involved via the self-energy operators $\hat{\Sigma}^{(M)}$. The operators $\Gamma^{(M)}$ are related to self-energy as $\mathrm{Im}[\hat{\Sigma}] = -\frac{1}{2}\hat{\Gamma}$.

The Green function description of the open system can be generalized to non-equilibrium cases by the so-called Keldysh formalism [155]. This method, known as non-equilibrium Green function (NEGF) [156–163], has been implemented in many TB and DFT software packages [164–167], and became popular for investigation of transport properties of semiconductor nanoelectronic components [136,137,168–170] and molecular junctions [102, 138, 171].

3 Computational approaches

3.1 Current-voltage curve modeling

Measured current-voltage (I-V) curves from single-molecular experiments like STM are usually first analyzed by using analytical models capturing the physical properties of the probed sample [29, 32, 33, 35, 39, 41, 150, 172–198]. For example, one can design multi-site hopping models for modeling electron fluxes through redox protein chains [68, 102, 103] or apply tunneling models [199, 200] to analyze current curves in solid-state junctions. Usually, agreement of several different models with the experimental data is explored to determine the electron transfer mechanism and estimate values of the key parameters (see Fig. 5 for details).

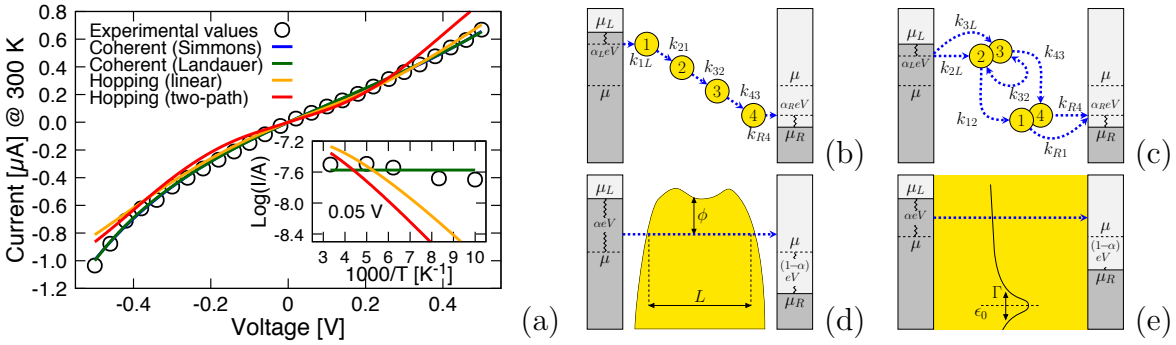

Figure 5: (a) Fitting of experimental current–voltage (I-V) and current–temperature (I-T) curves (inset) for the tetra-heme protein STC [35]. Models of incoherent hopping (b) along a linear chain and (c) along a branched chain of redox sites are compared to coherent tunneling (d) Simmons model and (e) single-channel Landauer model.

3.1.1 Incoherent hopping models

Incoherent hopping models, based on the kinetic master equations described in Sec. 2.1.2, are popular for modeling of I-V curves measured on redox systems where applicability of the Marcus–Hush theory of electron transfer [46,48] can be assumed. The hopping models can be adapted to capture geometry and expected ET pathways in particular systems. While simple linear chains can be applied to compute electronic fluxes, for example, in multi-heme cytochromes [13, 68, 71, 201], branched chains are typically more suitable for investigation of electron transfer in redox cascades involving more proteins [65, 72, 103]. Moreover, the model can describe also electron hopping events in molecular crystals [76, 77, 81, 82, 202–205] and in inorganic semiconductors [75, 78–80, 206], although solution of

the kinetic master equations for such ET networks requires different methodology then the simpler chain pathways.

For the small linear chains, analytical solution of the equations (9) can found directly or by using various symbolic solvers [68]. However, this becomes impractical for the cases where long chains involving many redox sites are investigated, and impossible for the more complex, typically branched, ET pathways. In such cases, the solution (i.e. the equilibrium populations of the individual sites and the steady-state current) is usually obtained by iterative techniques, where the initial populations are guessed (often set to zero) and then improved by iterative cycles [35, 36, 102]. Finally, for the complex and extended ET networks, where the iterative methods would converge too slowly or suffer from oscillations, kinetic Monte Carlo approaches are applied [202, 203, 207].

However, for analyzing the experimentally measured current data, number of free parameters must be reduced to ambiguities related to over-fitting. The input rate constants are computed from the Marcus formula (6), which requires knowledge of the driving force (ΔG), reorganization free energy λ, and electronic coupling H_{ab}. Typically, available experimental redox-potential values are employed to obtain ΔG, λ and H_{ab} are estimated from Eqs. 4 and 72, and parameters of interest (e.g., missing redox potential or rate constant between specific redox pair) are fitted. Recently, we used such incoherent hopping modeling of I-V curves measured on solid-state protein junctions based on multi-heme cytochromes [35, 36], where we simultaneously fitted the current dependencies on applied bias potential and temperature (shown in Fig. 5), to prove that the hopping cannot explain high current magnitudes and weak thermal effects in such devices.

3.1.2 Coherent models

Simmons model The model of Simmons [200] describes electron tunnelling through a potential barrier of arbitrary shape representing a thin insulating film between two conductive electrodes. Assuming the average barrier height ϕ above the Fermi level μ_L of the negatively-charged left electrode and the potential drop occurring at the right electrode, the current can be described as

$$I(V) = \frac{e^2}{2\pi h}\left[\left(\phi - \alpha V\right) e^{-K\sqrt{\phi-\alpha V}} - \left(\phi + (1-\alpha)\, V\right) e^{-K\sqrt{\phi+(1-\alpha)V}}\right] \tag{24}$$

where

$$K = 4\pi L \left(2me\right)^{1/2} / h \tag{25}$$

is determined by tunnelling length L. The model involves also the so-called symmetry factor α allowing description of arbitrary distribution of the potential drop on the electrodes [208].

Landauer model In the Landauer formalism [142, 191], the transmission function is approximated by a Lorentzian peak

$$T(E) = \frac{\Gamma_L \Gamma_R}{[E - \epsilon_0]^2 + \Gamma^2}, \qquad \Gamma = (\Gamma_L + \Gamma_R)/2 \tag{26}$$

representing the conduction channel, that is a molecular energy level ϵ_0 mediating the tunnelling current. Γ_L and Γ_R are spectral densities (interfacial protein/electrode couplings exhibited by interfacial state broadening) determining the shape of the transmission function.

As in the Simmons model, a symmetry factor α is introduced to control the potential drop on the electrodes via the positions of their Fermi levels

$$\mu_L = \alpha eV/2, \qquad \mu_R = -(1-\alpha)eV/2 \tag{27}$$

The integral with transmission function (26) is solved in the zero-temperature limit, where the Fermi–Dirac distribution converges to a Heaviside step function $f(E) \to \vartheta(E - \mu)$ and $df/d\mu \to \delta(E - \mu)$. In this limit the electric conductance can be written in analytic form,

$$\begin{aligned} g(V) = \frac{dI}{dV} = \frac{e}{\pi\hbar}\left[\int T(E)\frac{df}{d\mu_L}\frac{d\mu_L}{dV}dE - \int T(E)\frac{df}{d\mu_R}\frac{d\mu_R}{dV}dE\right] = \\ = G_0\Gamma_L\Gamma_R\left[\frac{\alpha}{(\alpha eV - \epsilon_0)^2 + \Gamma^2} - \frac{\alpha - 1}{((\alpha-1)eV - \epsilon_0)^2 + \Gamma^2}\right], \end{aligned} \tag{28}$$

where $G_0 = e^2/\pi\hbar$ is known as the quantum conductance (i.e., the maximal conductance of the single electronic level). The tunneling current is then obtained by integration of (28), giving

$$I(V) = \frac{2G_0}{e}\frac{\Gamma_L\Gamma_R}{\Gamma_L + \Gamma_R}\left[\arctan\frac{\alpha eV - \epsilon_0}{(\Gamma_L + \Gamma_R)/2} - \arctan\frac{(\alpha-1)eV - \epsilon_0}{(\Gamma_L + \Gamma_R)/2}\right], \tag{29}$$

For the fitting of the experimental I-V curves to (29), the same coupling values to the left and right electrode ($\Gamma_L = \Gamma_R \equiv \Gamma$) are typically assumed. Hence, there are three fitting parameters: ϵ_0, Γ, α in this model.

3.2 Molecular dynamics (MD) techniques

Due to the flexible nature of the molecular soft matter, including biomolecules, sampling of configuration space by molecular dynamics is often employed. In the classical mechanics, the state of a particle is determined by its position $\boldsymbol{r}$ and momentum $\boldsymbol{p}$. Integrating the equations of motion, time evolution of these two quantities can be written as

$$\boldsymbol{r}(t) = \boldsymbol{r}(t_0) + \int_{t_0}^{t} \frac{\boldsymbol{p}(t')}{m} dt' \tag{30a}$$

$$\boldsymbol{p}(t) = \boldsymbol{p}(t_0) + m \int_{t_0}^{t} \boldsymbol{a}(t') dt' \tag{30b}$$

where $\boldsymbol{a}(t) = \boldsymbol{F}(t)/m$ is atomic acceleration caused by the force $\boldsymbol{F}$. The time-evolution integrals can be solved by various numerical methods differing by complexity and accuracy, for example, by the so-called "velocity Verlet" algorithm, which is popular in atomistic MD simulations.

Original Verlet algorithm is based on Taylor expansion of position in time [209]

$$\boldsymbol{r}(t + \Delta t) = 2\boldsymbol{r}(t) - \boldsymbol{r}(t - \Delta t) + \boldsymbol{a}(t)(\Delta t)^2 \tag{31}$$

without explicit formula for velocities. To avoid their calculations by finite differentiation, the algorithm was later updated [210]

$$\boldsymbol{r}(t + \Delta t) = \boldsymbol{r}(t) + \boldsymbol{v}\Delta t + \frac{1}{2}\boldsymbol{a}(t)(\Delta t)^2 \tag{32a}$$

$$\boldsymbol{v}(t + \Delta t) = \boldsymbol{v}(t) + \frac{1}{2}[\boldsymbol{a}(t + \Delta t) + \boldsymbol{a}(t)]\Delta t \tag{32b}$$

which is known as the velocity Verlet method.

3.2.1 Ab initio MD simulations

Naturally, the above-mentioned integration of the classical equations of motions is performed on systems described by classical potentials (the so-called molecular mechanical description or classical force-field description). This approach is typical for structural studies of molecular systems like solvated organic molecules, biomolecules, solid/liquid interfaces, bio/metallic interfaces, etc. However, when chemical changes such as bond breaking/making or electron transfer occur, the quantum description needs to be employed. Such computations are usually referred as *ab initio* or first-principles simulations [211]

In the quantum mechanics, the time-dependent Schrödinger equations plays the role of the equation of motion

$$i\hbar\frac{\partial}{\partial t}\left|\psi(\boldsymbol{r},\boldsymbol{R},t)\right\rangle = \hat{H}\left|\psi(\boldsymbol{r},\boldsymbol{R},t)\right\rangle \tag{33}$$

where $\boldsymbol{r}$ and $\boldsymbol{R}$ denotes all electronic and nuclear coordinates, respectively. As the electronic motions are much faster than the nuclear movements, these two coordinate types can be separated

$$\psi(\boldsymbol{r},\boldsymbol{R},t) = \phi(\boldsymbol{r},t)\chi(\boldsymbol{R},t) \tag{34}$$

which leads to coupled time-depended self-consistent-field (TDSCF) equations

$$i\hbar\frac{\partial\chi}{\partial t} = -\sum_\alpha \tfrac{\hbar^2}{2M_\alpha}\nabla_\alpha^2\chi + \left\langle\phi\right| - \sum_i \tfrac{\hbar^2}{2m}\nabla_i^2 + V_{ne}\left|\phi\right\rangle\chi \tag{35a}$$

$$i\hbar\frac{\partial\phi}{\partial t} = -\sum_i \tfrac{\hbar^2}{2m}\nabla_i^2\phi + \left\langle\chi\right| - \sum_\alpha \tfrac{\hbar^2}{2M_\alpha}\nabla_\alpha^2 + V_{ne}\left|\chi\right\rangle\phi \tag{35b}$$

where V_{ne} stands for Coulomb potential describing electrostatic interaction between nuclei and electrons (i.e., external potential in density functional theory).

Ehrenfest molecular dynamics Since the atomic nuclei are by three orders of magnitude heavier than electrons, their motion can be described classically while the electronic wavefunction adiabatically follows the changing nuclear potential.

$$i\hbar\frac{\partial\phi}{\partial t} = -\sum_i \frac{\hbar^2}{2m}\nabla_i^2\phi + V_{ne}\phi \tag{36}$$

The above equation of motion for electronic degrees of freedom is solved self consistently while the nuclear propagation is obtained by integration of classical Newton's equations. This type of molecular dynamics is known and Ehrenfest MD or mean-field MD [212–214].

Born-Oppenheimer dynamics When the energy gap between the electronic ground state and excited states is large compared to thermal energy k_BT, the motion of the nuclei can be restricted to the potential energy surface of the ground state.

$$M_\alpha\frac{d^2\boldsymbol{R}_\alpha}{dt^2} = -\nabla_\alpha \min_{\{\phi_i\}}\left[\left\langle\phi_0\right| - \sum_i \frac{\hbar^2}{2m}\nabla_i^2 + V_{ne}\left|\phi_0\right\rangle\right] \tag{37}$$

where $\left|\phi_0\right\rangle$ is the ground state adiabatic wavefunction of the time-independent electronic Hamiltonian. This approach is known as Born-Oppenheimer molecular dynamics

(BOMD) [211] and it is popular for the first-principles simulations because it allows to propagate the nuclear motion with much larger time steps than in the Ehrenfest MD. However, solving the stationary Schrödinger equation at each MD step is still very computationally demanding.

Car-Parrinello dynamics To avoid expensive self-consistent finding of the ground state in BOMD, Car and Parrinello formulated the extended Lagrangian [215]

$$\mathcal{L} = \sum_{\alpha} \frac{1}{2} M_\alpha \boldsymbol{R}_\alpha^2 + \sum_i \mu_i \langle \dot{\phi}_i | \dot{\phi}_i \rangle - \langle \phi_0 | - \sum_i \frac{\hbar^2}{2m} + V_{ne} | \phi_0 \rangle + \sum_{i,j} \Lambda_{ij} \left[\langle \phi_i | \phi_i \rangle - \delta_{ij} \right] \quad (38)$$

leading to Car-Parrinello equations of motions

$$M_\alpha \frac{d^2 \boldsymbol{R}_\alpha}{dt^2} = -\nabla_\alpha \langle \phi_0 | - \sum_i \frac{\hbar^2}{2m} + V_{ne} | \phi_0 \rangle \quad (39a)$$

$$\mu_i \frac{d^2 \phi_i}{dt^2} = \sum_i \left[\frac{\hbar^2}{2m} \nabla_i^2 - V_{ne} \right] \phi_i + \sum_j \Lambda_{ij} \phi_j \quad (39b)$$

where each state ϕ_i is propagated with fictitious mass μ_i, while its normalization is imposed by Lagrange multipliers Λ_{ij}. The ground state ϕ_0, constructed as a Slater determinant of the one-electron states ϕ_i, is thus propagated without need of the self-consistent solution. This method is popular in the plane-wave density-functional-theory codes, where the individual terms are easily evaluated [211].

3.2.2 Thermodynamic properties

A connection between the atomistic simulations and the macroscopic properties of the molecular systems is provided by the formalism of statistical mechanics [216]. The so-called ergodic hypothesis represents the key relation of the time averaging of variable A during the MD simulation and the statistical averages $\langle A \rangle$

$$\bar{A} \equiv \lim_{T \to \infty} \frac{1}{T} \int_0^T A(t) dt = \frac{\iint A(\boldsymbol{r}, \boldsymbol{p}) \exp\left(-\frac{H(\boldsymbol{r},\boldsymbol{p})}{k_B T}\right) d\boldsymbol{r} d\boldsymbol{p}}{\iint \exp\left(-\frac{H(\boldsymbol{r},\boldsymbol{p})}{k_B T}\right) d\boldsymbol{r} d\boldsymbol{p}} \equiv \langle A \rangle \quad (40)$$

In practice, the exact time average $\bar{A}$ is approximated by mean value over the available MD samples

$$\bar{A} \approx \frac{1}{N} \sum_{i=1}^{N} A_i \quad (41)$$

and the variations are calculated by the block-average method

$$\sigma^2 = \frac{1}{N_b - 1} \sum_{\beta=1}^{N_b} \left(A_\beta^2 - \langle A \rangle_b^2 \right) \tag{42}$$

where N_b is number of used blocks, A_β is the block average, and $\langle A \rangle_b$ is the average over all the blocks [217, 218].

Besides the total energy E, the system temperature T, and pressure p are typically tracked or controlled during the MD simulations. The temperature is obtained via the Boltzmann equipartition theorem

$$\frac{3}{2} N k_B T = \left\langle \frac{1}{2} \sum_{i=1}^{N} m_i v_i^2 \right\rangle \tag{43}$$

where N is total number of particles in the system and v_i are their velocities. On the other hand, the virial theorem is often employed to compute the system pressure

$$pV = N k_B T - \frac{1}{3} \left\langle \sum_{i=1}^{N} \boldsymbol{r}_i \boldsymbol{F}_i \right\rangle \tag{44}$$

While the direct propagation of the equations of motions conserves the total energy E and leads to sampling of the microcanonical (NVE) ensemble, constraining the temperature or pressure is usual to sample canonical (NVT) and isothermal-isobaric (NpT) ensembles, respectively. For open systems, grand canonical ensemble (μVT) with fixed chemical potential μ is often applied.

3.2.3 Free energy calculations

The statistical ensembles (NVE, NVT, NpT, μVT) are, via their partition functions (Ω, Q, Λ, Ξ), directly related to thermodynamic potentials (S, A, G, pV), which are important for practical applications

Ensemble	Potential	Relation
microcanonical	entropy	$S = k_B \ln \Omega(N, V, E)$
canonical	Helmholtz free energy	$A = -k_B T \ln Q(N, V, T)$
isothermal-isobaric	Gibbs free energy	$G = -k_B T \ln \Lambda(N, p, T)$
grand canonical	mechanical work	$pV = k_B T \ln \Xi(\mu, V, T)$

However, these thermodynamic potentials cannot be obtained from MD directly because proper evaluation of the related partition functions would require effectively infinitely-

long simulations. Therefore, various approaches have been developed to compute the free energies by methods of enhanced sampling [216, 219, 220].

Free energy perturbation theory From the practical point of view, only the free energy differences between states of interest are relevant for applications. For example, the free energy difference between the reactants and products of chemical reactions determines exothermicity or spontaneity of such processes. When these two states are energetically close, the perturbation theory can be employed to express the desired free energy difference [216, 221], leading to the formula

$$\Delta A_{01} = -k_B T \ln \left\langle e^{-\Delta U/k_B T} \right\rangle_0, \qquad \Delta U = U_1 - U_0 \tag{45}$$

where U_0, U_1 are potential energies of the reactant and products, respectively, while $\langle \dots \rangle_0$ denotes mean value on reactant potential energy surface. When the potential-energy distributions are Gaussian, the formula can be simplified to [220]

$$\Delta A_{01} = \langle \Delta U \rangle_0 - \frac{1}{2k_B T} \left(\left\langle \Delta U^2 \right\rangle_0 - \langle \Delta U \rangle_0^2 \right) \tag{46}$$

which is often used in practical applications.

When the energy differences between the two states are large, in a sense that the Boltzmann factor $e^{-\Delta U/k_B T}$ becomes negligibly small, the perturbation formula cannot be directly used. However, the path from the reactants to the products can be interpolated at Hamiltonian level

$$\hat{H}(\lambda) = (1 - \lambda)\hat{H}_0 + \lambda \hat{H}_1 \tag{47}$$

using the mapping parameter $\lambda \in [0, 1]$ and divided into N segments. The total free energy difference ΔA_{01} is then computed as a sum of free energy differences between these segments [216]

$$\Delta A_{01} = -k_B T \sum_{i=1}^{N-1} \ln \left\langle e^{-\Delta U_{i,i+1}/k_B T} \right\rangle_i \tag{48}$$

Thermodynamic integration The Hamiltonian interpolation (47) between the two states of interest is typical for the so-called thermodynamic integration approaches. In general, the free energy difference can be obtained by integration of potential mean force along the path between the reactants and products [222]

$$\Delta A_{01} = \int_0^1 \frac{\partial A}{\partial \lambda} d\lambda = \int_0^1 \left\langle \frac{\partial U}{\partial \lambda} \right\rangle_\lambda d\lambda \tag{49}$$

where $\langle \dots \rangle_\lambda$ denotes mean value at fixed λ. The free energy difference does not depend on the chosen pathway between the two states. However, when the linear interpolation (47) is used, the integration formula simplifies to [216, 220]

$$\Delta A_{01} = \int_0^1 \langle U_1 - U_0 \rangle_\lambda \, d\lambda \tag{50}$$

In practice, the pathways is divided into N segments and the mean values $\langle \Delta U \rangle_{\lambda_i}$ are evaluated for the selected $\lambda_i \in [0, 1]$ values. These are then integrated by standard numerical algorithms.

Blue moon ensemble In molecular systems, the studied processes can be often described by a reaction coordinate, i.e. a collective variable $f(\boldsymbol{r}_1, \dots, \boldsymbol{r}_N)$ dependent on positions $\boldsymbol{r}_i$ of N particles involved in the system, which represent a natural pathway between the reactant and the products. The free energy difference along the reaction coordinate can be evaluated in the thermodynamic integration fashion by imposing the holonomic constraints

$$\sigma(\boldsymbol{r}_1, \dots, \boldsymbol{r}_N) = f(\boldsymbol{r}_1, \dots, \boldsymbol{r}_N) - s \tag{51}$$

where s is the pre-set value of the collective variable f. However, this affects the dynamics of the system, and the formula (49) needs to be corrected in the following way [223–226]

$$\Delta A_{01} = \int_0^1 \frac{\left\langle z^{-1/2}(\boldsymbol{r})[\lambda + k_B T G] \right\rangle_s}{\left\langle z^{-1/2}(\boldsymbol{r}) \right\rangle_s} ds \tag{52}$$

where $z(\boldsymbol{r})$ is a metric, known as the Fixman potential, which has a value

$$z(\boldsymbol{r}) = \sum_i \frac{1}{m_i} \left(\frac{\partial \sigma}{\partial \boldsymbol{r}_i} \right)^2 \tag{53}$$

while the G parameters can be expressed as

$$G = \frac{1}{z^2(\boldsymbol{r})} \sum_{i,j} \frac{1}{m_i m_j} \frac{\partial f}{\partial \boldsymbol{r}_i} \cdot \frac{\partial^2 f}{\partial \boldsymbol{r}_i \partial \boldsymbol{r}_j} \cdot \frac{\partial f}{\partial \boldsymbol{r}_j} \tag{54}$$

The Lagrange multiplier λ have a general form [216]

$$\lambda = -\frac{1}{z(\boldsymbol{r})} \left[\sum_i \frac{\boldsymbol{F}_i}{m_i} \cdot \frac{\partial \sigma}{\partial \boldsymbol{r}_i} + \sum_{i,j} \boldsymbol{v}_i \cdot \frac{\partial^2 \sigma}{\partial \boldsymbol{r}_i \boldsymbol{r}_j} \cdot \boldsymbol{v}_j \right] \tag{55}$$

However, in practice, the simplified expressions for a specific constrains such as interatomic distances are used [227].

Umbrella sampling In the umbrella sampling method [228, 229], instead of constraining MD at specific segments of the reaction coordinate like in the blue moon ensemble approach, the restraining bias potentials are are applied, which usually have the following harmonic form

$$W(f,s) = \frac{1}{2}k[f(\boldsymbol{r}_1,\ldots,\boldsymbol{r}_N) - s]^2 \tag{56}$$

The system fluctuates near the pre-set value s of the reaction coordinate f. The biased distributions $P^b(q,s)$, which are functions of generalized coordinates q, are approximated by histograms collected during the restrained MD simulations. The bias distributions from different segments of the reaction coordinates are then reweighted to obtain the unbiased distributions

$$P_i(q) = e^{-(A_i - A_0)/k_BT} e^{W(q,s_i)/k_BT} P^b(q,s_i) \tag{57}$$

using the free energies A_i associated with the bias potentials $W_i \equiv W(f,s_i)$. These are related to the total unbiased distribution $P(q)$ as

$$e^{(A_i - A_0)/k_BT} = \int P(q) e^{W_i/k_BT} dq \tag{58}$$

The total distribution is constructed as a linear combination of unbiased distribution from the individual reaction-coordinate segments, $P(q) = \sum_i c_i(q) P_i(q)$. The coefficients c_i are set to minimize the statistical error, which leads to the expression

$$P(q) = \frac{\sum_i n_i P_i(q)}{\sum_k n_i e^{(A_i - A_0)/k_BT} e^{-W_i/k_BT}} \tag{59}$$

Finally, the free energy profile along the reaction coordinate is obtained as

$$A(q) = -k_BT \ln P(q) \tag{60}$$

However, as the equations (58) and (59) are coupled, they need to be solved iteratively until the self-consistent solution if found. This approach is known as the weighted histogram analysis method (WHAM) [230, 231] and it can be easily generalized to describe multidimensional free energy surfaces [232].

Metadynamics The bias potentials (56) in the umbrella sampling method need to be distributed along the reaction coordinate in a way to ensure sufficient overlaps of the bias distributions $P^b(q, s_i)$. However, as the free energy profile is not known *a priory*, additional restrained MD simulations need to be performed for the poorly sampled reaction-coordinate regions, which makes the method computationally and time demanding. To avoid these problems, Laio and Parrinello [233–235] invented the enhanced sampling technique known as metadynamics, where the bias potentials of Gaussian shapes are automatically placed on the already-sampled regions of the reaction coordinate as the MD simulations progress

$$W(q,t) = H \sum_{t_i} \exp\left[-\frac{|f(q) - f(q,t_i)|^2}{2w^2}\right] \tag{61}$$

The system is thus enforced to overcome free energy barriers and sample the higher-energy configurations. Finally, the free energy profile converges to the negative sum of all the bias potentials distributed along the reaction coordinate

$$A(q) = -\lim_{t\to\infty} W(q,t) \tag{62}$$

Later, modified versions of metadynamics were designed where the Gaussian bias potentials (61) adapt their widths w and heights H to sample the free energy profile in the most efficient way [236, 237].

3.2.4 Non-equilibrium MD simulations

The above discussed free-energy calculation method are related to canonical statistical ensemble, sampled by equilibrium MD techniques. Nevertheless, the system of interest can be perturbed by time-dependent external fields to which the system responds. For example, charge transport events can be induced by applied bias potential or electric field, respectively, which could be followed by faster or slower relaxation processes [238].

At the classical level of theory, the electromagnetic field effects can be studied by non-equilibrium MD simulations based on the equations of motions involving the time-dependent Lorentz force [126]

$$M_\alpha \frac{d^2\boldsymbol{R}_\alpha}{dt^2} = -\nabla_\alpha V(\boldsymbol{R}) + q_\alpha \boldsymbol{E}(t) + q_\alpha \boldsymbol{v}_\alpha \times \boldsymbol{B}(t) \tag{63}$$

where q_α are particle charges and $\boldsymbol{E}$, $\boldsymbol{B}$ are electric and magnetic field vectors, respectively. These are perpendicular to each other, as well as to the field-propagation direction, as it

is required by Maxwell equations. In the nanoscopic simulations, the field intensities are usually regarded to be uniform throughout the system and their magnitudes vary with angular frequency ω

$$\boldsymbol{E}(t) = E_{\max} \cos(\omega t) \boldsymbol{e}_x \tag{64a}$$

$$\boldsymbol{B}(t) = B_{\max} \cos(\omega t) \boldsymbol{e}_y \tag{64b}$$

The root-mean-square (RMS) electric field intensity is $E_{\mathrm{rms}} = E_{\max}/\sqrt{2}$. Further, electric and magnetic field intensities are related as $E_{\max}/B_{\max} = c/n$ where c is the vacuum speed of light while n stands for the refractive index of a given environment.

In the first-principles simulations, the interaction of the system with external fields need to be described at Lagrangian or Hamiltonian level. For example, the dipole interaction with the electric field can be studied by involving the potential

$$V_{\mathrm{dip}}(t) = -\boldsymbol{\mu} \cdot \boldsymbol{E}(t) \tag{65}$$

where μ is the electric dipole moment of the system. However, more complex and general field-matter interaction terms can be applied, depending on the particular problem of interest [239]. For the molecular system, density functional theory (DFT) together with Berry phase formulation and modern theory of polarization are employed to describe the external field effects [125,240]. These techniques have been used, for example, for studying electrocatalysis of chemical reactions [241–245], field effect of liquid water [128,246]. More complex system, like biomolecules and the heterogeneous interfaces, are usually studied at classical level of theory [127, 247–251].

3.3 Electronic coupling

Diabatic electronic states, which represent localized charge states in the ET studies [46,55, 252], are, in contrast to adiabatic states, not eigenfunctions of the electronic Hamiltonian of the system. Therefore, off-diagonal elements of the Hamiltonian matrix in diabatic-state representation are not zero. These elements are known as electronic coupling matrix elements H_{ab} and they quantify interactions between the diabatic states ψ_a, ψ_b:

$$H_{ab} = \langle \psi_a | \hat{H} | \psi_b \rangle \tag{66}$$

For investigation electron transfer in donor-acceptor system, a simple two-state model is often used with electronic Hamiltonian

$$\mathbb{H} = \begin{pmatrix} E_a & H_{ab} \\ H_{ab} & E_b \end{pmatrix} \tag{67}$$

Energies of the adiabatic ground state (E_0) and the first excited state (E_1) are

$$E_{0,1} = \frac{1}{2}\left(E_a + E_b \mp \sqrt{(E_a - E_b)^2 + 4|H_{ab}|^2}\right). \tag{68}$$

If the studied system is symmetric like in self-exchange ET reaction, then diabatic energies of the donor and acceptor are equal ($E_a = E_b$) and the energy gap between the adiabatic states is is simply twice the diabatic coupling matrix element

$$\Delta E_{01} = E_1 - E_0 = 2|H_{ab}|. \tag{69}$$

This is often utilized in high-level quantum-chemistry calculations of the coupling elements between homo-dimer units [253–256].

The two state model can be generalized to the case where the two diabatic states ψ_a, ψ_b are not orthogonal. [257] Then, the overlap matrix has non-zero off-diagonal elements $S_{ab} = \langle\psi_a|\psi_b\rangle$ and the adiabatic energy gap equals to

$$\Delta E_{01} = \frac{1}{1 - S_{ab}^2}\sqrt{(E_a - E_b)^2 - 4[H_{ab}S_{ab}(E_a + E_b) - H_{ab}^2 - E_a E_b S_{ab}^2]}. \tag{70}$$

The coupling element V_{ab}, also known as electron-transfer matrix element or transfer integral, is defined as the half of the adiabatic energy splitting at the crossing point of the diabatic surfaces

$$V_{ab} = \frac{1}{2}\,\Delta E_{01}|_{E_a=E_b} = \frac{1}{1 - S_{ab}^2}\sqrt{H_{ab} - S_{ab}\frac{E_a + E_b}{2}}. \tag{71}$$

Obviously, the coupling is close to the off-diagonal diabatic matrix element $V_{ab} \sim H_{ab}$ when the overlap between the two charge states is negligible ($S_{ab} \ll 1$). This expression is typically used to evaluate the coupling for the intra-molecular electron transfer reactions. [257–263]

3.3.1 Empirical approaches

Evaluation of the electronic coupling elements by quantum wavefunction methods or by density-functional-theory (DFT) approaches is computationally demanding. Therefore, several empirical methods for estimating the coupling values have been developed, which are employed in more complex calculations of electron-transfer processes. These methods are used, for example, in studies of long-range electron transfer in multi-heme protein, where the structural details are affected by relatively large uncertainties [70], or in non-adiabatic molecular dynamics (NAMD) simulations of charge propagation where fast estimation of the coupling element values is crucial [264–268].

Distance decay Interaction between the diabatic states is exponentially decaying with the growing distance d between the donor and acceptor centers

$$|H_{ab}| = A \exp\left[-\beta d/2\right] \tag{72}$$

Value of the decay factor β is characteristic for different types of molecular systems. Its value, together with the pre-exponential factor A, are obtained by fitting of experimental data or computed data from higher-level methods. Then, the decay law (72) is used to predict the coupling values at various distances.

Correlation with the overlap The decay law (72) captures well the long-range distance regions where specific shapes of donor/acceptor centers can be disregarded. However, structural orientations together with localization of the molecular orbitals participating in the given electron transfer process are important. These effect are naturally described by overlap integrals

$$S_{ab} = \langle \psi_a | \psi_b \rangle \tag{73}$$

Therefore, more accurate empirical estimates do not fit the coupling values to distances but their assume their linear dependence on the overlaps [256, 269]

$$H_{ab} = C S_{ab} \tag{74}$$

The scaling factor C is obtained by fitting of accurate quantum-chemistry or density-functional-theory data.

For example, in the analytic overlap method (AOM) [269], which is used for non-adiabatic charge-transfer studies of organic crystals, the factor $C = 1.819$ eV is used, obtained by fit to 43 data points. This factor is applicable on π-conjugated hydrocarbon

homo-dimers, where the overlap S_{ab} is evaluated for the diabatic states projected to optimized minimal Slater basis set. Recently, the AOM was extended to polyaromatic hydrocarbons with heteroatoms [270], and it is used for simulations of charge propagation in organic semiconductors [84, 267].

3.3.2 Generalized Mulliken-Hush (GMH) method

The Mulliken-Hush method [49, 271] is based on the two-state model and it relates the electronic coupling element H_{ab} to the adiabatic transition moment $\boldsymbol{\mu}_{01}$:

$$|H_{ab}| = \frac{|\boldsymbol{\mu}_{01}|\Delta E_{ab}}{|\Delta\boldsymbol{\mu}_{ab}|} \tag{75}$$

where $\Delta E_{ab} = E_b - E_a$ is the diabatic energy gap and $\Delta\boldsymbol{\mu}_{ab} = \boldsymbol{\mu}_b - \boldsymbol{\mu}_a$ is the difference between the diabatic dipole moments. The diabatic energy gap can be approximated by excitation energy $\Delta E_{01} = h\nu_{01}$, $\Delta\boldsymbol{\mu}_{ab}$ is well described by the distance between the two charge centers $e\boldsymbol{R}_{ab}$, and the transition moment is directly related to the oscillatory strength, which is proportional to the corresponding absorption peak area. Therefore, the Mulliken-Hush expression is often used to extract the coupling values from the spectroscopic measurements. [49, 272, 273]

In generalized Mulliken-Hush (GMH), unitary transformation diagonalizing the dipole moment matrix is applied to the adiabatic two-state Hamiltonian. [274, 275] This leads to expression

$$|H_{ab}| = \frac{|\boldsymbol{\mu}_{01}|\Delta E_{01}}{\sqrt{(\boldsymbol{\mu}_{00} - \boldsymbol{\mu}_{11})^2 + 4(\boldsymbol{\mu}_{01})^2}} \tag{76}$$

where the diabatic electronic coupling is related only to adiabatic energies and transition dipoles. The relation can be thus easily implemented in standard quantum chemistry codes where the adiabatic quantities are directly available (note that for the self-exchange ET in homo-dimers the GMH expression reduces to the half-splitting formula (69)). Therefore, the GMH method is often used for high-level calculations of electronic coupling elements between selected states of small molecules. [253–256, 276–281]

Fragment charge differences When the charge transitions lead to well separated diabatic states ψ_a, ψ_b, with negligible overlap S_{ab}, it is more natural to express the electronic coupling in terms of charges localized on the donor/acceptor centers rather than dipole moments. Such approach is known as fragment charge differences (FCD) [282] and the

expression for the coupling elements is formally analogous to GMH

$$|H_{ab}| = \frac{|\Delta q_{01}|\Delta E_{01}}{\sqrt{(\Delta q_0 - \Delta q_1)^2 + 4(\Delta q_{01})^2}} \tag{77}$$

Here, the Δq_0 and Δq_1 are the charge differences between the donor and the acceptor regions in the ground and first excited states, respectively, while the Δq_{01} denotes the adiabatic cross term. These charges can obtained from the expansion coefficients of electronic states in localized basis sets which are readily available in quantum chemistry codes, or by projection to donor/acceptor regions in plane wave codes.

Fragment energy differences The idea of obtaining the coupling elements by diagonalizing dipole and charge matrices in GMH and FCD methods, respectively, was later used also for computing a Coulomb coupling in excitation energy transfer (EET) [283]. The adiabatic electronic Hamiltonian is now transformed by unitary matrix diagonalizing the matrix of transition density differences between donor/acceptor regions for the $m \rightarrow n$ excitation. Again, this leads to the coupling expression formally analogous to GMH

$$|H_{ab}| = \frac{|\Delta x_{mn}|\Delta E_{mn}}{\sqrt{(\Delta x_m - \Delta x_n)^2 + 4(\Delta x_{mn})^2}}. \tag{78}$$

This method is known as fragment energy differences (FED) [283, 284] and it has been used in various studies of photoexcitations in biomolecules [285–288] and organic semiconductors [289–291].

3.3.3 Constrained density functional theory (CDFT)

Conventional DFT exchange-correlation functionals suffer from self-interaction error [292–295], which leads to artificial delocalization of adiabatic Kohn-Sham (KS) states. Construction of localized diabatic states is thus almost impossible in DFT without special optimization techniques. In the so-called constrained density functional theory (CDFT) [296–298], the localization of the charge density in a desired region is forced by applying a charge constraint N_c on the system as an integral of charge density $n(\boldsymbol{r})$ weighted by a function $w(\boldsymbol{r})$ defining the donor and acceptor regions,

$$N_c = \int w(\boldsymbol{r})n(\boldsymbol{r})d\boldsymbol{r}. \tag{79}$$

The Lagrange multiplier technique is then applied to add this constraint to the energy functional

$$W[n,V] = E[n] + V\left(\int w(\boldsymbol{r})n(\boldsymbol{r})d\boldsymbol{r} - N_c\right). \tag{80}$$

The resulting new functional $W[n,V]$ is minimized with respect to the charge density n and maximized with respect to the Lagrange multiplier V. The latter can be interpreted as the external potential needed to enforce the constraint N_c.

To obtain the electronic coupling matrix element, the diabatic states are chosen to be the Kohn-Sham determinants ψ_a, ψ_b resulting from the constrained energy minimization described above. Within this approximation the two-state Hamiltonian matrix has the following form

$$\mathbb{H}' = \begin{pmatrix} E_a & F_bS_{ab} - V_bW_{ab} \\ F_aS_{ab} - V_aW_{ab} & E_b \end{pmatrix}. \tag{81}$$

While there are diabatic energies $E_\alpha = \langle\psi_\alpha|\,\hat{H}_\alpha^{\mathrm{KS}}\,|\psi_\alpha\rangle$ on the diagonal, the off-diagonal terms contain diabatic potential energies $F_\alpha = \langle\psi_\alpha|\,\hat{H}_\alpha^{\mathrm{KS}} + V_\alpha\sum_i w(\boldsymbol{r}_i)\,|\psi_\alpha\rangle$ involving the interaction with the external potential, diabatic-state overlap $S_{ab} = \langle\psi_a|\psi_b\rangle$, and the weight function matrix element $W_{ab} = \langle\psi_a|\sum_i w(\boldsymbol{r}_i)\,|\psi_b\rangle$. The Hamiltonian matrix is then transformed into the orthogonal diabatic states, which are eigenstates of the weight matrix $\mathbb{W}$. These are obtained by solving the general eigenvalue problem

$$\mathbb{W}\cdot\mathbb{V} = \mathbb{S}\cdot\mathbb{V}\cdot\mathbb{L}, \tag{82}$$

where the diagonal $\mathbb{L}$ matrix contains the eigenvalues and the unitary matrix $\mathbb{V}$ is constructed from the generalized eigenfunctions of $\mathbb{W}$. Finally, the desired H_{ab} elements are the off-diagonal elements of the transformed Hamiltonian $\mathbb{H} = \mathbb{V}^\dagger\cdot\mathbb{H}'\cdot\mathbb{V}$.

3.3.4 Fragment orbital density functional theory (FODFT)

The opposite approach to CDFT represent fragment orbital density functional theory (FODFT) [299–302] where the KS wavefunctions are calculated on isolated donor/acceptor fragments in their reduced forms, neglecting their mutual interaction. The diabatic states are constructed from these donor/acceptor orbitals. Assuming that there are N occupied orbitals of reduced donor $\{\phi_{\mathrm{D}}^1,\ldots,\phi_{\mathrm{D}}^N\}$ and M occupied orbitals of reduced acceptor $\{\phi_{\mathrm{A}}^1,\ldots,\phi_{\mathrm{A}}^M\}$ then we can write the approximate diabatic states as Slater determinants

of the combined $N + M - 1$ states

$$\psi_a^{\mathrm{DA}} = [(N+M-1)!]^{-1/2} \det\left[\phi_{\mathrm{D}}^1, \ldots, \phi_{\mathrm{D}}^{N-1}, \phi_{\mathrm{A}}^1, \ldots, \phi_{\mathrm{A}}^M\right] \quad (83a)$$

$$\psi_b^{\mathrm{DA}} = [(N+M-1)!]^{-1/2} \det\left[\phi_{\mathrm{D}}^1, \ldots, \phi_{\mathrm{D}}^N, \phi_{\mathrm{A}}^1, \ldots, \phi_{\mathrm{A}}^{M-1}\right] \quad (83b)$$

for the case of $\mathrm{D}^- + \mathrm{A} \rightarrow \mathrm{D} + \mathrm{A}^-$ electron transfer. Because the KS Hamiltonian is constructed from one-particle state-dependent operators $\hat{H}_\alpha^{\mathrm{KS}} = \sum_i^{N+M-1} \hat{h}_{\alpha,i}^{\mathrm{KS}}$ and the diabatic-state determinants differ only in the highest occupied orbitals, the electronic coupling element is according to the Slater-Condon rules equal to the integral over these two orbitals only [303]

$$H_{ab} = \left\langle \psi_a^{\mathrm{DA}} \right| \hat{H}_b^{\mathrm{KS}} \left| \psi_b^{\mathrm{DA}} \right\rangle = \left\langle \phi_{\mathrm{D}}^N \right| \hat{h}_b^{\mathrm{KS}} \left| \phi_{\mathrm{A}}^M \right\rangle . \quad (84)$$

The complementary elements H_{ab} and H_{ba} can in principle differ in asymmetric charge-transfer systems, where the donor/acceptor fragments are not identical, and their average is then taken as the resulting electronic coupling matrix element.

3.3.5 Projector-operator based diabatization (POD)

All the computational approaches for the coupling calculations reviewed above are designed for single-electron transfer between the electron donor and acceptor molecules. However, to investigate electron transfer on heterogenous interfaces with solid-state surfaces, like in electrochemistry or nanoelectronics, efficient and accurate calculation of all the coupling elements between the surface and molecular states is needed. For this purposes, the projector-operator based diabatization (POD) method was developed [304].

The POD method constructs the localized charge states from the Kohn-Sham (KS) adiabatic states

$$\hat{H} \left| \psi_i \right\rangle = \epsilon_i \left| \psi_i \right\rangle , \quad (85)$$

which are obtained by standard SCF calculations. Without loss of generality, the adiabatic states can be represented in an orthonormalized basis set of atom-center localized functions $\{\phi_i\}$. Partitioning the system to donor/acceptor fragments, the Hamiltonian matrix can be reordered to block structure

$$\tilde{\mathbb{H}} = \begin{pmatrix} \tilde{\mathbb{H}}_{DD} & \tilde{\mathbb{H}}_{DA} \\ \tilde{\mathbb{H}}_{AD} & \tilde{\mathbb{H}}_{AA} \end{pmatrix} . \quad (86)$$

The desired localized charge-transfer states are obtained by diagonalization of the diagonal

blocks, $\tilde{\mathbb{H}}_{\alpha\alpha}$ (α = D,A), while the off-diagonal blocks are transformed correspondingly:

$$\bar{\mathbb{H}}_{\alpha\alpha} = \mathbb{U}_{\alpha}^{\dagger} \cdot \tilde{\mathbb{H}}_{\alpha\alpha} \cdot \mathbb{U}_{\alpha}, \tag{87a}$$

$$\bar{\mathbb{H}}_{\alpha\beta} = \mathbb{U}_{\alpha}^{\dagger} \cdot \tilde{\mathbb{H}}_{\alpha\beta} \cdot \mathbb{U}_{\beta}. \tag{87b}$$

By this unitary transformation the system Hamiltonian is transformed to the following form

$$\bar{\mathbb{H}} = \begin{pmatrix} \bar{\mathbb{H}}_{DD} & \bar{\mathbb{H}}_{DA} \\ \bar{\mathbb{H}}_{AD} & \bar{\mathbb{H}}_{AA} \end{pmatrix} = \begin{pmatrix} \epsilon_{D,1} & \dots & 0 & & & \\ \vdots & \ddots & \vdots & & \bar{H}_{DA} & \\ 0 & \dots & \epsilon_{D,N} & & & \\ & & & \epsilon_{A,1} & \dots & 0 \\ & \bar{H}_{AD} & & \vdots & \ddots & \vdots \\ & & & 0 & \dots & \epsilon_{A,M} \end{pmatrix}. \tag{88}$$

While there are N donor and M acceptor one–electron energies $\epsilon_{\alpha,i}$ of diabatic states on the main diagonal, the off-diagonal blocks $\bar{\mathbb{H}}_{\alpha\beta}$ contain electronic coupling elements between the corresponding states.

The POD method was implemented [87, 305] by the author of this thesis to CP2K software package [306–308] and its accuracy was assessed on the HAB7^{-}, HAB11, and HAB79 data sets [253, 254, 256]. For the Kohn-Sham calculations performed with range-separated hybrid functionals such as LRC-wPBEh [309–311] and wB97XD [312, 313], the method provides electronic coupling values in excellent agreement with high-level *ab initio* calculations, giving a mean relative unsigned error of ∼5%. The procedure was shown to be less accurate for large numerical basis sets, however, the accuracy is regained in the POD2L variant [314]. The method was later employed as a reference for the AOM parametrization [269, 270] and used for studies of electron transfer kinetics in multi-heme proteins [68, 72, 201, 315] and their heterogeneous junctions [36].

3.4 Electron hopping simulations

The key factors for electron-hopping simulations are the free energy difference ΔG between the D/A pairs, the reorganization free energy λ, and the electronic coupling H_{ab}. These determine the rate constants (6) entering the master equations (8).

Cluster models The free energy differences are related to experimentally measurable redox potentials E by the Nerst equation [109]

$$E = E^0 - \frac{\Delta G - \Delta G^0}{nF} \tag{89}$$

where F is the Faraday constant, ΔG^0 denotes the free energy change in the standard state (concentrations 1 mol/l, pressure 1 atm, temperature 25 °C), and E_0 is the standard potential. The experimental redox potentials are referenced to standard hydrogen electrode (SHE), which has the absolute potential ∼4.44 V [316].

Computationally, the redox potentials are often computed on cluster models of the studied D/A pairs [317–325] These models often utilize the continuous screening approximation of the surrounding environment based on the Poisson equation, usually referred as implicit solvent [326–331]. The curvature of the free energy surfaces, i.e. the reorganization free energy, is typically estimated from ionization energies evaluated on the D/A sites, which is the procedure known as a four-point scheme [332–334].

Extended models The cluster approaches are performing well for D/A pairs in solution, however, they tend to be inaccurate for the biomolecular electron transfer. The redox sites in biomolecules are typically restrained by steric effects and influenced by oriented intrinsic electric fields induced by the surrounding molecular environment, which cannot be captured by implicit solvent models. However, the localized nature of the hopping electron-transfer mechanism allows application of the hybrid computational approaches such as quantum-mechanical / molecular mechanical (QM/MM) method [335–341] or perturbed matrix method (PMM) [342–346], where the redox sites are treated at higher level of theory than the rest of the molecules. At this level, the free energies can be estimated from optimized structures like in the cluster models or evaluated by the molecular-dynamics techniques reviewed in Sec. 3.2 [347–354].

However, in the electron-transfer studies, the reaction coordinate or collective variable used for the free energy calculations, can be set as the vertical ionization energy gap [252]

$$\Delta E = E_{\mathrm{Ox}}(\boldsymbol{R}^N) - E_{\mathrm{Red}}(\boldsymbol{R}^N) \tag{90}$$

where $\boldsymbol{R}^N = \{\boldsymbol{R}_1, \ldots, \boldsymbol{R}_N\}$ denotes the coordinates of the N-particle molecular system. The free energy profile of the state $M = \{\mathrm{Red}, \mathrm{Ox}\}$ is then

$$A(\Delta E') = -k_B T \ln \left\langle \delta(\Delta E(\boldsymbol{R}^N) - \Delta E') \right\rangle_M \tag{91}$$

fulfilling the linear free energy relation

$$A_{\mathrm{Ox}}(\Delta E) - A_{\mathrm{Red}}(\Delta E) = \Delta E \tag{92}$$

The reorganization free energy is directly related to the variance of the energy-gap distributions $\sigma_M^2 = \langle(\Delta E - \langle\Delta E\rangle_M)^2\rangle_M$

$$\lambda_M^{\mathrm{var}} = \frac{\sigma^2}{2k_BT} \tag{93}$$

When these distributions are Gaussian, the free energy curves have parabolic shapes, following the Marcus theory, and the linear response approximation can be applied in the thermodynamic integration. This significantly simplifies the calculations, because in the linear-response regime the free energy change and the reorganization free energy are fully determined by the mean vertical energy gaps at the initial and final states

$$\Delta A = \frac{1}{2}\left[\langle\Delta E\rangle_{\mathrm{Ox}} + \langle\Delta E\rangle_{\mathrm{Red}}\right] \tag{94}$$

$$\lambda^{\mathrm{St}} = \frac{1}{2}\left[\langle\Delta E\rangle_{\mathrm{Ox}} - \langle\Delta E\rangle_{\mathrm{Red}}\right] \tag{95}$$

This approach have been successfully applied to study electron transfer in various redox active biomolecules, in particular metalloproteins [11, 100, 355–358].

3.5 Electron tunneling calculations

The tunneling current through molecular junctions are usually computed by NEGF technique (Sec. 2.2.2), while Landauer-Büttiker formalism in Breit-Wigner approximation (Sec. 2.2.1) can be applied to larger biomolecular junctions. Nevertheless, all approaches require full quantum treatment of the model.

Here, we focus on the latter case of large junctions involving biomolecules with thousands of atoms, for which we developed the state-of-the-art computational procedure [36, 41]. After preparing the junction structure by molecular dynamics techniques, the projection-operator diabatization (POD) method [87], implemented in CP2K software package by our group, is employed to localize Kohn-Sham (KS) DFT electronic states on the system fragments (left electrode L, scattering region S containing the molecule, and right electrode R). The method also provides the electronic coupling elements H_{mj} between metallic states m and scattering states j.

Localization Technically, the KS Hamiltonian is transformed to orthonormalized basis set of atom-center localized functions $\{\phi_i\}$ and rearranged to the following block structure [36, 41]

$$\tilde{\mathbb{H}} = \begin{bmatrix} \tilde{\mathbb{H}}_{LL} & \tilde{\mathbb{H}}_{LS} & \tilde{\mathbb{H}}_{LR} \\ \tilde{\mathbb{H}}_{SL} & \tilde{\mathbb{H}}_{SS} & \tilde{\mathbb{H}}_{SR} \\ \tilde{\mathbb{H}}_{RL} & \tilde{\mathbb{H}}_{RS} & \tilde{\mathbb{H}}_{RR} \end{bmatrix} \tag{96}$$

and then transformed to the following form by series of block diagonalizations $\bar{\mathbb{H}}_{\mu\mu} = \mathbb{U}_\mu^\dagger \cdot \tilde{\mathbb{H}}_{\mu\mu} \cdot \mathbb{U}_\mu$ and transformations $\bar{\mathbb{H}}_{\mu\nu} = \mathbb{U}_\mu^\dagger \cdot \tilde{\mathbb{H}}_{\mu\nu} \cdot \mathbb{U}_\nu$, $\mu, \nu \in \{L, S, R\}$

$$\bar{\mathbb{H}} = \begin{bmatrix} \epsilon_{L,1} & \dots & 0 & & & & & & \\ \vdots & \ddots & \vdots & & \bar{\mathbb{H}}_{LS} & & & \bar{\mathbb{H}}_{LR} & \\ 0 & \dots & \epsilon_{L,N_L} & & & & & & \\ & & & \epsilon_{S,1} & \dots & 0 & & & \\ & \bar{\mathbb{H}}_{SL} & & \vdots & \ddots & \vdots & & \bar{\mathbb{H}}_{SR} & \\ & & & 0 & \dots & \epsilon_{S,N_S} & & & \\ & & & & & & \epsilon_{R,1} & \dots & 0 \\ & \bar{\mathbb{H}}_{RL} & & & \bar{\mathbb{H}}_{RS} & & \vdots & \ddots & \vdots \\ & & & & & & 0 & \dots & \epsilon_{R,N_R} \end{bmatrix} \tag{97}$$

The diabatic state energies are located on the main diagonal, while the off-diagonal blocks contain the electronic coupling elements. In practice, the $\bar{\mathbb{H}}_{LR}$ blocks are not evaluated because the direct tunneling between L, R electrodes is not considered.

Band alignment The DFT calculations are performed at GGA level, which can relatively well describe both the metallic and molecule states. However, due to the self-interaction error and the lack of image-charge interactions, the molecular states are incorrectly places with respect to the Fermi level E_F of the metal electrodes in GGA. Typically, the valence band edge, i.e. molecular HOMO, is aligned to E_F, although in reality there should be offset between these states at the bio/metallic interface. We use the DFT+Σ [115, 121, 359] approach to correct these deficiencies.

In general, each molecular orbital energy $\epsilon_{S,j}$ deviates from the accurate reference value $\epsilon^0_{S,j}$ by an energy shift $\Sigma_{S,j}$. In DFT+Σ this shift is decomposed to

$$\epsilon_{\Sigma_j} = \epsilon_{S,j} + \Sigma_{S,j} \tag{98}$$

$$\Sigma_{S,j} = \Sigma^0_{S,j} + \Sigma^{pol}_{S,j}, \tag{99}$$

where $\Sigma^0_{S,j}$ is the self-interaction-error correction, while $\Sigma^{pol}_{S,j}$ stands for the polarization, image-charge correction.

The self-interaction error is responsible for the HOMO-LUMO gap underestimation in GGA. To obtain the correct energies of HOMO and LUMO, the optimally tuned range-separated hybrid functionals (OT-RSH) [360–362] are applied on selected parts of the system. On the contrary, the incapability of DFT to capture the image-charge interactions is exhibited by the lack of interfacial state renormalization, i.e. the HOMO-LUMO gap narrowing. The image-charge potential between two metal planes is given by the following series

$$V_{\text{img}}(z) = \frac{q}{4\pi\epsilon_0} \sum_{n=-\infty}^{\infty} \left(\frac{1}{|z - 2nd - z_0|} - \frac{1}{|z - 2nd + z_0|} \right), \tag{100}$$

where q is the charge of the particle and d is the distance between the two surface planes. The offset z_0 is obtained by the fitting of V_{img} to exchange-correlation potential V_{XC} obtained from DFT. Then, the polarization corrections can be obtained by integration of the given molecular orbitals $\psi_{S,j}$ in the image-charge potential

$$\Sigma^{pol}_{S,j} = q \int_V |\psi_{S,j}(\mathbf{r})|^2 V_{\text{img}}(\mathbf{r}) d\mathrm{r}^3 \tag{101}$$

Obviously, the DFT+Σ is applicable only on weakly interacting systems where the frontier orbitals are not hybridized with the metallic state.

4 Methodology development

4.1 Double-QM/MM method

Conventional QM/MM techniques partition the system to the inner part, described at QM level of theory, and the outer part parametrized by a MM potential. Therefore, when applied on the ET processes, the method is limited to the half-reaction description where either the oxidation of an electron donor or the reduction of an electron acceptor is simulated.

$$\mathrm{D} \rightarrow \mathrm{D}^{+} + e, \qquad \mathrm{A} + e \rightarrow \mathrm{A}^{-} \tag{102}$$

As a result, the donor and acceptor do not interact with each other and the ET process is studied in the so-called dilute limit.

However, the rate of the electron transfer reaction is of course distance dependent. The free energy barrier increases with the growing distances due to the reorganization free energy dependence on the donor–acceptor distance. On the other hand, the electronic coupling between the two redox centers is exponentially decaying with the increasing distance. These effects need to be considered when the full ET reactions at finite distances are investigated

$$\mathrm{D} + \mathrm{A} \rightarrow \mathrm{D}^{+} + \mathrm{A}^{-} \tag{103}$$

This is typical for example for the intra-molecular ET where the distance between the two centers is restrained by the bridging chemical groups and surrounded molecular environment.

Although the full reactions are conceptually easier to investigate because one does not need to deal with the unknown electrochemical potential of solvated electron, in practice, stabilization of a desired diabatic charge states is computationally difficult. At full QM description, constrained density functional theory (CDFT) can be applied, however, this approach is limited by the size of the system and chemical properties of the donor and acceptor regions. For example, high-spin states or more complicated electronic structures, like anti-ferromagnetic configuration of the iron-sulfur clusters present in many important metalloproteins, cannot be maintained by CDFT.

Therefore, we developed the so-called multiple-QM/MM technique with generalized QM/MM partitioning where more than one inner part can be defined within the same outer part [363]. For the case of two inner parts (double-QM/MM, see Figure 6) the method can be applied to the full ET reactions. Thanks to the chosen partitioning with well defined boundaries of the inner parts, the charge density is naturally localized in

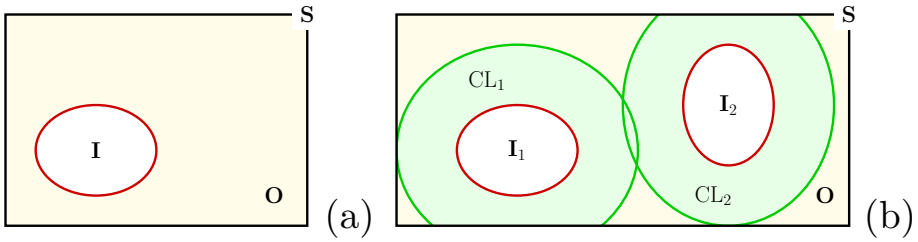

Figure 6: Schematic illustration of QM/MM partitioning: (a) conventional QM/MM where the whole system S is divided into the QM inner part (I) and the MM outer part (O), (b) the double-QM/MM method with two inner parts surrounded by the common outer part. The charge layers (CL) used for electrostatic embedding are shown as green regions.

desired regions and its spin state can be easily controlled. The method is limited to the outer–sphere description where the two redox regions are separated and therefore applicable on non-adiabatic electron hopping described by Marcus theory.

The method was implemented in the QMS software [364], which is a program interface for coupling QM and MM software to perform QM/MM calculations, coded by the author of the thesis. QMS is based on the subtractive QM/MM scheme where the MM energies of inner parts are substituted by the QM energy contributions

$$E_{\mathrm{QM/MM}}(\mathrm{S}) = E_{\mathrm{MM}}(\mathrm{S}) + \sum_{i=1}^{N} \left[E_{\mathrm{QM}}(\mathrm{I}_i) - E_{\mathrm{MM}}(\mathrm{I}_i)\right]. \tag{104}$$

Several optimization methods including steepest descent, conjugate gradient, and L-BFGS algorithms, are implemented in QMS together with molecular dynamics (MD) based on velocity Verlet integration technique. Available stochastic (Andersen, Langevin) and deterministic (Berendsen, Nose-Hoover) thermostats allow temperature control needed for simulations in the canonical NVT ensemble.

The performance of the d-QM/MM method was demonstrated on the cross-ET reaction between iron and ruthenium cations in solution [365]

$$\mathrm{Fe}^{3+} + \mathrm{Ru}^{2+} \rightarrow \mathrm{Fe}^{2+} + \mathrm{Ru}^{3+}. \tag{105}$$

The first hydration shells of the cations were included in the inner parts, forming the hexa-aqua metal complexes. These were treated at DFT level of theory using hybrid functionals, core pseudopotentials and Pople-type basis sets while the explicit water solution was described by classical TIP3P model. Molecular dynamics at d-QM/MM level was run to sample the vertical ionization energies at initial and final states to compute the Marcus free

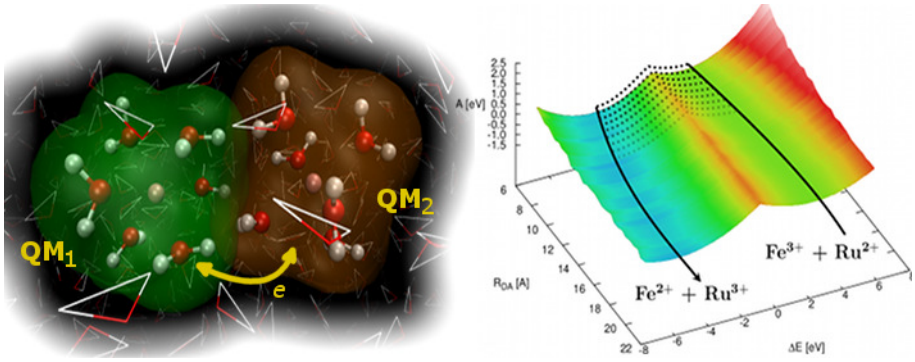

Figure 7: The model of $Ru^{2+/3+}$ and $Fe^{2+/3+}$ cations exchanging electron in the aqueous solution with Cl^- counterions. Reconstructed free energy surface $A(R_{DA}, \Delta E)$ is shown on the right-hand side where the minimum free energy path is shown by a thick black arrow while the dotted lines below 10 Å indicate the region where crossing the barrier is probable.

energy surfaces at different donor–acceptor distances. We showed that the d-QM/MM method converges to conventional QM/MM results at the dilute limit, while the free energy barrier is considerably lowered as the interaction distance is shortened.

4.2 Projector operator-based diabatization (POD) method

The POD method, described in Sec. 3.3.5, was originally designed for quantum dynamics studies of electron transfer on heterogeneous interfaces of organic molecules with semiconductor surfaces [304]. However, we implemented the method into to the CP2K program package [307], and demonstrated in Ref. 87 and 305 that it can also be used for efficient and accurate coupling element calculations in organic-molecule pairs. For example, the coupling element between HOMO and LUMO frontiers in cationic benzene dimer (see Fig. 8) is known to be 435.2 meV at plane interaction distance 3.5 Å and it decays exponentially with the rate 2.85 $Å^{-1}$. Using the POD method on Kohn-Sham wavefunction obtained by a popular hybrid range-separated functional wB97X [313], nearly identical values 429.5 meV and 2.82 $Å^{-1}$, respectively, are obtained [305].

Further, we evaluated the performance and accuracy of the POD method on the HAB11 database of organic homo-dimers (see Fig. 9), which was designed for benchmarking electronic coupling computational level [253]. As other DFT-based methods, such as CDFT or FODFT, also POD accuracy is strongly dependent on applied functional [87]. As in the other cases, the best performance exhibit the hybrid functionals with mixture of DFT and Hartree-Fock (HF) exchange, although the coupling magnitude increases with the fraction of HF exchange in contrast to other approaches where the trend is op-

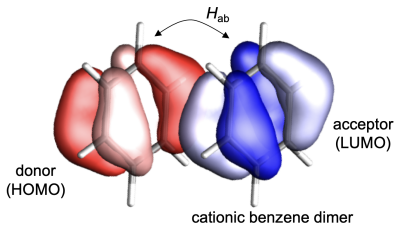

Figure 8: Illustration of electronic interaction (coupling element) between the highest occupied molecular orbital (HOMO, red) and the lowest unoccupied molecular orbital (LUMO, blue) in the co-planar cationic benzene dimer (charge +1).

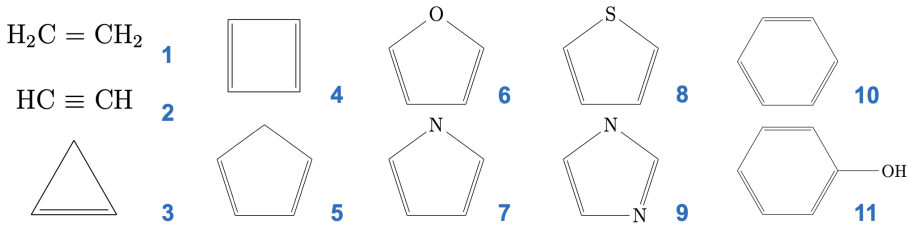

Figure 9: The HAB11 set of organic homo-dimers with +1 positive charge. The database contains high-level quantum-chemistry reference values for the electronic coupling elements at four inter-molecular distances (3.5, 4.0, 4.5, and 5.0 Å), and the corresponding exponential decay β factors.

posite [87, 253]. Naturally, the range-separated hybrid functional, where the Coulomb potential is split into short and long-range parts to capture both the correct chemical character of organic bonds as well as assymptotics of charge density at large distances, are the most suitable for the coupling calculations. The POD methods was shown to have only 5% mean unsigned relative error on HAB11 set compared to high-level, and much more expensive, quantum chemistry techniques [305].

Later, the method was used as a reference in analytic overlap method (AOM) [269, 270], an ultrafast electronic coupling estimator for non-adiabatic molecular dynamics (NAMD) simulations. For that purposes, new HAB79 dataset was designed, containing 921 dimer configurations of organic dimers typical for molecular-crystal electronics [256]. This methodology was then successfully used to simulate polaronic charge transport in organic crystals [84, 267] using the NAMD technique known as fragment orbital-based hopping (FOB-SH) [82, 265, 366].

Besides the organic pairs, the POD method can be applied to such a complex systems as semiconductors with defects or heterogeneous interfaces of molecules with solid surfaces [87] (see Fig. 10), where the other electronic-coupling calculations methods reviewed in Sec. 3.3 are hardly, if at all, applicable. Finally, the post-processing nature of the method and relatively simple evaluation of coupling elements between all the states be-

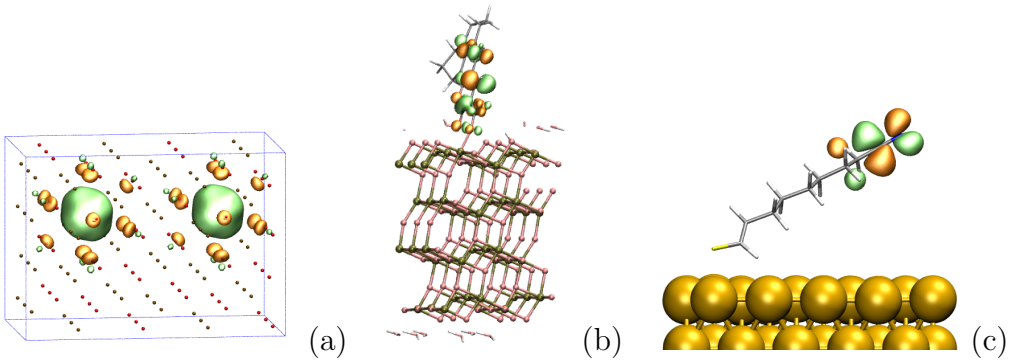

Figure 10: Illustration of applicability of the POD method for electronic coupling element evaluation between (a) semiconductor defects, (b) organic molecules on semiconductor surfaces, (c) and organic molecules on metal surfaces. Localization of Kohn-Sham HOMO is shown by green/orange lobes for each system.

tween considered system parts makes the POD method suitable also for transport studied on molecular junctions between metallic contacts [36, 41].

4.3 Gold-sulfur interactions in GolP-CHARMM force field

Organic molecules and biomolecules can suprisingly often get into contact with solid surfaces. Besides obvious interactions of biological tissues with metal tools, jewelry, and implants, various bioelectrochemical measurements and nanobioelectronic components are directly utilizing properties of such heterogeneous interfaces [173, 367–370]. Biomolecules can be interacting weakly with the surfaces via the so-called physisorption, however, more often they are chemically attached to the surface to prevent the undesired lateral movements. This process, known as chemisorption, can proceed either directly, for example by direct binding of sulfate chemical groups to gold surfaces, or indirectly via suitable organic linkers [371–373].

Regarding the charge transport, interfaces of biomolecules with semiconducting metal-oxide surfaces or conducting metal surfaces are typically studied. While the metal-oxide surfaces often exhibit complex ridged structures and strong hydrogen bonding interactions to the solution, the metal surfaces are usually flat and weakly interacting [374–380]. However, due to the high polarizability of metals, image charge interactions need to be taken into account in simulations of biomolecular adsorption to correctly predict the adsorption structures and interactions energies [381, 382]. To capture these effects on gold surfaces, popular in nanobioelectronics, Iori *et al.* [383, 384] developed a polarizable GolP force field, which is parametrized for quantitative simulations on organo-metallic interfaces.

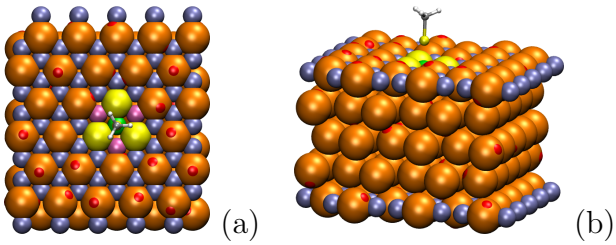

Figure 11: Structure of the model gold slab in (a) top and (b) side views with the chemisorbed methanethiolate as described in GolP-CHARMM force field. The gold atoms are shown as orange balls, surface interface sites are in blue, and the dipole charges in red. The binding-site atom and interface types, where the molecule is bonded, are highlighted in yellow and magenta, respectively.

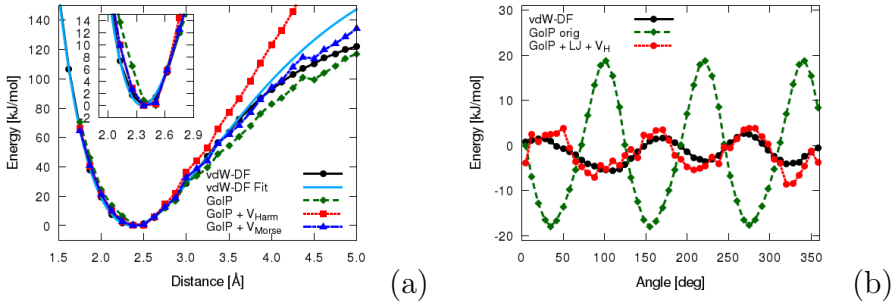

Figure 12: Potential energy profile of (a) the Au-S bonding and (b) rotation around the Au-S bond for cysteinethiolate on the gold surface parametrized in GolP-CHARMM. The reference vdW-DF profiles are indicated by solid black curves, while the dashed green curves show the potential obtained by the original GolP-CHARMM without the modified binding-site types.

The force field was later combined with popular and well-tested CHARMM27 parameter set, designed for biomolecular simulations in aqueous solutions. The resulting GolP-CHARMM force field [385, 386] became very popular for simulations of biomolecules, in particular proteins, with flat gold surfaces [250, 387–390]. However, it allowed to simulate only physisorbing processing, without chemical anchoring of the molecules to the surface. Therefore, we extended the force field by introducing new atomic types for describing Au-S binding sites [391], as shown in Fig. 11.

Besides initial benchmarks of the Au-S interaction potentials on the small sulfur-containing molecules like methanecysteine (c.f. Fig. 11), we focused on accurate description of cysteine binding to gold surfaces [391]. The cysteine residues are often utilized to anchor proteins on gold as they are naturally present in the protein structure either as single thiols or disulfide (S-S) bridges [392–395]. In the latter case, the S-S bonds are known to spontaneously dissociate near the gold surfaces and the resulting thiolates then

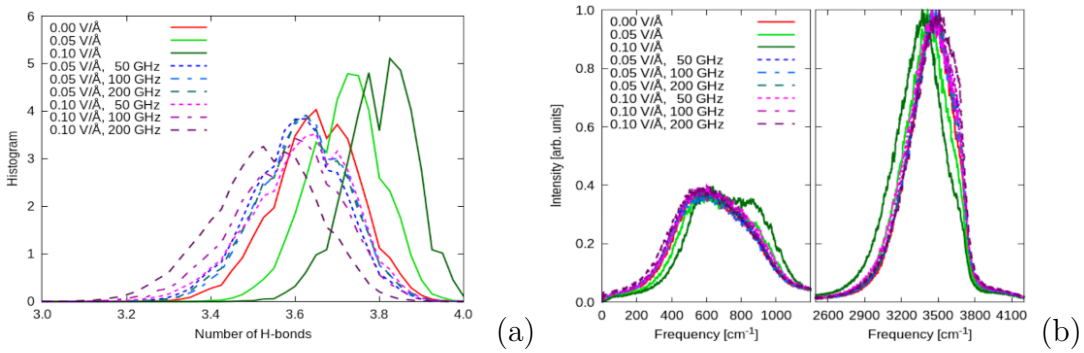

Figure 13: Response of bulk water to applied external electric fields, as obtained from the *ab initio* molecular dynamics. (a) Changes in the mean number of hydrogen bonds per water molecule, and (b) response of the libration and stretching vibrational spectral modes (figures from Ref. [396]).

form the Au-S bonds.

We employ the GolP-CHARMM force field to prepare models of biomolecular junctions, experimentally studied by STM and EC-STM methods [36, 41]. In our pioneering study of small-tetraheme cytochrome (STC) junction, we demonstrated that this force field can well describe such complex structures including chemisorbing interactions [36]. The predicted adsorption structures are in good agreement with experimental AFM scratching measurements of STC monolayer thickness on Au(111) substrates. Moreover, the simulated electronic currents on such structures are in accord not only with the *I*-*V* measurements but also with EC-STM probing of distance decay.

4.4 Ab initio non-equilibrium MD with electric fields

In electrochemical measurements or molecular electronic devices, geometries and electronic structures are affected by external electric fields induced by applied bias potentials. To investigate these effects by atomistic computer simulations, we modified the CP2K software package [307] to implement the time-dependent external electric fields in semi-classical fashion, as described in Sec. 3.2.4. The electric-field intensity in Berry phase formulation [125, 240] is uniform over the simulation cell treated at DFT level, however, its magnitude is harmonically varying in time with given angular frequency [396]. The modified code thus allows simulations of molecular systems not only under static but also oscillatory external electric fields.

Nevertheless, due to the flexible nature of the most of the molecular systems, especially biomolecules in solutions, molecular dynamics and statistical techniques need to be employed to study even the effects of static fields. On the other hand, the DFT-

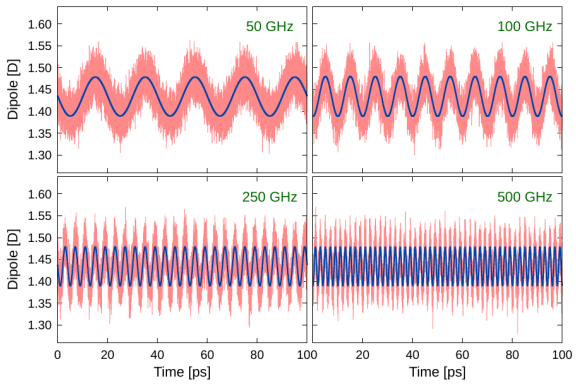

Figure 14: Dipolar response of the ice VII within 100 ps first-principles dynamics affected by oscillating electric field of RMS magnitude 0.2Å and frequencies 50, 100, 250, and 500 GHz. The detected collective dipole is shown in red while the fitted harmonic functions are in blue.

based first-principles MD simulations are computationally very demanding, applicably on relatively small systems only, and limited to short simulations times (typically tens of picoseconds), insufficient to capture the field responses with longer relaxation times. Therefore, we combined the external field implementation with the so-called second generation Car-Parrinello dynamics, developed by Kuhne and Parrinello [397, 398]. This dynamics is in fact based on Born-Oppenheimer approach, however, the instead of full SCF solution of Kohn-Sham equations at each time step, the new solution is estimated by the always stable predictor-corrector (ASPC) method [399], iteratively improved up to pre-set accuracy, and modified by stochastic Langevin thermostat ensuring the long-time stability. In this way, these first-principles MD simulations can be extended to hundreds of picoseconds [396, 400–402].

We demonstrated the performance of this approach on bulk water simulations [396]. Using the correlation-corrected optB88-vdW density functional [403–405], which can well describe the liquid structure of water [406–408], we carried out the room-temperature NEMD simulations with static and oscillatory electric fields of various magnitudes and frequencies. The 100 ps trajectories were obtained, long enough to capture response effects of fields with frequencies 50 GHz and higher. The statistically analyses applied on these trajectories then proved that even the fields of 0.05 V/Å intensities, which are small compared to intrinsic field magnitudes in bulk water (1.5 – 2.5 V/Å [409]), affects the structure of liquid water. While the static fields tend to increase the water ordering, which is exhibited by larger number of hydrogen bonds (see Fig. 13a), the oscillatory field influence the molecular vibrations at both intra- and inter-molecular levels (Fig. 13b).

Later, we applied the time-varying electric fields to study the dielectric properties of

ice VII, which is a high-pressure phase of water [410,411] that can be found on some Solar-system exoplanets [412, 413]. In contrast to standard hexagonal ice, the dipole moments of individual molecules are ordered along the external field direction and the structural constraints considerably hinder their thermal fluctuations. Therefore, the applied oscillatory electric fields at first-principles level of theory can probe the electronic polarization by tracking the responses of the collective dipole of such system, as shown in Fig. 14 [402]. In contrast to liquid phase, these electronic changes have little effect on the vibrations, although the static fields can promote the splitting of the symmetric and antisymmetric stretching modes.

5 Applications to biologically relevant systems

5.1 Ergodicity of ET in redox proteins

One of the key assumptions of the Marcus theory, which is usually employed as the theoretical framework for computational studies of electron-transfer events in redox proteins, is the ergodicity. The transfer events must be divided by long enough time intervals so the protein structure and the surrounding aqueous solution can adapt to the changed electrostatic potential and reach the equilibrium state. Only in such case, different structural configurations are populated in accord with the Boltzmann distribution, the processes follow exponential dynamical behaviour, and the Marcus theory is valid. [11, 46, 47]

Typically, the ergodicity is violated in systems with high transfer rates where the transient times are on femtosecond timescales, for example, in rapid charge flow in photosystems or artificially photosensitized proteins. [97, 98, 414–418] During such short times these proteins do not fully relax to the equilibrium and the transferred charge thus moves to another site from the non-equilibrium, high-energy state. This effectively reduces the reorganization free energies and free energy barriers to lower values that would be predicted by the Marcus theory, and modified theoretical descriptions were developed to capture these situations. [94, 419, 420] However, when the electronic coupling is low compared to the barrier height, the hopping mechanics can be still applied using the corrections for the reorganization free energy based on the spectral decomposition. In other cases, non-adiabatic molecular-dynamics approaches need to be applied. [63, 67, 421, 422]

On the other hand, proteins, due to their soft-matter nature, might undergo relatively slow motions and structural changes similar to glass transitions, which could exceed nano- or even microsecond timescales. As the typical electron-transfer evens proceed in times less then 1 ns, the ergodicity could not be assumed in such proteins. This problem was theoretically investigated by Matyushov [90, 95, 99, 423–428], who generalized the Marcus theory by introducing reaction reorganization energy $\lambda^r = (\lambda^{\mathrm{St}})^2/\lambda^{\mathrm{var}} < \lambda^{\mathrm{St}}$. In contrast to Marcus theory, the separation of free energy surfaces does not correspond to their steepness and the free free energy barrier lower lowered (c.f. Fig. 15a). Based on this behavior, Matyushov formulated a hypothesis that the slow motions of redox proteins are utilized by Nature to optimize the electron-transfer efficiency in redox chains.

However, some of the Matyushov's predictions are rather controversial. For example, significant reduction of the cytochrome c reorganization free energy to 0.57 eV due to the alleged large discrepancy between the λ^{St} and λ^{var} was reported. Although this value is close to the mean experimental value from the aqueous-solution measurements,

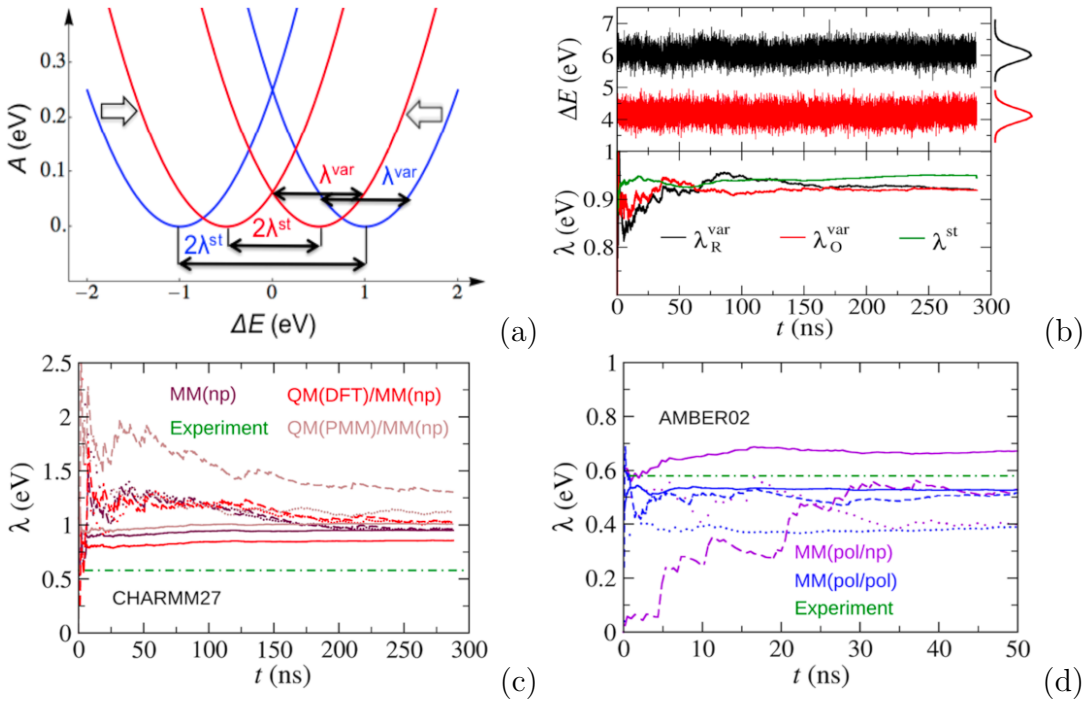

Figure 15: (a) Effect of the ergodicity violation on the Marcus free energy curves. Due to the insufficient relaxation, the Stokes λ^{St} is lower that variational λ^{var}, which is exhibited by shift of the free-energy parabolas and lowering the barrier (red) comparing to the Marcus theory (blue). (b) Time series of vertical ionization energies ΔE obtained by PMM on Cytochrome c and convergence of λ. (c) Comparison of λ obtained by different computational approaches with experimental value for the Cytochrome c. (d) The same comparison for polarizable force fields.

0.6 eV [5, 429–432] and lower than typical reoganization free energies of redox proteins (0.7–1.2 eV [11]), slow glassy-like transition in the cytochrome c structure are improbable. Cytochrome c is a small globular protein, formed by a peptide chain of 104 amino acids folded around the redox-active heme cofactor [433], for which standard behaviour in accordance with the Marcus theory could be expected. Therefore, we reinvestigated the reported non-ergodic effects by extended computer simulations based on long-time MD and sampling in various potentials. [434, 435]

We compared two hybrid-potential approaches, namely QM/MM and PMM, applied on cytochrome c in two different partitioning to schemes and biomolecular force fields to eliminate any computational artifacts. Nevertheless, the λ^{var} consistently converging to λ^{St} was observed in all the cases for both redox states (c.f. Fig 15b here and Table 1 in Ref. 434). The calculated reorganization free energies are overestimated compared to the experimental value (see Fig 15c) due to the lack of electronic polarization in the standard force fields based where the electronic density distributions are approximated by

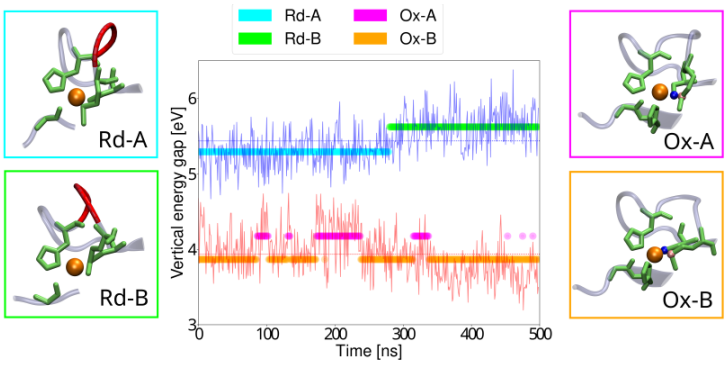

Figure 16: Vertical ionization energy gap (ΔE_M, M = Red, Ox) series on the reduced (blue) and oxidized (red) azurin structure adsorbed on a gold surface. Different configuration states corresponding to twists of a peptide loop near the Cu redox site are indicated by colors (figure taken from Ref. 100).

atomic point charges. Yet, when the polarizable force fields are employed, the λ values are correspondingly reduced and get into accord with the experimental reference (Fig. 15d). Therefore, the numerical evidence for the ergodicity-breaking effects was not observed in the particular case of cytochrome c. [434, 435]

However, it does not mean that the non-ergodic effects cannot occur in biology. On the other, it is quite probable that in more complex and bulky systems, which are typically composed of several protein domains, for example, photosystem II (PSII), the non-ergodicity plays a role in tuning of electron-transfer efficiency. [97, 98] Obviously, investigation of these effects on such extended systems is very difficult and limited by the computational power, as the systems are large, the required simulation times are long ($> \mu$s), and the electronic polarization should be considered.

Further, the non-ergodic effects may become more significant in protein structures incorporated in vacuum nanobioelectronic applications. Recently, we investigated reorganization free energy for azurin oxidation on gold surfaces [100], as electron transfer on such interfaces is being extensively studied by various experimental techniques. [30,35,436–443] During the extensive MD simulations performed on various azurin structures in vacuum and on gold interfaces, we observed that the loss of hydration shell leads to destabilization of relatively flexible peptide loop near the redox site of the protein. The loop flips and twists on ∼100 ns time scales which effectively increases the reorganization free energy. However, as the charge transitions through azurin/gold junction proceed on shorter time scales (∼1 ns), the non-ergodicity can be expected. Nevertheless, the transport properties on bio/metallic interfaces and especially junctions cannot be always interpreted in terms of Marcus theory as the coherent tunneling might play dominant role there. [36, 41]

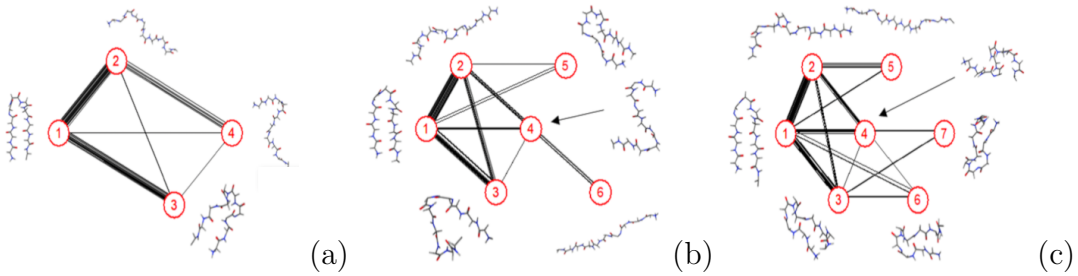

Figure 17: Stable chignolin conformations under (a) zero-field conditions, (b) static electric field of 0.02 V/Å magnitude, and (c) oscillating electric field of 0.02 V/Åmagnitude (r.m.s.) and 2.45 GHz frequency. Probability of the structural transitions is indicated by the crossing line thickness (figures from Ref. [445]).

5.2 Electric field effects on biomolecules

Electric field, comparing to magnetic component of the electromagnetic (e/m) radiation, can relatively strongly interact with the molecular structures. Besides the thermal effects induced by absorption of electric or e/m energy, electron and proton transfer, hydrogen bonding stimulation or disruption, structural and dynamical responses of biomolecules, and other events are often consequences of acting external fields. [126] Surprisingly, microscopic details are not very well known and their investigation were initiated by recently developed state-of-the-art computational and experimental techniques. While the progress in optimization of *ab initio* molecular dynamics (AIMD) methods [397, 398] together with development of Berry-phase formalism [125, 444] allows studying the field effects in solid state matter at quantum level, advanced experimental measurements like vibrational sum-frequency generation (VSFG) provide detail knowledge about molecular-interaction responses to static as well as alternating external fields. [114]

We investigated these effects on chignolin mutant CLN025 [445], which is an artificial minimal protein structure designed for protein folding studies. Chignolin consists of 10 amino acids only that form β-hairpin structure, which undergoes relatively rapid (un)folding transitions between four configurational basins (see Fig. 17a). However, when the structure is perturbed by weak external static electric fields of magnitude 0.02 V/Å, the free energy landscape considerably changes and the structure might appear in seven different configurations (Fig. 17b). These configurations remain (meta)stable even under influence of time-varying fields of the same magnitude and microwave frequency 2.45 GHz, however, the transition probabilities changes (Fig. 17c). Obviously, although the equilibrium chignolin structure is stabilized by hydrogen bonding, the external electric fields can substantially affects its geometry, and the similar effects can be expected on flexible parts of large proteins as well.

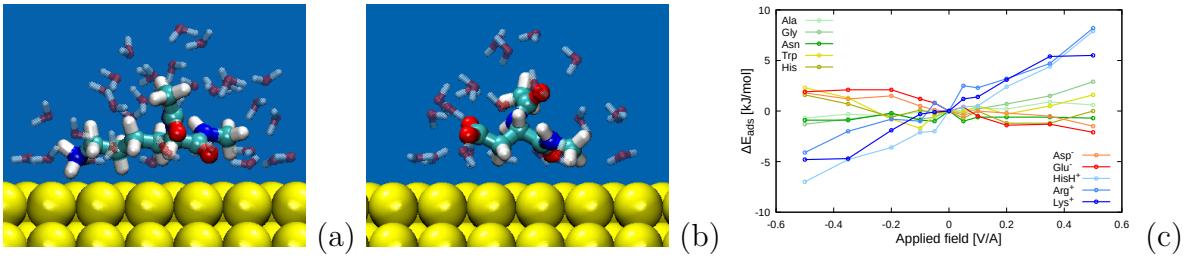

Figure 18: Adsorption structures of (a) lysine and (b) aspartic acid on aqueous gold (111) surface, and (c) response of the adsorption free energies of selected amino acids to external static electric fields (figures from Ref. [250]).

Next, we investigated the external field effects on amino acids adsorbed to aqueous gold surfaces [250], focusing predominantly on 20 proteinogenic structures. The amino acids differ by their side chains, which can have aliphatic or aromatic character, behave as acids, bases, or neutral molecules in aqueous solutions, and could contain specific chemical groups such as hydroxyls, amids, thiols, or thioethers. Naturally, acidic and basic amino acids bear -1 and +1 charge, respectively, in water solutions and respond strongly to the external fields due to the electrostatic interactions. However, we showed that this response is surprisingly considerably larger for the positively charged amino acids than for the negatively charged ones, when they are adsorbed to the gold-electrode surfaces (see Fig. 18). This is effects is caused by different solvation interactions affecting the adsorption structures [250, 391, 446–448] and it is important for understanding structural field responses of biomolecules in electrochemical methods like protein film voltammetry [25–28].

5.3 Long-range ET in multi-heme cytochromes

The recently discovered multi-heme proteins facilitating long-distance extracellular electron transport (EET) in metal-reducing bacteria such as *Shewanella oneidensis* are biomolecules containing well-organized chains of heme cofactors designed by nature for fast and efficient electron transfer (ET) and electron transport (ETp). Similar to chains of multi-heme cytochromes found in *Geobacter sulfurreducens*, these protein can shuttle electrons across the periplasm and outer cell membranes and act as molecular wires [11, 449].

To understand the mechanism of these charge transfer processes, series of computational studies have been performed on two integral proteins MtrF and MtrC located in the bacterial outer membrane (see Fig. 19a), and on small-tetraheme cytochrome (STC) known to carry charge in the periplasm [19,68,70,72,103,201,315,450]. The structure of all these proteins were resolved experimentally by X-ray diffraction methods and their conductive properties are intensively studied by several research groups [20, 21, 69, 451–453].

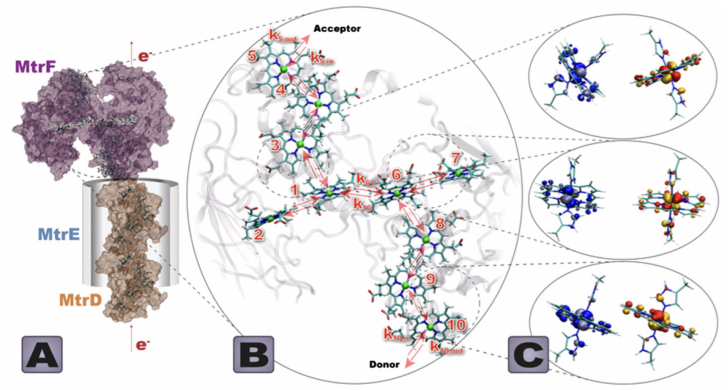

Figure 19: Multiheme cytochromes from *Shewanella oneidensis*: (a) structure of the MtrFDE transmembrane complex, (b) heme cofactor arrangement in MtrF with indicated electron-hopping transitions, and (c) three types of heme pair motifs found in MtrF (T-shaped, coplanar, and stacked). The figure is taken from Ref. 450.

These measurements revealed large number of iron-containing heme cofactors in the cytochrome structures, organized to chains suggesting possible intra-molecular electron-transfer pathways.

We combined classical molecular dynamics (MD) with density functional theory (DFT), as described in Sec. 3.4, to investigate why the long-range electron transfer is so efficient in these multi-heme proteins. Analyzing the redox potentials, reorganization free energies, and the electronic coupling elements, we discovered that not only iron cations but also sulphur in cysteine linkages covalently attached to the heme cofactors play the key roles in the transfer processes [68]. Enhanced charge-density delocalization over the heme planes and cysteine linkages increases the heme-pair rates by 1-2 orders of magnitude in STC [68, 315] and similar effect was found also in MtrF and MtrC proteins as well [72]. Large electronic coupling can kinetically compensate the free energy barriers between cofactors, resulting in large electronic fluxes.

5.4 Charge transfer properties of bio/metallic interfaces

For understanding the electronic charge transfer occurring at heterogeneous interfaces of biomolecules with surfaces of metal electrodes, detail knowledge of their adsorption structures and electronic states is needed. However, these are very difficult to predict computational at quantitative level due to the large structural flexibility of biomolecular systems and extended sizes limiting the application of accurate quantum approaches.

Therefore, first we analyzed such properties of proteinogenic amino acids only, which are the basic building blocks of all proteins [250, 454]. We employed the polarizable GolP-

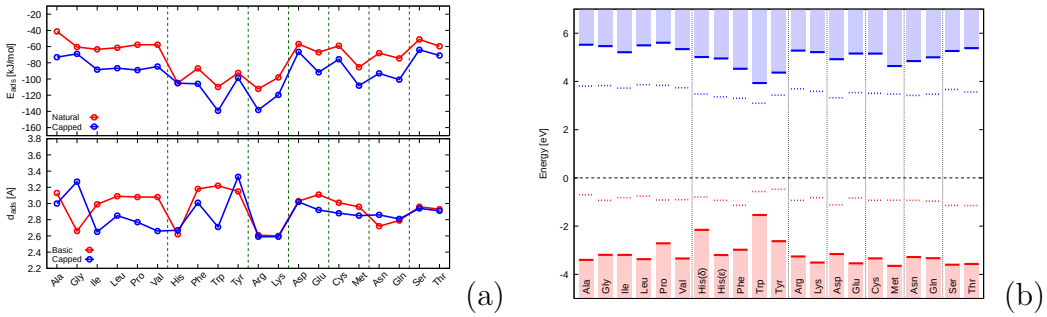

(a) (b)

Figure 20: Interaction of proteinogenic amino acids with vacuum gold (111) surfaces: (a) adsorption energies and distances, electronic-level alignment with respect to the gold Fermi level E_F. The figures are taken from Ref. 454.

CHARMM force field to sample their adsorption structures at gold (111) surfaces, which we then refined by accurate DFT methods based on vdW-DF functionals. This procedure allowed us to determine adsorption energies and interaction distances at gold not only for the natural but also for capped amino acids, mimicing the peptide binding (see Fig. 20a).

Further, we applied the DFT+Σ procedure to establish the electronic-state alignment between frontier HOMO, LUMO energy levels of amino acids and the Fermi level of gold electrodes (see Fig. 20b). Knowledge of these state positions is key for evaluating of charge transfer feasibilities and their mechanisms. Most of the aliphatic amino acids were found unsuitable for electronic hopping as their frontier levels are far from the Fermi level. The exceptions are aromatic histidine, and in particular tryptophane, which have high-energy occupied states suitable for hole transfer.

Then, we started to analyze the gold interface with peptides and proteins. First, we investigated adsorption interactions of chignolin, the 10-amino acid β-hairpin, that unfolds and strongly sticks to the aqueous gold surfaces due to the large contain of aromatic amino acids. Less structural changes at the gold interfaces undergoes insulin, small double-chain protein containing three disulfide bridges stabilizing its geometry. However, the bridges can be dissociate at gold surfaces and the two released thiolates form the Au-S bonds immobilizing the protein structure at the surfaces by relatively strong chemisorption [394, 455–457]

Finally, we studied the gold interactions with azurin [100, 358], the blue-copper redox-active protein often utilized in nanobioelectronic devices (see Fig. 21). Azurin can be directly immobilized at the gold surfaces via a disulfide bridge, which is naturally present in its structure [456, 458]. The protein lies at the surface, maximizing its adsorption interaction by gold contacts with suitable folded β-sheets, while keeping its overall structure , and the copper redox site in particular, relatively well preserved. Nevertheless, we showed

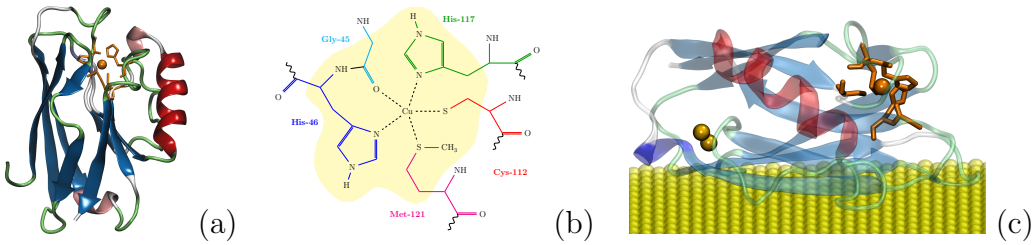

Figure 21: Blue copper protein azurin: (a) crystal structure extracted from *Pseudomonas aeruginosa*, (b) chemical structure of the $Cu^{1+/2+}$ redox site, (c) representative adsorption structures at gold surface. The figures are taken from Ref. 100.

that the reorganization free energy is practically unchanged at vacuum gold interfaces, keeping its ∼0.8 eV value known from solution [459] This, together with the large offset between the azurin and gold electronic states (∼1.8 eV), makes the electron hopping unfavourable in azurin-based gold junctions, where the tunneling currents were detected experimentally.

5.5 Electron transport through protein junctions

Rapid development of single-molecular-junction technologies in recent years and their applicability to protein junctions allows measurements of electric conductivities on single-molecular level [42, 44, 370, 460, 461]. This was demonstrated on blue-copper protein azurin and on small-tetraheme cytochrome (STC) with iron-containing heme cofactors (Fig. 22a) [35]. Strikingly, the measured conductance of the STC junction is by 3 orders of magnitude larger than the one detected for azurin although these two proteins have similar size and shape. Moreover, the experiments suggested coherent electron tunneling as an undergoing charge transfer mechanism in contrast to incoherent electron hopping, which is dominant in solvated multi-heme proteins.

Using the state-of-the-art computational procedures (Sec. 3.5), we computed the junction currects and confirmed the tunneling mechanism [36, 41]. The hole transfer proceed in the off-resonant regime, flowing through the protein over delocalized heme states and amino-acid side chains (see Fig. 22c). Presence of these aromatic states, which are relatively high in energy, explains the large difference in conductance of STC and azurin, where no organic cofactors are incorporated into the protein structure. Interestingly, the redox states of metal cations were not found important for the conductance, in contrast to hopping transfer in solutions.

By evaluation of the tunneling currents on STC junction models of different orientations of sizes, we showed that the current magnitudes decay exponentially, however, due

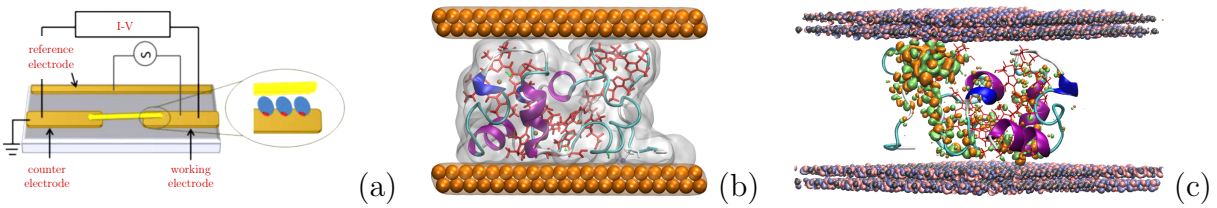

Figure 22: Small-tetraheme cytochrome (STC) junction between gold contacts: (a) experimental setup of the suspended nanowire method, (b) the junction model for DFT calculations of tunneling currents, (c) one of the dominant conduction channels in the off-resonant regime. The figures are taken from Ref. 35 and 36.

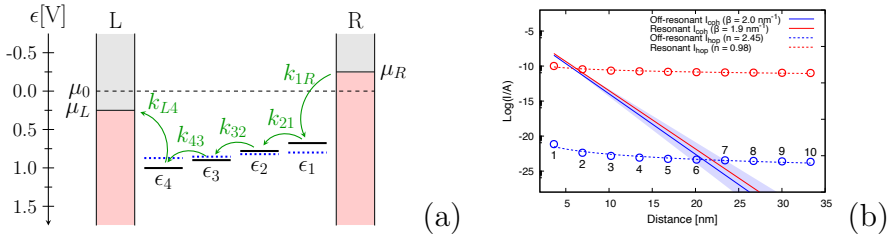

Figure 23: Electron transport through multi-heme cytochrome junctions between gold contacts: (a) schematic diagram of redox state positions in STC junction with indicated hopping transitions, (b) comparison of incoherent hopping and coherent tunneling current magnitudes and their distance dependence in the stacked STC junctions. The figures are taken from Ref. 41.

tot the large density of protein states, the decay factor has a small magnitude of 0.2 $Å^{-1}$, ensuring the tunneling over several nanometers. The hopping mechanism was shown to be uncompetitive due to the large potential decrease at the interface preventing efficient electron hole injection (c.f., Fig. 23a). However, we predicted a crossover of transport mechanism from coherent tunneling to incoherent hopping for multi-heme cytochromes at ∼7 nm (Fig. 23b), in near resonant regime, which could be accessible, for example, by electrochemical gating.

6 Other applications

6.1 Donor-acceptor ET reactions in solution

Electron transfer events between redox pairs in solutions are well described by outer-sphere Marcus theory (Sec. 2.1.1) and typically studied by molecular-dynamics techniques in QM/MM potentials (Sec. 3.4). However, in the conventional QM/MM description the reduced and oxidized species are simulated separately, neglecting their mutual interactions, and so limiting to dilute-limit regime [51, 356, 462] Therefore, we developed the so-called double-QM/MM method (Sec. 4.1), where both species are treated in the same simulation box and the distance dependencies of the free-energy surfaces can be directly studied [363].

First we explored the distance dependencies of electron transfer between hexaaqua $Ru^{2/3+}$ and $Fe^{2/3+}$ complexes in water solution (c.f. Fig. 7), where we relied on the linear response approximation (Eqs. (94) and (95)), which was well justified for the studied system. Recently, we focused on ferricyanide ($[Fe(CN)_6]^{4-}$) / ferrocyanide ($[Fe(CN)_6]^{3-}$) redox couple [354, 463–467], which often used in electrochemistry as a standard, thanks to the reversible electron transfer at low concentrations. We investigated the reliability of the linear response approximation for higher concentrations by reducing the interaction distance down to touching sphere limit.

The ferri/ferro-cyanide complexes have octahedral symmetry and their frontier HOMO, LUMO orbitals facilitating the electron transfer are dominated by the iron d orbitals (see Fig. 24a). Nevertheless, these molecular orbitals are partly delocalized to nitrogens in cyano groups that effectively increases the Marcus radii of these species. This effect, together with the stable and very similar configurations [468–471], is responsible for the relatively low reorganization free energies (1.47 eV, measured by photoemission spectroscopy [472]). We reproduced this value by using conventional QM/MM as well as dilute-limit double-QM/MM calculations (these results were not published yet).

To justify the linear response approximation, we applied the free-energy computational techniques with Warshel's energy-gap reaction coordinate [252] to obtained the reorganization free energy directly from the free energy surfaces (see Fig. 24b where both the free energies and the energy-gap distributions are shown). The linearity is well justified in the dilute limit (Fe-Fe separation 20 Å, error in free energy 0.01 eV) and well preserved down to the touching-sphere limit (7.5 Å, error 0.03 eV). Finally, we combined the double-QM/MM treatment with polarizable force fields to avoid Pekar-factor based reorganization free energy corrections for electronic polarizability, and evaluated the elec-

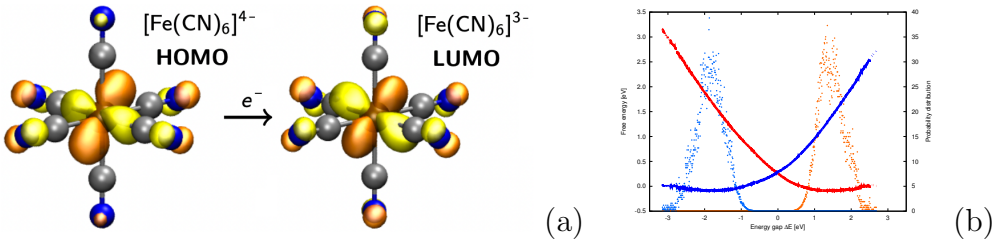

Figure 24: Ferricyanide / ferrocyanide redox pair: (a) frontier HOMO / LUMO orbitals facilitating the electron transfer, (b) free energy surfaces obtained by WHAM.

tronic coupling between the redox species by POD method. In this way, we were able to well reproduce the experimental rate constants from NMR measurements [473].

6.2 Intramolecular redox-state transitions

Resorcinarenes are cyclic macromolecules formed by cyclotetramerization of an aldehyde and resorcinol [474–476] that are used for chiral host-guest recognition and formation of supramolecular self-assembled structures [477–481]. These molecules are relatively flexible, substituents in their meso-positions can flip to different positions, and according to their relative orientations the resorcinarenes form four configuration types conventionally labeled as rctt, rccc, rcct, and rtct.

The complexity of resorcinarene dynamics and structural stability is further increased when the meso-substituent have redox character, i.e. they can be exist in either reduced or oxidized charge states. Often, hydroquinone and benzoquinone are incorporated in these molecules, which can undergo intramolecular charge transfer transitions detectable by characteristic changes in UV/VIS spectra. Simultaneously, the structural changes induced by the charge transfer, are recognizable by nuclear magnetic resonance (NMR) techniques.

We investigated such intramolecular charge transfer events on resorcinarenes bearing four 3,5-di-t-butyl-4-hydroxyphenyl (DtBHP) redox-active groups [476]. As the electron transfer events are in this case coupled with the proton transfer, the conformational changes can be controlled by pH of the solution via acidic concentrations. Due to the resorcinarene symmetries, five different optical patterns, distinguishable by color changes in visible light region, were observed. The whole system thus represent single-molecular redox-active photochemical switch that could be utilized as chemosensor.

The redox-active resorcinarenes can be also used for manufacturing molecular rotors. The rotation dynamics can be initiated/stopped by the oxidation/reduction, respectively, of the suitable meso-substituents, and further controlled by solvent polarity and temper-

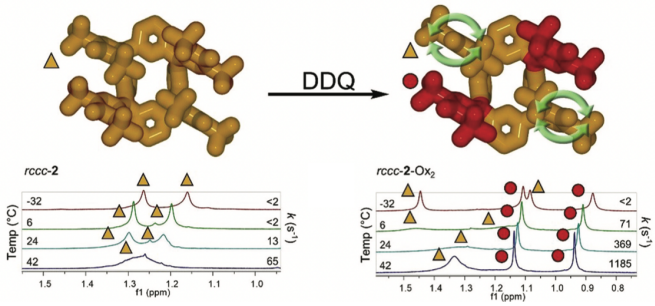

Figure 25: Comparison of relative rotation of the meso-substituents in resorcinarenes (left) and fuchsonarenes (right), and the corresponding high field (t-butyl) region of ^{1}H NMR spectra in acetone at different temperatures (DDQ: 2,3-dichloro-5,6-dicyano-1,4-benzoquinone). The figure is taken from Ref. 482.

ature. We demonstrated this behavior or DtBHP-substituted resorcinarenes and their transitions to fuchsonarenes (i.e. oxidized resorcinarenes with hemiquinonoid groups in diagonal arrangement, see Fig. 25) [482]. In all these cases, we supported the experimental works by series of classical molecular dynamics simulations and DFT calculations to suggest the best molecular design and interpret the UV/VIS and NMR measurements [483].

6.3 Charge transfer on aqueous semiconductor interfaces

While diamond is a well known insulator exhibiting large gap (∼5.5 eV) between valence and conduction bands, diamond surface terminated by hydrogen exhibit negative electron affinity and p-type conductivity [484–486]. This effect can be enhanced by boron doping and it can lead even to superconductive behavior when the diamond is heavily doped [487–489]. However, at low doping levels, the boron-doped diamond (BDD) exhibit the semiconductor properties.

BDD became popular material in electrochemistry thanks to its wide potential window (from -1.25 V to 2.3 V vs. SHE), low background currents, and large stability [490]. Nowadays, it is used, for example, for electrochemical wastewater treatment, water disinfection, pH detection, biosensoring, and electrochemical synthesis [491–493] However, the BDD electrode properties differ based on their surface termination. When the electrodes are prepared by chemical vapour deposition (CVP) technique, they are hydrophobic and mostly reversible, while after their oxidation, the BDD surfaces exhibit the opposite properties (compare CV curves in Fig. 26) [494, 495]. Besides the surface termination, the boron doping concentrations are known to affect the electrochemical response of BDD electrodes as well [496].

We employed density functional theory (DFT) to predict termination stability (phase

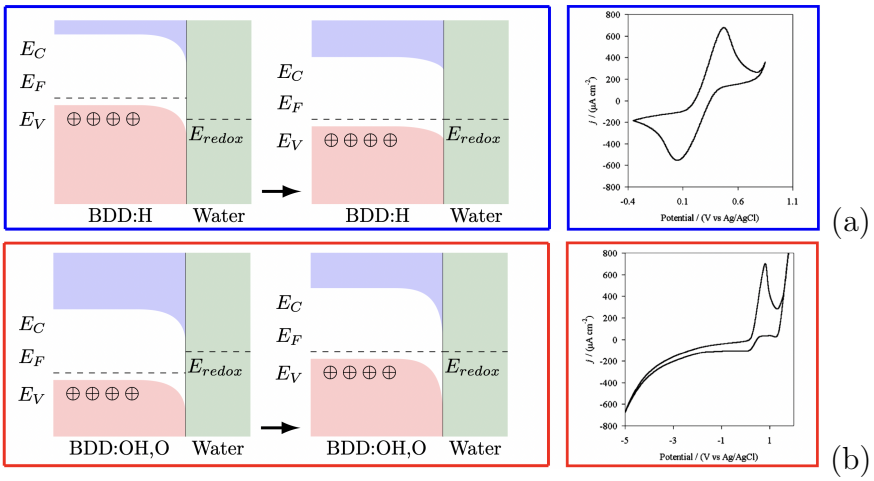

Figure 26: Electronic band alignment and electrochemical response on (a) reduced and (b) oxidized aqueous interfaces with boron-dopped diamond (BDD).

diagrams) of both diamond and BDD surfaces of (100) and (111) orientations [365]. The calculations showed that the as-grown electrode surfaces are terminated by atomic hydrogen, which is replaced by mixture of hydroxyl groups and carbonyl oxygens, when the electrodes are electrochemically oxidized. As these groups are forming relatively strong hydrogen bonds with the nearest hydration layers in solution, in contrast to hydrogen termination where these kinds of interactions are not preferred, the BDD oxidation leads to hydrophobic / hydrophilic character change.

On the other hand, explanation of the different electrochemical response of the reduced and oxidized BDD electrodes, requires analyses of the interface electronic states [365,497, 498]. The hydrogen termination forms the opposite surface dipole than the hydroxyl and oxygen species, which affects the electrode work functions. The reduced electrodes have the Fermi level higher than redox potential of ferricyanide / ferrocyanide couple, typically used to measure the CV curves. Interface electron transfer equilibrating these two level thus flatten the depletion layer in BDD, which leads to reversible current-voltage response like at metallic electrodes (see Fig. 26). The level alignment at the oxidized interfaces is opposite, the band bending over the depletion layer is enhanced, and, as a result, the electrochemical response is irreversible.

6.4 Catalytic charge transfer processes on metal-oxide surfaces

Metal oxides are popular as surface materials in electrochemistry for their catalytic activities related to large structural and electronic variability of such surfaces [109]. Transition metals such as iron, titanium, manganese, zirconium, cobalt, or nickel are often utilized

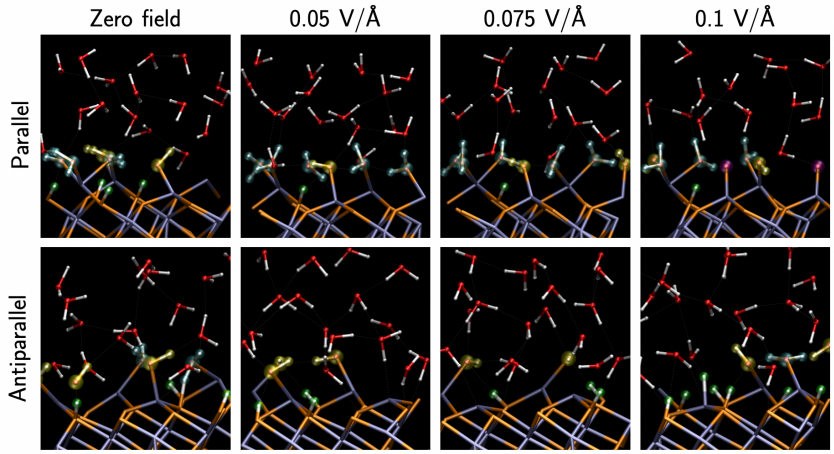

Figure 27: Snapshots from the non-equilibrium first-principles molecular dynamics of hematite / water interfaces under external static electric fields applied parallel or antiparallel with respect to the outward surface plane. The hematite slab's Fe atoms are shown in light blue and oxygen atoms in orange. Adsorbed non-dissociated water molecules are highlighted by cyan color, while dissociated hydrogen protons, hydroxyl groups, and oxygens adsorbed to the surface are depicted in green, yellow, and magenta, respectively. The figure is adapted from Ref. 401.

for biomolecular sensing [499], recently also in the form of nanoparticles, which have larger surface areas and richer electronic properties than traditional flat surfaces.

One of the most popular metal-oxide materials in electrochemistry is titania (TiO_2), which is famous for its photocatalytic activity, i.e. splitting of water at the electrode surface largely enhanced by illumination [500–502]. We investigated the structural water confinement at two titania polymorphs – rutile and anatase – by classical molecular dynamics simulations and studied the effects of applied static and time-varying electric field on dynamical properties of the interface water layers [377, 503]. In particular, we investigated response of the hydrogen-bond lifetimes, self-diffusivity, and vibrations.

Later, we employed reactive force field (ReaxFF [504, 505]) to investigate the spontaneous water splitting reactions catalysed by titania [506]. In contrast to the classical biomolecular force fields, ReaxFF allows to describe not only bond breaking/making but also charge transfer processes [507, 508], although the charge densities are also approximated by point charge distributions there. Therefore, changes in mean potentials and fields can be studied. For titania, we showed that there is a large potential drop and corresponding intrinsic field variation at the aqueous interfaces of both rutile and anatase [506]. These strong local fields enhance the surface water confinement and participate in catalytic O-H bond breakage by orienting the water molecules to reactive configurations.

Hematite (α-Fe_2O_3) is another photocatalytic material able to split water, which re-

cently became as popular as titania thanks to its relative ubiquity and low costs [509–512]. However, because of the anti-ferromagnetic layer composition and complex surface properties, computational studies of hematite interfaces are challenging and often require advanced simulation techniques [206, 513]. For example, it was shown by von Rudorff *et al.* [378, 514] that to capture the correct surface geometry, protonation, and related charge transfer phenomena in aqueous solution, the computationally very demanding first-principles simulations at hybrid functional level need to be applied.

We performed the non-equilibrium first-principles molecular dynamics to study the water splitting on aqueous hematite interfaces induced by external electric fields mimicing the electrochemical bias potential effects [401]. The fields were applied perpendicular to the surface, both in parallel and anti-parallel orientation with respect to the outward surface-plane normal, with increasing intensity up to 0.1 V/Å(see Fig. 27). The field-induced water dissociation was observed, followed by hopping-like proton transfer across the simulation cell, and development of Helmholtz layers compensating the induced surface charge. The performed calculations thus simulated simple electrochemical cell with the catalytic electrodes.

6.5 External-field induced charge transport

Ice VII is one of the 18 known ice polymorphs, which is form under high pressures (above 2 GPa). It has a cubic structure composed of two interpenetrating sublattices of water molecules mutually interacting by hydrogen bonding [515, 516]. Experimentally, methods like water confinement in nanomeniscus [517], and subnanosecond laser-induced shock waves can be used to prepare the ice VII phase [518]. Besides, the ordered high-pressure phases could be prepared by electrofreezeing techniques employing static electric fields [519, 520].

Due to the densely packed structure and high pressures, the bonds between oxygen and hydrogen atoms are weakened and the protons can relatively easily change their positions in the double-well potentials between neighbouring O...O pairs in the same sublattice. Consequently, when an external field is applied, the protons are dragged in the field direction, diffusing in the preserved lattice of oxygens. This state is known as a superionic (SI) ice phase and its existence was recently proved by Millot *et al.* by shock compression [411]. Although these phases might seem artificial at Earth, there is indirect evidence for its presence in Solar-system exoplanet "ice giants" Uranus and Neptune.

We performed a series of first-principles MD simulations [400, 402, 521] to investigate the O-H bonding in ice VII, its pressure dependence, dielectric properties, as well as

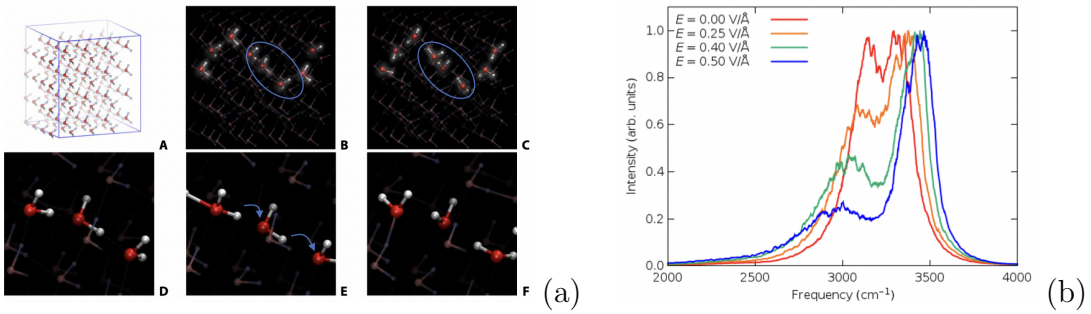

Figure 28: External-field induced proton hopping in ice VII: (a) snapshots from the non-equilibrium first-principles molecular dynamics, (b) field response of in the stretching band of the vibrational spectrum. The figures are taken from Ref. 400.

the field-induced dissociation. As the pressure increases from 5 to 20 GPa, the O...O distances shrink and the O-H bonds start to be more ionized, which is exhibited by the increased gap between the valence and conduction bands of ice VII [521]. These changes affect the stretching band of the vibrational Raman spectra, on which the transition to SI phase can be detected [522].

Finally, we applied the static electric fields of magnitudes between from 0.02 to 0.50 V/Å to induce the phase transition [400]. Indeed, when the dissociation threshold ∼0.3 V/Å was exceeded, the proton hopping between practically unperturbed positions of oxygen atoms was initiated. The protons were propagated though the ice VII crystal by Grotthus-like mechanism following the zig-zag pathways oriented along the field direction (see Fig. 28a). The simultaneous changes in the Raman spectra (Fig. 28b) were in this case significant and followed the trend observed in experimental measurements [522].

7 Conclusion

Transfer of charge can proceed in many different materials by various mechanisms, for examples, ionic diffusive transport in electrolytes, proton Grotthus-type transfer in water, incoherent electron hopping through biomolecular redox chains, coherent tunneling through molecular junctions, polaronic charge propagation in molecular crystals, band-like electron transport in metals, or quantum transport in superconductive metallic alloys. Here, we limited ourselves to electronic transfer in molecular systems, with a special focus on transport facilitated by biomolecules.

Incoherent electron hopping and coherent tunneling were briefly reviewed as limiting cases of the transport mechanisms that can be facilitated by biomolecules in their native environment, on electrochemical interfaces, or in nanobioelectronic devices. Then, the most popular computational approaches applicable in electronic charge-transfer studies were summarized, although many other techniques can be found in literature. Also, methods of potential energy evaluations (i.e. molecular mechanics, quantum-chemistry methods, density functional theory, etc.), inherently used in the discussed approaches, were not reviewed to not exceed the scope of the thesis.

The research activities of the author are introduced and discussed in the second half of the thesis. First, works on the methodology development related to biomolecular charge-transfer studies were listed. These include the design of double-QM/MM method for investigations of outer-sphere electron hopping, implementation of the POD method for electronic coupling element calculations, tuning and refining works on the GolP-CHARMM force fields for the biomolecular interfaces with gold surfaces, and improving performance of *ab initio* non-equilibrium molecular dynamics with external electric fields.

Finally, the main applications focused on electron transfer in various systems are introduced as successful study cases. Five selected applications involving biologically relevant systems are followed by another five applications on other systems. These selections illustrate the research activities of the author and its research group during last decade and their relevance is supported by the reprints of relevant articles from peer-reviewed journals, where this research was published.

Besides these research activities, the author participate in education of students at Faculty of Science at University of South Bohemia in České Budějovice. There, at Department of Physics, he established two new courses: "Density Functional Theory (DFT) and Its Applications" and "Charge Transfer Processes and Their Simulations". The latter course covers the theory and computational approaches summarized in this thesis, and the up-to-date scientific knowledge in this field is communicated to students.

References

[1] Moser, C. C.; Keske, J. M.; Warncke, K.; Farid, R. S.; and Dutton, P. L. Nature of Biological Electron Transfer. *Nature* **1992**, 355.

[2] Gray, H. B. and Winkler, J. R. Electron Transfer in Proteins. *Annu. Rev. Biochem.* **1996**, 65, 537–561.

[3] Jeuken, L. J. C.; Jones, A. K.; Chapman, S. K.; Cecchini, G.; and Armstrong, F. A. Electron-Transfer Mechanisms through Biological Redox Chains in Multicenter Enzymes. *J. Am. Chem. Soc.* **2002**, 124, 5702–5713.

[4] Page, C. C.; Moser, C. C.; and Dutton, P. L. Mechanism for Electron Transfer Within and Between Proteins. *Curr. Opin. Chem. Biol.* **2003**, 7, 551–556.

[5] Gray, H. B. and Winkler, J. R. Electron Tunneling through Proteins. *Quart. Rev. Biophys.* **2003**, 36(3), 341–372.

[6] Gray, H. B. and Winkler, J. R. Long-Range Electron Transfer. *Proc. Nat. Acad. Sci.* **2005**, 102, 3534–3539.

[7] Cordes, M. and Giese, B. Electron Transfer in Peptides and Proteins. *Chem. Soc. Rev.* **2009**, 38, 892–901.

[8] Gray, H. B. and Winkler, J. R. Electron Flow Through Metalloproteins. *Biochim. Biophys. Acta* **2010**, 1797, 1563–1572.

[9] Liu, L.-N.; Bryan, S. J.; Huang, F.; Yu, J.; Nixon, P. J.; Rich, P. R.; and Mullineaux, C. W. Control of Electron Transport Routes through Redox-Regulated Redistribution of Respiratory Complexes. *Proc. Nat. Acad. Sci.* **2012**, 109(28), 11431–11436.

[10] Williamson, H. R.; Dow, B. A.; and Davidson, V. L. Mechanism for Control of Biological Electron Transfer Reactions. *Bioorg. Chem.* **2014**, 57, 213–221.

[11] Blumberger, J. Recent Advances in the Theory and Molecular Simulation of Biological Electron Transfer Reactions. *Chem. Rev.* **2015**, 115, 11191–11238.

[12] Lienemann, M. Molecular Mechanism of Electron Transfer Employed by Native Proteins and Biological-Inorganic Hybrid Systems. *Comput. Struct. Biotech. J.* **2021**, 19, 206–213.

[13] Pirbadian, S. and El-Naggar, M. Y. Multistep Hopping and Extracellular Charge Transfer in Microbial Redox Chains. *Phys. Chem. Chem. Phys.* **2012**, 14, 13802–13808.

[14] Takematsu, K.; Pospisil, P.; Pizl, M.; Towrie, M.; Heyda, J.; Zalis, S.; Kaiser, J. T.; Winkler, J. R.; Gray, H. B.; and Vlcek, A. Hole Hopping Across a Protein-Protein Interface. *J. Phys. Chem. B* **2019**, 123, 1578–1591.

[15] Sorensen, M. L. H.; Sanders, B. C.; Hicks, L. P.; Rasmussen, M. H.; Vishart, A. L.; Kongsted, J.; Winkler, J. R.; Gray, H. B.; and Hansen, T. Hole Hopping through Cytochrome P450. *J. Phys. Chem. B* **2020**, 124, 3065–3073.

[16] Marcus, R. A. and Sutin, N. Electron Transfer in Chemistry and Biology. *Biochim. Biophys. Acta* **1985**, 811, 265–322.

[17] Winkler, J. R. and Gray, H. B. Elecron Flow through Metalloproteins. *Chem. Rev.* **2014**, 114, 3369–3380.

[18] Kokhan, O.; Ponomarenko, N. S.; Pokkuluri, P. R.; Schiffer, M.; Mulfort, K. L.; and Tiede, D. M. Bidirectional Photoinduced Electron Transfer in Ruthenium(II)-Tris-bipyridyl-Modified PpcA, a Multi-heme c-Type Cytochrome from Geobacter sulfurreducens. *J. Phys. Chem. B* **2015**, 119, 7612–7624.

[19] Blumberger, J. Electron Transfer and Transport through Multi-Heme Proteins: Recent Progress and Future Directions. *Curr. Opin. Chem. Biol.* **2018**, 47, 24–31.

[20] van Wonderen, J. H.; Hall, C. R.; Jiang, X.; Adamczyk, K.; Carof, A.; Heisler, I.; Piper, S. E. H.; Clarke, T. A.; Watmough, N. J.; Sazanovich, I. V.; Towrie, M.; Meech, S. R.; Blumberger, J.; and Butt, J. N. Ultrafast Light-Driven Electron Transfer in a Ru(II)tris(bipyridine)-Labeled Multiheme Cytochrome. *J. Am. Chem. Soc.* **2019**, 141, 15190–15200.

[21] van Wonderen, J.; Adamczyk, K.; Wu, X.; Jiang, X.; Piper, S. E. H.; Hall, C. R.; Edwards, M. J.; Clarke, T. A.; Zhang, H.; Jeuken, L. J. C.; Sazanovich, I. V.; Towrie, M.; Blumberger, J.; Meech, S. R.; and Butt, J. N. Nanosecond Heme-to-Heme Electron Transfer Rates in a Multiheme Cytochrome Nanowire Reported by a Spectrally Unique His/Met-Ligated Heme. *Proc. Nat. Acad. Sci.* **2021**, 118.

[22] Guo, L.-H. and Hill, H. A. Direct Electrochemistry of Proteins and Enzymes. *Adv. Inorg. Chem.* **1991**, 36, 341–375.

[23] Leger, C. and Bertrand, P. Direct Electrochemistry of Redox Enzymes as a Tool for Mechanistic Studies. *Chem. Rev.* **2008**, 108, 2379–2438.

[24] Shumyantseva, V. V.; Bulko, T. V.; Lisitsyna, V. B.; Urlacher, V. B.; Kuzikov, A. V.; Suprun, E. V.; and Archakov, A. I. Electrochemical Measurement of Intraprotein and Interprotein Electron Transfer. *Biophysics* **2013**, 58, 349–354.

[25] Armstrong, F. A.; Heering, H. A.; and Hirst, J. Reactions of Complex Metalloproteins Studied by Protein-Film Voltammetry. *Chem. Soc. Rev.* **1997**, 26, 169–179.

[26] Armstrong, F. A.; Belsey, N. A.; Cracknell, J. A.; Goldet, G.; Parkin, A.; Reisner, E.; Vincent, K. A.; and Wait, A. F. Dynamic Electrochemical Investigations of Hydrogen Oxidation and Production by Enzymes and Implications for Future Technology. *Chem. Soc. Rev.* **2009**, 38, 36–51.

[27] Kurth, J. M.; Dahl, C.; and Butt, J. N. Catalytic Protein Film Electrochemisty Provides a Direct Measure of the Tetrathionate/Thiosulfate Reduction Potential. *J. Am. Chem. Soc.* **2015**, 137, 13232–13235.

[28] del Barrio, M. and Fourmond, V. Redox (In)activations of Metalloenzymes: A Protein Film Voltammetry Approach. *ChemElectroChem* **2019**, 6, 4949–4962.

[29] Zhang, J.; Kuznetsov, A. M.; Medvedev, I. G.; Chi, Q.; Albrecht, T.; Jensen, P. S.; and Ulstrup, J. Single-Molecule Electron Transfer in Electrochemical Environments. *Chem. Rev.* **2008**, 108, 2737–2791.

[30] Artes, J. M.; Lopez-Martinez, M.; Giraudet, A.; Diez-Perez, I.; Sanz, F.; and Gorostiza, P. Current-Voltage Characteristics and Transition Voltage Spectroscopy of Individual Redox Proteins. *J. Am. Chem. Soc.* **2012**, 134, 20218–20221.

[31] Della Pia, E. A.; Elliott, M.; Jones, D. D.; and Macdonald, J. E. Orientation-Dependent Electron Transport in a Single Redox Protein. *ACS Nano* **2012**, 6, 355–361.

[32] Ruiz, M. P.; Aragones, A. C.; Camarero, N.; Vilhena, J. G.; Ortega, M.; Zotti, L. A.; Perez, R.; Cuevas, J. C.; Gorostiza, P.; and Diez-Perez, I. Bioengineering a Single-Protein Junction. *J. Am. Chem. Soc.* **2017**, 139, 15337–15346.

[33] Tang, L.; Yi, L.; Jiang, T.; Ren, R.; Nadappuram, B. P.; Zhang, B.; Wu, J.; Liu, X.; Lindsay, S.; Edel, J. B.; and Ivanov, A. P. Measuring Conductance Switching in Single Proteins Using Quantum Tunneling. *Sci. Adv.* **2022**, 8.

[34] Bian, K.; Gerber, C.; Heinrich, A. J.; Muller, D. J.; Scheuring, S.; and Jiang, Y. Scanning Probe Microscopy. *Nat. Rev. Methods Primers* **2021**, 1, 36.

[35] Garg, K.; Ghosh, M.; Eliash, T.; van Wonderen, J. H.; Butt, J. N.; Shi, L.; Jian, X.; Futera, Z.; Blumberger, J.; Pecht, I.; Sheves, M.; and Cahen, D. Direct Evidence for Heme-Assisted Solid-State Electronic Conduction in Multi-Heme c-Type Cytochromes. *Chem. Sci.* **2018**, 9, 7304–7310.

[36] Futera, Z.; Ide, I.; Kayser, B.; Garg, K.; Jiang, X.; van Wonderen, J. H.; Butt, J. N.; Ishii, H.; Pecht, I.; Sheves, M.; Cahen, D.; and Blumberger, J. Coherent Electron Transport across a 3 nm Bioelectronic Junction Made of Multi-Heme Proteins. *J. Phys. Chem. Lett.* **2020**, 11, 9766–9774.

[37] Andolfi, L.; Bizzarri, A. R.; and Cannistraro, S. Electron Tunneling in a Metal-Protein-Metal Junction Investigated by Scanning Tunneling and Conductive Atomic Force Spectroscopies. *Appl. Phys. Lett.* **2006**, 89, 183125.

[38] Kumar, K. S.; Pasula, R. R.; Lim, S.; and Nijhuis, C. A. Long-Range Tunneling Processes across Ferritin-Based Junctions. *Adv. Mater.* **2016**, 28, 1824–1830.

[39] Fereiro, J. A.; Yu, X.; Pecht, I.; Sheves, M.; Cuevas, J. C.; and Cahen, D. Tunneling Explains Efficient Electron Transport via Protein Junctions. *Proc. Nat. Acad. Sci.* **2018**, 115(20), 4577–4583.

[40] Cahen, D.; Pecht, I.; and Sheves, M. What Can We Learn from Protein-Based Electron Transport Junctions? *J. Phys. Chem. Lett.* **2021**, 12, 11598–11603.

[41] Futera, Z.; Wu, X.; and Blumberger, J. Tunneling-to-Hopping Transition in Multiheme Cytochrome Bioelectronic Junctions. *J. Phys. Chem. Lett.* **2023**, 14, 445–452.

[42] Lee, T.; Kim, S.; Kim, J.; Park, S.-C.; Yoon, J.; Park, C.; Sonn, H.; Ahn, J.-H.; and Min, J. Recent Advances in Biomolecule-Nanomaterial Heterolayer-Based Charge Storage Devices for Bioelectronic Applications. *Materials* **2020**, 13, 3520.

[43] Ha, T. Q.; Planje, I. J.; White, J. R. G.; Aragones, A. C.; and Diez-Perez, I. Charge Transport at the Protein-Electrode Interface in the Emerging Field of Biomolecular Electronics. *Curr. Opin. Electrochem.* **2021**, 28, 100734.

[44] Zhang, L.; Lu, J. R.; and Waigh, T. A. Electronics of Peptide- and Protein-Based Biomaterials. *Adv. Colloid Interface Sci.* **2021**, 287, 102319.

[45] Atkinson, J. T.; Chavez, M. S.; Niman, C. M.; and El-Naggar, M. Y. Living Electronics: A Catalogue of Engineered Living Electronic Components. *Microbial Biotech.* **2022**, pages 1–27.

[46] Marcus, R. A. On the Theory of Oxidation-Reduction Reactions Involving Electron Transfer I. *J. Chem. Phys.* **1956**, 24(5), 966–978.

[47] Marcus, R. A. Electrostatic Free Energy and Other Properties of States Having Nonequi-

librium Polarization. I. *J. Chem. Phys.* **1956**, 24(5), 979–989.

[48] Hush, N. S. Adiabatic Theory of Outer Sphere Electron Transfer Reactions in Solution. *Trans. Faraday Soc.* **1961**, 57, 557–580.

[49] Hush, N. S. Homogeneous and Heterogeneous Optical and Thermal Electron Transfer. *Electrochim. Acta* **1968**, 13, 1005–1023.

[50] Marcus, R. A. Exchange Reactions and Electron Transfer Reactions Including Isotopic Exchange - Theory of Oxidation-Reduction Reactions Involving Electron Transfer. *Discuss. Faraday Soc.* **1960**, 29, 21–31.

[51] Blumberger, J. and Lamoureux, G. Reorganization Free Energies and Quantum Corrections for a Model Electron Self-Exchange Reaction: Comparison of Polarizable and Non-Polarizable Solvent Models. *Mol. Phys.* **2008**, 106(12), 1597–1611.

[52] Marcus, R. A. Electron Transfer Reactions in Chemistry. Theory and Experiment. *Rev. Mod. Phys.* **1993**, 65(3), 599–610.

[53] Miller, J. R.; Calcaterra, L. T.; and Closs, G. L. Intramolecular Long-Distance Electron Transfer in Radical Anions. The Effects of Free Energy and Solvent on the Reaction Rates. *J. Am. Chem. Soc.* **1984**, 106, 3047–3049.

[54] Newton, M. D. and Sutin, N. Elecron Transfer Reactions in Condensed Phases. *Ann. Rev. Phys. Chem.* **1984**, 35, 437–480.

[55] Newton, M. D. Quantum Chemical Probes of Electron-Transfer Kinetics: The Nature of Donor-Acceptor Interactions. *Chem. Rev.* **1991**, 91, 767–792.

[56] Bixon, M. and Jortner, J. Electron Transfer - From Isolated Molecules to Biomolecules. *Adv. Chem. Phys.* **2007**, 106, 35–202.

[57] Newton, M. D. Control of Electron Transfer Kinetics: Models for Medium Reorganization and Donor-Acceptor Coupling. *Adv. Chem. Phys.* **2007**, 106, 303–375.

[58] Page, C. C.; Moser, C. C.; Chen, X.; and Dutton, L. Natural Engineering Principles of Electron Tunnelling in Biological Oxidation-Reduction. *Nature* **1999**, 402, 47–52.

[59] Beratan, D. D.; Skourtis, S. S.; Balabin, I. A.; Balaeff, A.; Keinan, S.; Venkatramani, R.; and Xiao, D. Steering Electrons on Moving Pathways. *Acc. Chem. Res.* **2009**, 42(10), 1669–1678.

[60] Skourtis, S. S.; Waldeck, D. H.; and Beratan, D. N. Fluctuations in Biological and Bioinspired Electron-Transfer Reactions. *Ann. Rev. Phys. Chem.* **2010**, 61, 461–485.

[61] Venkatramani, R.; Keinan, S.; Balaeff, A.; and Beratan, D. N. Nucleic Acid Charge Transfer: Black, White and Gray. *Coord. Chem. Rev.* **2011**, 255, 635–648.

[62] Saen-Oon, S.; Lucas, M. F.; and Guallar, V. Electron Transfer in Proteins: Theory, Applications and Future Perspectives. *Phys. Chem. Chem. Phys.* **2013**, 15, 15271–15285.

[63] Kubar, T. and Elstner, M. A Hybrid Approach to Simulation of Electron Transfer in Complex Molecular Systems. *Interface* **2013**, 10, 415.

[64] Matyushov, D. V. Protein Electron Transfer: Dynamics and Statistics. *J. Chem. Phys.* **2013**, 139, 25102.

[65] Beratan, D. N.; Liu, C.; Migliore, A.; Polizzi, N. F.; Skourtis, S. S.; Zhang, P.; and Zhang, Y. Charge Transfer in Dynamical Biosystems, or the Treachery of (Static) Images. *Acc.*

Chem. Res. **2015**, 48(2), 474–481.

[66] Narth, C.; Gillet, N.; Gailiez, F.; Levy, B.; and de la Lande, A. Electron Transfer, Decoherence, and Protein Dynamics: Insights from Atomistic Simulations. *Acc. Chem. Res.* **2015**, 48(4), 1090–1097.

[67] de la Lande, A.; Gillet, N.; Chen, S.; and Salahub, D. R. Progress and Challenges in Simulating and Understanding Electron Transfer in Proteins. *Arch. Biochem. Biophys.* **2015**, 582, 28–41.

[68] Jiang, X.; Futera, Z.; Ali, M. E.; Gajdos, F.; von Rudorff, G. F.; Carof, A.; Breuer, M.; and Blumberger, J. Cysteine Linkages Accelerate Electron Flow through Tetra-Heme Protein STC. *J. Am. Chem. Soc.* **2017**, 139, 17237–17240.

[69] El-Naggar, M. Y.; Wanger, G.; Leung, K. M.; Yuzvinsky, T. D.; Southam, G.; Yang, J.; Lau, W. M.; Nealson, K. H.; and Gorby, Y. A. Electrical Transport along Bacterial Nanowires from Shewanella oneidensis MR-1. *Proc. Nat. Acad. Sci.* **2010**, 107(42), 18127–18131.

[70] Breuer, M.; Rosso, K. M.; Blumberger, J.; and Butt, J. N. Multi-Haem Cytochromes in Shewanella Oneidensis MR-1: Structures, Functions and Opportunities. *Interface* **2014**, 12, 1117.

[71] Chong, G. W.; Karbelkar, A. A.; and El-Naggar, M. Y. Nature's Conductors: What Can Microbial Multi-Heme Cytochromes Teach Us About Electron Transport and Biological Energy Conversion? *Curr. Opin. Chem. Biol.* **2018**, 47, 7–17.

[72] Jiang, X.; Burger, B.; Gajdos, F.; Bortolotti, C.; Futera, Z.; Breuer, M.; and Blumberger, J. Kinetics of Trifurcated Electron Frlow in the Decaheme Bacterial Proteins MtrC and MtrF. *Proc. Nat. Acad. Sci.* **2019**, 116(9), 3425–3430.

[73] Yates, M. D.; Golden, J. P.; Roy, J.; Strycharz-Glaven, S. M.; Tsoi, S.; Erickson, J. S.; El-Naggar, M. Y.; Barton, S. C.; and Tender, L. M. Thermally Activated Long Range Electron Transport in Living Biofilms. *Phys. Chem. Chem. Phys.* **2015**, 17, 32564–32570.

[74] Yates, M. D.; Eddie, B. J.; Kotloski, N. J.; Lebedev, N.; Malanoski, A. P.; Lin, B.; Strycharz-Glaven, S. M.; and Tender, L. M. Toward Understanding Long-Distance Extracellular Electron Transport in an Electroautotrophic Microbial Community. *Energy Environ. Sci.* **2016**, 9, 3544–3558.

[75] Rosso, K. M. and Dupuis, M. Reorganization Energy Associated with Small Polaron Mobility in Iron Oxide. *J. Chem. Phys.* **2004**, 120, 7050–7054.

[76] Coropceanu, V.; Cornil, J.; da Silva Filho, D. A.; Olivier, Y.; Silbey, R.; and Bredas, J.-L. Charge Transport in Organic Semiconductors. *Chem. Rev.* **2007**, 107, 926–952.

[77] Nelson, J.; Kwiatkowski, J. J.; Kirkpatrick, J.; and Frost, J. M. Modeling Charge Transport in Organic Photovoltaic Materials. *Acc. Chem. Res.* **2009**, 42(11), 1768–1778.

[78] McKenna, K. P. and Blumberger, J. Crossover from Incoherent to Coherent Electron Tunneling Between Defects in MgO. *Phys. Rev. B* **2012**, 86, 245110.

[79] Blumberger, J. and McKenna, K. P. Constrained Density Functional Theory Applied to Electron Tunneling Between Defects in MgO. *Phys. Chem. Chem. Phys.* **2013**, 15, 2184–2196.

[80] Alexandrov, V. and Rosso, K. M. Electron Transport in Pure and Substituted Iron

Oxyhydroxides by Small-Polaron Migration. *J. Chem. Phys.* **2014**, 140, 234701.

[81] Oberhofer, H.; Reuter, K.; and Blumberger, J. Charge Transport in Molecular Materials: An Assessment of Computational Methods. *Chem. Rev.* **2017**, 117, 10319–10357.

[82] Giannini, S.; Carof, A.; and Blumberger, J. Crossover from Hopping to Band-Like Charge Transport in an Organic Semiconductor Model: Atomistic Nonadiabatic Molecular Dynamics Simulation. *J. Phys. Chem. Lett.* **2018**, 9, 3116–3123.

[83] Jiang, Y.; Geng, H.; Li, W.; and Shuai, Z. Understanding Carrier Transport in Organic Semiconductors: Computation of Charge Mobility Considering Quantum Nuclear Tunneling and Delocalization Effects. *J. Chem. Theory Comput.* **2019**, 15, 1477–1491.

[84] Giannini, S. and Blumberger, J. Charge Transport in Organic Semiconductors: The Perspective from Nonadiabatic Molecular Dynamics. *Acc. Chem. Res.* **2022**.

[85] Marcus, R. A. On the Theory of Electron-Transfer Reactions. VI. Unified Treatment for Homogeneous and Electrode Reactions. *J. Chem. Phys.* **1965**, 43(2), 679–701.

[86] Chidsey, C. E. D. Free Energy and Temperature Dependence of Electron Transfer at the Metal-electrolyte Interface. *Science* **1991**, 251(4996), 919–922.

[87] Futera, Z. and Blumberger, J. Electronic Couplings for Charge Transfer across Molecule/Metal and Molecule/Semiconductor Interfaces: Performance of the Projector Operator-Based Diabatization Approach. *J. Phys. Chem. C* **2017**, 121, 19677–19689.

[88] Matyushov, D. V. Electrode Redox Reactions with Polarizable Molecules. *J. Chem. Phys.* **2018**, 148, 154501.

[89] Blumberger, J. Cu^{+}_{aq} / Cu^{2+}_{aq} Redox Reaction Exhibits Strong Nonlinear Solvent Response Due to Change in Coordination Number. *J. Am. Chem. Soc.* **2008**, 130, 16065–16068.

[90] LeBard, D. N. and Matyushov, D. V. Protein-Water Electrostatics and Principles of Bioenergetics. *Phys. Chem. Chem. Phys.* **2010**, 12, 15335–15348.

[91] Vuilleumier, R.; Tay, K. A.; Jeanmairet, G.; Borgis, D.; and Boutin, A. Extension of Marcus Picture for Electron Transfer Reactions with Large Solvation Changes. *J. Am. Chem. Soc.* **2012**, 134, 2067–2074.

[92] Amadei, A.; Daidone, I.; and Bortolotti, C. A. A General Statistical Mechanical Approach for Modeling Redox Thermodynamics: The Reaction and Reorganization Free Energies. *RSC Adv.* **2013**, 3, 19657–19665.

[93] Daidone, I.; Amadei, A.; Zaccanti, F.; Borsari, M.; and Bortolotti, C. A. How the Reorganization Free Energy Affects the Reduction Potential of Structurally Homologous Cytochromes. *J. Phys. Chem. Lett.* **2014**, 5, 1534–1540.

[94] Sumi, H. and Marcus, R. A. Dynamical Effects in Electron Transfer Reactions. *J. Chem. Phys.* **1986**, 84, 4894–4914.

[95] Small, D. W.; Matyushov, D. V.; and Voth, G. A. The Theory of Electron Transfer Reactions: What May Be Missing? *J. Am. Chem. Soc.* **2003**, 125, 7470–7478.

[96] Blumberger, J.; Tavernelli, I.; Klein, M. L.; and Sprik, M. Diabatic Free Energy Curves and Coordination Fluctuations for the Aqueous Ag+/Ag2+ Redox Couple: A Biased Born-Oppenheimer Molecular Dynamics Investigation. *J. Chem. Phys.* **2006**, 124, 64507.

[97] LeBard, D. N.; Kapko, V.; and Matyushov, D. V. Energetics and Kinetics of Primary

Charge Separation in Bacterial Photosynthesis. *J. Phys. Chem. B* **2008**, 112, 10322–10342.

[98] LeBard, D. N. and Matyushov, D. V. Energetics of Bacterial Photosynthesis. *J. Phys. Chem. B* **2009**, 113, 12424–12437.

[99] Matyushov, D. V. Protein Electron Transfer: Is Biology (Thermo)Dynamic? *J. Phys.: Condens. Matter* **2015**, 27, 473001.

[100] Kontkanen, O. V.; Biriukov, D.; and Futera, Z. Reorganization Free Energy of Copper Proteins in Solution, in Vacuum, and on Metal Surfaces. *J. Chem. Phys.* **2022**, 156, 175101.

[101] Sarhangi, S. M. and Matyushov, D. V. Theory of Protein Charge Transfer: Electron Transfer between Tryptophan Residue and Active Site of Azurin. *J. Phys. Chem. B* **2022**.

[102] Nitzan, A. *Chemical Dynamics in Condensed Phases: Relaxation, Transfer, and Relations in Condensed Molecular Systems.* Oxford University Press, **2014**.

[103] Polizzi, N. F.; Skourtis, S. S.; and Beratan, D. N. Physical Constraints on Charge Transport through Bacterial Nanowires. *Faraday Discuss.* **2012**, 155, 43–62.

[104] Henstridge, M. C.; Laborda, E.; Rees, N. V.; and Compton, R. G. Marcus-Hush-Chidsey Theory of Electron Tranfer Applied to Voltammetry: A Review. *Electrochim. Acta* **2012**, 84, 12–20.

[105] Zhang, J.; Chi, Q.; Hansen, A. G.; Jensen, P. S.; Salvatore, P.; and Ulstrup, J. Interfacial Electrochemical Electron Transfer in Biology - Towards the Level of the Single Molecule. *FEBS Lett.* **2012**, 586, 526–535.

[106] Nazmutdinov, R. R.; Zinkicheva, T. T.; Shermukhamedov, S. A.; Zhang, J.; and Ulstrup, J. Electrochemistry of Single Molecules and Biomolecules, Molecular Scale Nanostructures, and Low-Dimensional Systems. *Curr. Opin. Electrochem.* **2018**, 7, 179–187.

[107] Matyushov, D. V. Electrochemistry of Protein Electron Transfer. *J. Electrochem. Soc.* **2022**, 169, 67501.

[108] Santos, E. and Schmickler, W. Models of Electron Transfer at Different Electrode Materials. *Chem. Rev.* **2022**.

[109] Bard, A. J. and Faulkner, L. R. *Electrochemical Methods: Fundamentals and Applications.* Wiley, 2nd edition, **2000**.

[110] Hughes, Z. E. and Walsh, T. R. Structure of the Electronical Double Layer at Aqueous Gold and Silver Interfaces for Saline Solutions. *J. Coll. Interface. Sci.* **2014**, 436, 99–110.

[111] Li, L.; Liu, Y.-P.; Le, J.-B.; and Cheng, J. Unraveling Molecular Structures and Ion Effects of Electric Double Layers at Metal Water Interfaces. *Cell Rep. Phys. Sci.* **2022**, 3, 100759.

[112] Neumann, E. Chemical Electric Field Effects in Biological Macromolecules. *Prog. Biophys. Mol. Biol.* **1986**, 47, 197–231.

[113] Shaik, S.; de Visser, S. P.; and Kumar, D. External Electric Field Will Control the Selectivity of Enzymatic-Like Bond Activations. *J. Am. Chem. Soc.* **2004**, 126, 11746–11749.

[114] Montenegro, A.; Dutta, C.; Mammetkuliev, M.; Shi, H.; Hou, B.; Bhattacharyya, D.; Zhao, B.; Cronin, S. B.; and Benderskii, A. V. Asymmetric Response of Interfacial Water to Applied Electric Fields. *Nature* **2021**, 594, 62–65.

[115] Neaton, J. B.; Hybertsen, M. S.; and Louie, S. G. Renormalization of Molecular Electronic Levels at Metal-Molecule Interfaces. *Phys. Rev. Lett.* **2006**, 97, 216405.

[116] Flores, F.; Ortega, J.; and Vazquez, H. Modelling Energy Level Alignment at Organic Interfaces and Density Functional Theory. *Phys. Chem. Chem. Phys.* **2009**, 11, 8658–8675.

[117] Biller, A.; Tamblyn, I.; Neaton, J. B.; and Kronik, L. Electronic Level Alignment at a Metal-Molecule Interface from a Short-Range Hybrid Functional. *J. Chem. Phys.* **2011**, 135, 164706.

[118] Tamblyn, I.; Darancet, P.; Quek, S. Y.; Bonev, S. A.; and Neaton, J. B. Electronic Energy Level Alignment at Metal-Molecule Interfaces with a GW Approach. *Phys. Rev. B* **2011**, 84, 201402.

[119] Souza, A. M.; Rungger, I.; Pemmaraju, C. D.; Schwingenschloegl, U.; and Sanvito, S. Constrained-DFT Method for Accurate Energy-Level Alignment of Metal/Molecule Interfaces. *Phys. Rev. B* **2013**, 88, 165112.

[120] Kharche, N.; Muckerman, J. T.; and Hybertsen, M. S. First-Principles Approach to Calculating Energy Level Alignment at Aqueous Semiconductor Interfaces. *Phys. Rev. Lett.* **2014**, 113, 176802.

[121] Egger, D. A.; Liu, Z.-F.; Neaton, J. B.; and Kronik, L. Reliable Energy Level Alignment at Physisorbed Molecule-Metal Interfaces from Density Functional Theory. *Nano Lett.* **2015**, 15, 2448–2455.

[122] Ma, J.; Liu, Z. F.; Neaton, J. B.; and Wang, L.-W. The Energy Level Alignment at Metal-Molecule Interfaces Using Wannier-Koopmans Method. *Appl. Phys. Lett.* **2016**, 108, 262104.

[123] Chen, Y.; Tamblyn, I.; and Quek, S. Y. Energy Level Alignment at Hybridized Organic-Metal Interfaces: The Role of Many-Electron Effects. *J. Phys. Chem. C* **2017**, 121, 13125–13134.

[124] Liu, Z.-F.; da Jornada, F. H.; Louie, S. G.; and NNeaton, J. B. Accelerating GW-Based Energy Level Alignment Calculations for Molecule-Metal Interfaces Using a Substrate Screening Approach. *J. Chem. Theory Comput.* **2019**, 15, 4218–4227.

[125] Umari, P. and Pasquarello, A. Ab Initio Molecular Dynamics in a Finite Homogeneous Electric Field. *Phys. Rev. Lett.* **2002**, 89(15), 157602.

[126] English, N. J. and Waldron, C. J. Perspectives on External Electric Fields in Molecular Simulation: Progress, Prospects and Challenges. *Phys. Chem. Chem. Phys.* **2015**, 17, 12407–12440.

[127] Mulheran, P. A.; Connell, D. J.; and Kubiak-Ossowska, K. Steering Protein Adsorption at Charged Surfaces: Electric Fields and Ionic Screening. *RSC Adv.* **2016**, 6, 73709–73716.

[128] Cassone, G.; Sponer, J.; and Saija, F. Ab Initio Molecular Dynamics Studies of the Electric-Field-Induced Catalytic Effects on Liquids. *Top. Catal.* **2021**.

[129] Otani, M. and Sugino, O. First-Principles Calculations of Charged Surfaces and Interfaces:

A Plane-Wave Nonrepeateed Slab Approach. *Phys. Rev. B* **2006**, 73, 115407.

[130] Sugino, O.; Hamada, I.; Otani, M.; Morikawa, Y.; Ikeshoji, T.; and Okamoto, Y. First-Priciples Molecular Dynamics Simulation of Biased Eletrode/Solution Interface. *Surf. Sci.* **2007**, 601, 5237–5240.

[131] Jinnouchi, R. and Anderson, A. B. Electronic Structure Calculations of Liquid-Solid Interfaces: Combination of Density Functional Theory and Modified Poisson-Boltzmann Theory. *Phys. Rev. B* **2008**, 77, 245417.

[132] Bonnet, N.; Morishita, T.; Sugino, O.; and Otani, M. First-Principles Molecular Dynamics at a Constant Electrode Potential. *Phys. Rev. Lett.* **2012**, 109, 266101.

[133] Benedikt, U.; Schneider, W. B.; and Auer, A. A. Modelling Electrified Interfaces in Quantum Chemistry: Constant Charge vs. Constant Potential. *Phys. Chem. Chem. Phys.* **2013**, 15, 2712–2724.

[134] Hamada, I.; Sugino, O.; Bonnet, N.; and Otani, M. Improved Modeling of Electrified Interfaces Using the Effective Screening Medium Method. *Phys. Rev. B* **2013**, 88, 155427.

[135] Haruyama, J.; Ikeshoji, T.; and Otani, M. Electrode Potential from Density Functional Theory Calculations Combined with Implicit Solvation Theory. *Phys. Rev. Mater.* **2018**, 2, 95801.

[136] Datta, S. *Quantum Transport: Atom to Transistor*. Cambridge University Press, **2013**.

[137] Ryndyk, D. A. *Theory of Quantum Transport at Nanoscale: An Introduction*. Springer, **2016**.

[138] Cuevas, J. C. and Scheer, E. *Molecular Electronics: An Introduction to Theory and Experiment*. World Scientific, 2nd edition, **2017**.

[139] Buttiker, M. Coherent and Sequential Tunneling in Series Barriers. *IBM J. Res. Dev.* **1988**, 32, 63–75.

[140] Meir, Y. and Wingreen, N. S. Landauer Formula for the Current through an Interacting Electron Region. *Phys. Rev. Lett.* **1992**, 68(16), 2512–2515.

[141] Lambert, C. J. Basic Concepts of Quantum Interference and Elecgron Transport in Single-Molecule Electronics. *Chem. Soc. Rev.* **2015**, 44, 875–888.

[142] Carey, R.; Chen, L.; Gu, B.; and Franco, I. When Can Time-Dependent Currents Be Reproduced by the Landauer Steady-State Approximation? *J. Chem. Phys.* **2017**, 146, 174101.

[143] Zwierzycki, M.; Khomyakov, P. A.; Starikov, A. A.; Xia, K.; Talanana, M.; Xu, P. X.; Karpan, V. M.; Marushchenko, I.; Turek, I.; Bauer, G. E. W.; Brocks, G.; and Kelly, P. J. Calculating Scattering Matrices by Wavefunction Matching. *Phys. Stat. Sol. (b)* **2008**, 245, 628–640.

[144] Buttiker, M.; Imry, Y.; Landauer, R.; and Pinhas, S. Generalized Many-Channel Conductance Formula with Application to Small Rings. *Phys. Rev. B* **1985**, 31(10), 6207–6215.

[145] Emberly, E. G. and Kirczenow, G. Theoretical Study of Electrical Conduction through a Molecule Connected to Metallic Nanocontacts. *Phys. Rev. B* **1998**, 58(16), 10911–10920.

[146] Agrait, N.; Yeyati, A. L.; and van Ruitenbeek, J. M. Quantum Properties of Atomic-Sized Conductors. *Phys. Rep.* **2003**, 377, 81–279.

[147] Mujica, V.; Nitzan, A.; Datta, S.; Ratner, M. A.; and Kubiak, C. P. Molecular Wire Junctions: Tuning the Conductance. *J. Phys. Chem. B* **2003**, 107, 91–95.

[148] Franco, I.; George, C. B.; Solomon, G. C.; Schatz, G. C.; and Ratner, M. A. Mechanically Activated Molecular Switch through Single-Molecule Pulling. *J. Am. Chem. Soc.* **2011**, 133, 2242–2249.

[149] Franco, I.; Solomon, G. C.; Schatz, G. C.; and Ratner, M. A. Tunneling Currents That Increase with Molecular Elongation. *J. Am. Chem. Soc.* **2011**, 133, 15714–15720.

[150] Papp, E.; Jelenfi, D. P.; Veszeli, M. T.; and Vattay, G. A Landauer Formula for Bioelectronic Applications. *Biomol.* **2019**, 9, 599.

[151] Lippmann, B. A. and Schwinger, J. Variational Principles for Scattering Processes. I. *Phys. Rev.* **1950**, 79(3), 469–480.

[152] Fisher, D. S. and Lee, P. A. Relation between Conductivity and Transmission Matrix. *Phys. Rev. B* **1981**, 23(12), 6851–6854.

[153] Lopez Sancho, M. P.; Lopez Sancho, J. M.; and Rubio, J. Quick Iterative Scheme for the Calculation of Transfer Matrices: Application to Mo(100). *J. Phys. F: Met. Phys.* **1984**, 14, 1205–1215.

[154] Todorov, T. N.; Briggs, G. A. D.; and Sutton, A. P. Elastic Quantum Transport through Small Structures. *J. Phys.: Condens. Matter* **1993**, 5, 2389–2406.

[155] Keldysh, L. V. Diagram Technique for Nonequilibrium Processes. *Sov. Phys. JETP* **1965**, 20(4), 1018–1026.

[156] Caroli, C.; Combescot, R.; Nozieres, P.; and Saint-James, D. Direct Calculation of the Tunneling Current. *J. Phys. C: Solid State Phys.* **1971**, 4, 916–929.

[157] Caroli, C.; Combescot, R.; Lederer, D.; Nozieres, P.; and Saint-James, D. A Direct Calculation of the Tunnelling Current II. Free Electron Description. *J. Phys. C: Solid State Phys.* **1971**, 4, 2598–2610.

[158] Taylor, J.; Guo, H.; and Wang, J. Ab Initio Modeling of Quantum Transport Properties of Molecular Electrronic Devices. *Phys. Rev. B* **2001**, 63, 245407.

[159] Xue, Y.; Datta, S.; and Ratner, M. A. First-Principles Based Matrix Green's Function Approach to Molecular Electronic Devices: General Formalism. *Chem. Phys.* **2002**, 281, 151–170.

[160] Brandbyge, M.; Mozos, J.-L.; Ordejon, P.; Taylor, J.; and Stokbro, K. Density-Functional Method for Nonequilibrium Electron Transport. *Phys. Rev. B* **2002**, 65, 165401.

[161] Spicka, V.; Velicky, B.; and Kalvova, A. Long and Short Time Quantum Dynamics: I. Between Green's Functions and Transport Equations. *Phys. E* **2005**, 29, 154–174.

[162] Rocha, A. R.; Garcia-Suarez, V. M.; Bailey, S.; Lambert, C.; Ferrer, J.; and Sanvito, S. Spin and Molecular Electronics in Atomically Generated Orbital Landscapes. *Phys. Rev. B* **2006**, 73, 85414.

[163] Paulsson, M. and Brandbyge, M. Transmission Eigenchannels from Nonequilibrium Green's Function. *Phys. Rev. B* **2007**, 76, 115117.

[164] Novaes, F. D.; da Silva, A. J. R.; and Fazzio, A. Density Functional Theory Method for Non-Equilibrium Charge Transport Calculations: TRANSAMPA. *Braz. J. Phys.* **2006**,

36, 799–807.

[165] Ozaki, T.; Nishio, K.; and Kino, H. Efficient Implementation of the Nonequilibrium Green Function Method for Electronic Transport Calculations. *Phys. Rev. B* **2010**, 81, 35116.

[166] Papior, N.; Lorente, N.; Frederiksen, T.; Garcia, A.; and Brandbyge, M. Improvements on Non-Equilibrium and Transport Green Function Techniques: The Next-Generation Transiesta. *Comp. Phys. Comm.* **2017**, 212, 8–24.

[167] Takaki, H.; Kobayashi, N.; and Hirose, K. SAKE: First-Principles Electron Transport Calculation Code. *J. Phys.: Condens. Matter* **2020**, 32, 325901.

[168] Butler, W. H.; Zhang, X.-G.; Nicholson, D. M. C.; and MacLaren, J. M. First-Principles Calculations of Electrical Conductivity and Giant Magnetoresistance of Co—Cu—Co Spin Valves. *Phys. Rev. B* **1995**, 52, 13399–13410.

[169] Sanvito, S.; Lambert, C. J.; Jefferson, J. H.; and Bratkovsky, A. M. General Green's-function Formalism for Transport Calculations with s p d Hamiltonians and Giant Magnetoresistance in Co- and Ni-based Magnetic Multilayers. *Phys. Rev. B* **1999**, 59(18), 11936–11948.

[170] Cook, B. G.; Dignard, P.; and Varga, K. Calculation of Electron Transport in Multiterminal Systems Using Complex Absorbing Potentials. *Phys. Rev. B* **2011**, 83, 205105.

[171] Cohen, G. and Galperin, M. Green's Function Methods for Single Molecule Junctions. *J. Chem. Phys.* **2020**, 152, 90901.

[172] Nitzan, A. A Relationship between Electron-Transfer Rates and Molecular Conduction. *J. Phys. Chem. A* **2001**, 105, 2677–2679.

[173] Davis, J. J.; Morgan, D. A.; Wrathmell, C. L.; Axford, D. N.; Zhao, J.; and Wang, N. Molecular Bioelectronics. *J. Mater. Chem.* **2005**, 15, 2160–2174.

[174] Weiss, E. A.; Wasielewski, M. R.; and Ratner, M. A. Molecules as Wires: Molecule-Assisted Movement of Charge and Energy. *Top. Curr. Chem.* **2005**, 257, 103–133.

[175] Visoly-Fisher, I.; Daie, K.; Terazono, Y.; Herrero, C.; Fungo, F.; Otero, L.; Durantini, E.; Silber, J. J.; Sereno, L.; Gust, D.; Moore, T. A.; Moore, A. L.; and Lindsay, S. M. Conductance of a Biomolecular Wire. *Proc. Nat. Acad. Sci.* **2006**, 103(23), 8686–8690.

[176] Lindsay, S. M. and Ratner, M. A. Molecular Transport Junctions: Clearing Mists. *Adv. Mater.* **2007**, 19, 23–31.

[177] Lu, Q.; Liu, K.; Zhang, H.; Du, Z.; Wang, X.; and Wang, F. From Tunneling to Hopping: A Comprehensive Investigation of Charge Transport Mechanism in Molecular Junctions Based on Oligo(p-phenylene ethynylene)s. *ACS Nano* **2009**, 3(12), 3861–3868.

[178] Liu, H.; Zhao, Z.; Wang, N.; and Zhao, J. Can the Transition from Tunneling to Hopping in Molecular Junctions Be Predicted by Theoretical Calculations? *J. Comput. Chem.* **2011**, 32, 1687–1693.

[179] Migliore, A. and Nitzan, A. Nonlinear Charge Transport in Redox Molecular Junctions: A Marcus Perspective. *ACS Nano* **2011**, 5(8), 6669–6685.

[180] Migliore, A.; Schiff, P.; and Nitzan, A. On the Relationship between Molecular State and Single Electron Pictures in Simple Electrochemical Junctions. *Phys. Chem. Chem. Phys.* **2012**, 14, 13746–13753.

[181] Zhou, J. and Xu, B. Determining Contact Potential Barrier Effects on Electronic Transport in Single Molecular Junctions. *Appl. Phys. Lett.* **2011**, 99, 42104.

[182] Sek, S. Peptides and Proteins Wired into the Electrical Circuits: An SPM-Based Approach. *Peptide Sci.* **2012**, 100, 71–81.

[183] Pawlowski, J.; Juhaniewicz, J.; Tymecka, D.; and Sek, S. Electron Transfer Across a-Helical Peptide Monolayers: Importance of Interchain Coupling. *Langmuir* **2012**, 28, 17287–17294.

[184] Jia, C. and Guo, X. Molecule-Electrode Interfaces in Molecular Electronic Devices. *Chem. Soc. Rev.* **2013**, 42, 5642–5660.

[185] Amdursky, N.; Marchak, D.; Sepunaru, L.; Pecht, I.; Sheves, M.; and Cahen, D. Electronic Transport via Proteins. *Adv. Mater.* **2014**, 26, 7142–7161.

[186] Venkatramani, R.; Wierzbinski, E.; Waldeck, D. H.; and Beratan, D. N. Breaking the Simple Proportionality between Molecular Conductances and Charge Transfer Rates. *Faraday Discuss.* **2014**, 174, 57–78.

[187] Livshits, G. I.; Stern, A.; Rotem, D.; Borovok, N.; Eidelshtein, G.; Migliore, A.; Penzo, E.; Wind, S. J.; Di Felice, R.; Skourtis, S. S.; Cuevas, J. C.; Gurevich, L.; Kotlyar, A. B.; and Porath, D. Long-Range Charge Transport in Single G-Quadruplex DNA Molecules. *Nat. Nanotech.* **2014**, 9, 1040–1046.

[188] Tschudi, S. E. and Reuter, M. G. Estimating the Landauer-Buttiker Transmission Function from Single Molecule Break Junction Experiments. *Nanotech.* **2016**, 27, 425203.

[189] Elliott, M. and Jones, D. Approaches to Single-Molecule Studies of Metalloprotein Electron Transfer Using Scanning Probe-Based Techniques. *Biochem. Soc. Trans.* **2018**, 46, 1–9.

[190] Fung, E.-D.; Gelbwaser, D.; Taylor, J.; Low, J.; Xia, J.; Davydenko, I.; Campos, L. M.; Marder, S.; Peskin, U.; and Venkataraman, L. Breaking Down Resonance: Nonlinear Transport and the Breakdown of Coherent Tunneling Models in Single Molecule Junctions. *Nano Lett.* **2019**, 19, 2555–2561.

[191] Valianti, S.; Cuevas, J.-C.; and Skourtis, S. S. Charge-Transport Mechanism in Azurin-Based Monolayer Junctions. *J. Phys. Chem. C* **2019**.

[192] Song, X.; Han, B.; Yu, X.; and Hu, W. The Analysis of Charge Transport Mechanism in Molecular Junctions Based on Current-Voltage Characteristics. *Chem. Phys.* **2020**, 528, 110514.

[193] Nichols, R. J. STM Studies of Electron Transfer Through Single Molecules at Electrode-Electrolyte Interfaces. *Electrochim. Acta* **2021**, 387, 138497.

[194] Nawarat, P.; Beach, K.; Meunier, V.; Terrones, H.; Wang, G.-C.; and Lewis, K. M. Voltage-Dependent Barrier Height of Electron Transport through Iron Porphyrin Molecular Junctions. *J. Phys. Chem. C* **2021**, 125, 7350–7357.

[195] Van Nguyen, Q.; Xie, Z.; and Frisbie, C. D. Quantifying Molecular Structure-Tunneling Conductance Relationships: Oligophenylene Dimethanethiol vs Oligophenylene Dithiol Molecular Junctions. *J. Phys. Chem. C* **2021**.

[196] Supur, M. and McCreery, R. L. A Simple, Semiclassical Mechanism for Activationless, Long Range Charge Transport in Molecular Junctions. *ECS J. Sol. Stat. Sci. Technol.*

2022, 11, 45009.

[197] Zhang, B.; Ryan, E.; Wang, X.; Song, W.; and LLindsay, S. Electronic Transport in Molecular Wires of Precisely Controlled Length Built from Modular Proteins. *ACS Nano* **2022**, 16, 1671–1680.

[198] Bera, S.; Govinda, S.; Fereiro, J. A.; Pecht, I.; Sheves, M.; and Cahen, D. Biotin Binding Hardly Affecs Electron Transport Efficiency across Streptavidin Solid-State Junctions. *Langmuir* **2023**, 39, 1394–1403.

[199] Landauer, R. Spatial Variation of Currents and Fields due to Localized Scatterers in Metallic Conduction. *IBM J.* **1957**, pages 223–231.

[200] Simmons, J. G. Generalized Formula for the Electric Tunnel Effect between Similar Electrodes Separated by a Thin Insulating Film. *J. Appl. Phys.* **1963**, 34(6), 1793–1803.

[201] Jiang, X.; van Wonderen, J. H.; Butt, J. N.; Edwards, M. J.; Clarke, T. A.; and Blumberger, J. Which Multi-Heme Protein Complex Transfers Electron More Efficiently? Comparing MtrCAB from Shewanella with OmcS from Geobacter. *J. Phys. Chem. Lett.* **2020**, 11, 9421–9425.

[202] Volpi, R.; Nassau, R.; Norby, M. S.; and Linares, M. Theoretical Study of the Charge-Transfer State Separation within Marcus Theory: The C60-Anthracene Case Study. *ACS Appl. Mater. Interfaces* **2016**, 8, 24722–24736.

[203] Yang, H.; Gajdos, F.; and Blumberger, J. Intermolecular Charge Transfer Parameters, Electron-Phonon Couplings, and the Validity of Polaron Hopping Models in Organic Semiconducting Crystals: Rubrene, Pentacene, and C60. *J. Phys. Chem. C* **2017**, 121, 7689–7696.

[204] Huang, J.; Zarzycki, J.; Gunner, M. R.; Parson, W. W.; Kern, J. F.; Yano, J.; Ducat, D. C.; and Kramer, D. M. Mesoscopic to Macroscopic Electron Transfer by Hopping in a Crystal Network of Cytochromes. *J. Am. Chem. Soc.* **2020**, 142, 10459–10467.

[205] Shuai, Z.; Li, W.; Ren, J.; Jiang, Y.; and Geng, H. Applying Marcus Theory to Describe the Carrier Transport in Organic Semiconductootors: Limitations and Beyond. *J. Chem. Phys.* **2020**, 153, 80902.

[206] Ahart, C. S.; Blumberger, J.; and Rosso, K. M. Polaronic Structure of Excess Electrons and Holes for a Series of Bulk Iron Oxides. *Phys. Chem. Chem. Phys.* **2020**.

[207] Berezin, A. S. and Nazmutdinov, R. R. Monte Carlo Simulations of Heterogeneous Electron Transfer: New Challenges. *Russ. J. Electrochem.* **2017**, 53(10), 1232–1238.

[208] Zhao, J.; Davis, J. J.; Sansom, M. S. P.; and Hung, A. Exploring the Electronic and Mechanical Properties of Protein Using Conducting Atom Force Microscopy. *J. Am. Chem. Soc.* **2004**, 126, 5601–5609.

[209] Verlet, L. Computer "Experiments" on Classical Fluids. I. Thermodynamical Properties of Lennard-Jones Molecules. *Phys. Rev.* **1967**, 159(1), 98–103.

[210] Swope, W. C.; Andersen, H. C.; Berens, P. H.; and Wilson, K. R. Computer Simulation Method for the Calculation of Equlibrium Constants for the Formation of Physical Clusters of Molecules: Application to Small Water Clusters. *J. Chem. Phys.* **1982**, 76(1), 637–649.

[211] Marx, D. and Hutter, J. *Ab Initio Molecular Dynamics: Basic Theory and Advanced*

Methods. Cambridge University Press, **2009**.

[212] Delos, J. B. Theory of Electronic-Transitions in Slow Atomic Collisions. *Rev. Mod. Phys.* **1981**, 53, 287–357.

[213] Rydzewski, J. and Nowak, W. Molecular Dynamics Simulations of Large Systems in Electronic Excited States. In Leszczynski, J.; Kaczmarek-Kedziera, A.; Puzyn, T.; G. Papadopoulos, M.; Reis, H.; and K. Shukla, M., editors, *Handbook of Computational Chemistry*, pages 1917–1941. Springer International Publishing, **2017**.

[214] Ojanpera, A.; Havu, V.; Lehtovaara, L.; and Puska, M. Nonadiabatic Ehrenfest Molecular Dynamics within the Projector Augmented-Wave Method. *J. Chem. Phys.* **2012**, 136, 144103.

[215] Car, R. and Parrinello, M. Unified Approach for Molecular Dynamics and Density-Functional Theory. *Phys. Rev. Lett.* **1985**, 55(22), 2471–2474.

[216] Tuckerman, M. E. *Statistical Mechanics: Theory and Molecular Simulations*. Oxford University Press, **2010**.

[217] Rapaport, D. C. *The Art of Molecular Dynamics Simulation*. Cambridge University Press, **2004**.

[218] Thijssen, J. *Computational Physics*. Cambridge University Press, **2007**.

[219] Frenkel, D. and Smit, B. *Understanding Molecular Simulation: From Algorithms to Applications*. Academic Press, Elsevier, **2002**.

[220] Chipot, C. *Free energy Calculations: Theory and Applications in Chemistry and Biology*. Springer, **2007**.

[221] Zwanzig, R. W. High-Temperature Equation of State by a Perturbation Method. I. Nonpolar Gases. *J. Chem. Phys.* **1954**, 22(8), 1420–1426.

[222] Kirkwood, J. G. Statistical Mechanics of Fluid Mixtures. *J. Chem. Phys.* **1935**, 3, 300–313.

[223] Carter, E. A.; Ciccotti, G.; Hynes, J. T.; and Kapral, R. Constrained Reaction Coordinate Dynamics for the Simulation of Rare Events. *Chem. Phys. Lett.* **1989**, 156(5), 472–477.

[224] Ciccotti, G. and Ferrario, M. Blue Moon Approach to Rare Events. *Mol. Simul.* **2004**, 30, 787–793.

[225] Ciccotti, G.; Kapral, R.; and Vanden-Eijnden, E. Blue Moon Sampling, Vectorial Reaction Coordinates, and Unbiased CConstrained Dynamics. *ChemPhysChem* **2005**, 6, 1809–1814.

[226] Fleurat-Lessard, P. and Ziegler, T. Tracing the Minimum-Energy Path on the Free-Energy Surface. *J. Chem. Phys.* **2005**, 123, 84101.

[227] Komeiji, Y. Implementation of the Blue Moon Ensemble Method. *Chem. Bio. Inf. J.* **2007**, 7(1), 12–23.

[228] Torrie, G. M. and Valleau, J. P. Monte Carlo Free Energy Estimates Using Non-Boltzmann Sampling: Application to the Sub-critical Lennard-Jones Fluid. *Chem. Phys. Lett.* **1974**, 28(4), 578–581.

[229] Torrie, G. M. and Valleau, J. P. Nonphysical Sampling Distributions in Monte Carlo Free-Energy Estimation: Umbrella Sampling. *J. Comput. Phys.* **1977**, 23, 187–199.

[230] Kumar, S.; Bouzida, D.; Swendsen, R. H.; Kollman, P. A.; and Rosenberg, J. M. The Weighted Histogram Analysis Method for Free-Energy Calculations on Biomolecules. I. The Method. *J. Comput. Chem.* **1992**, 13(8), 1011–1021.

[231] Kumar, S.; Rosenberg, J. M.; Bouzida, D.; Swendsen, R. H.; and Kollman, P. A. Multidimensional Free-Energy Calculation Using the Weighted Histogram Analysis Method. *J. Comput. Chem.* **1995**, 16(11), 1339–1350.

[232] Kumar, S.; Payne, P. W.; and Vasquez, M. Method for Free-Energy Calculations Using Iterative Techniques. *J. Comput. Chem.* **1996**, 17(10), 1269–1275.

[233] Laio, A. and Parrinello, M. Escaping Free-Energy Minima. *Proc. Nat. Acad. Sci.* **2002**, 99, 12526–12566.

[234] Ensing, B.; De Vivo, M.; Liu, Z.; Moore, P.; and Klein, M. L. Metadynamics as a Tool for Exploring Free Energy Landscapes of Chemical Reactions. *Acc. Chem. Res.* **2006**, 39, 73–81.

[235] Laio, A. and Gervasio, F. L. Metadynamics: A Method to Simulate Rare Events and Reconstruct the Free Energy in Biophysics, Chemistry and Material Science. *Rep. Prog. Phys.* **2008**, 71, 126601.

[236] Branduardi, D.; Bussi, G.; and Parrinello, M. Metadynamics with Adaptive Gaussians. *J. Chem. Theory Comput.* **2012**, 8, 2247–2254.

[237] Dama, J. F.; Rotskoff, G.; Parrinello, M.; and Voth, G. A. Transition-Tempered Metadynamics: Robust, Convergent Metadynamics via On-the-Fly Transition Barrier Estimation. *J. Chem. Theory Comput.* **2014**, 10, 3626–3633.

[238] Joy, J.; Stuyver, T.; and Shaik, S. Oriented External Electric Fields and Ionic Additives Elicit Catalysis and Mechanistic Crossover in Oxidative Addition Reactions. *J. Am. Chem. Soc.* **2020**, 142, 3836–3850.

[239] English, N. J. Molecular Simulation of External Electric Fields on the Crystal State: A Perspective. *Crystals* **2021**, 11, 1405.

[240] Souza, I.; Iniguez, J.; and Vanderbilt, D. First-Principles Approach to Insulators in Finite Electric Fields. *Phys. Rev. Lett.* **2002**, 89(11), 117602.

[241] Meir, R.; Chen, H.; Lai, W.; and Shaik, S. Oriented Electric Fields Accelerate Diels-Alder Reactions and Control the endo/exo Selectivity. *ChemPhysChem* **2010**, 11, 301–310.

[242] Wang, Z.; Danovich, D.; Ramanan, R.; and Shaik, S. Oriented-External Electric Fields Create Absolute Enantioselectivity in Diels-Alder Reactions: Importance of the Molecular Dipole Moment. *J. Am. Chem. Soc.* **2018**, 140, 13350–13359.

[243] Stuyver, T.; Danovich, D.; Joy, J.; and Shaik, S. External Electric Field Effects on Chemical Structure and Reactivity. *WIREs Comput. Mol. Sci.* **2019**, 10, 1438.

[244] Yu, L.-J. and Coote, M. L. Electrostatic Switching between SN1 and SN2 Pathways. *J. Phys. Chem. A* **2019**, 123, 582–589.

[245] Dubey, K. D.; Stuyver, T.; Kalita, S.; and Shaik, S. Solvent Organization and Rate Regulation of a Menshutkin Reaction by Oriented External Electric Fields are Revealed by Combined MD and QM/MM Calculations. *J. Am. Chem. Soc.* **2020**, 142, 9955–9965.

[246] Ojha, D. and Kuhne, T. D. Vibrational Dynamics of Liquid Water in an External Electric Field. *Phys. Chem. Chem. Phys.* **2023**.

[247] English, N. J. and Mooney, D. A. Denaturation of Hen Egg White Lysozyme in Electromagnetic Fields: A Molecular Dynamics Study. *J. Chem. Phys.* **2007**, 126, 91105.

[248] English, N. J.; Solomentsev, G. Y.; and O'Brien, P. Nonequilibrium Molecular Dynamics Study of Electric and Low-Frequency Microwave Fields on Hen Egg White Lysozyme. *J. Chem. Phys.* **2009**, 131, 35106.

[249] Nandi, P. K.; Futera, Z.; and English, N. J. Perturbation of Hydration Layer in Solvated Proteins by External Electric and Electromagnetic Fields: Insight from Non-Equilibrium Molecular Dynamics. *J. Chem. Phys.* **2016**, 145, 205101.

[250] Biriukov, D. and Futera, Z. Adsorption of Amino Acids at the Gold/Aqueous Interface: Effect of an External Electric Field. *J. Phys. Chem. C* **2021**, 125, 7856–7867.

[251] Kalita, S.; Bergman, H.; Dubey, K. D.; and Shaik, S. How Can Static and Oscillating Electric Fields Serve in Decomposing Alzheimer's and Other Senile Plaques? *J. Am. Chem. Soc.* **2023**, 145, 3543–3553.

[252] Warshel, A. Dynamics of Reactions in Polar Solvents. Semiclassical Trajectory Studies of Electron-Transfer and Proton-Transfer Reactions. *J. Phys. Chem.* **1982**, 86, 2218–2224.

[253] Kubas, A.; Hoffmann, F.; Heck, A.; Oberhofer, H.; Elstner, M.; and Blumberger, J. Electronic Couplings for Molecular Charge Transfer: Benchmarking CDFT, FODFT, and FODFTB Against High-Level Ab Initio Calculations. *J. Chem. Phys.* **2014**, 140, 104105.

[254] Kubas, A.; Gajdos, F.; Heck, A.; Oberhofer, H.; Elstner, M.; and Blumberger, J. Electronic Couplings for Molecular Charge Transfer: Benchmarking CDFT, FODFT and FODFTB Against High-Level Ab Initio Calculation. II. *Phys. Chem. Chem. Phys.* **2015**, 17, 14342–14354.

[255] Manna, D.; Blumberger, J.; Martin, J. M. L.; and Krronik, L. Prediction of Electronic Couplings for Molecular Charge Transfer Using Optimally Tuned Range-Separated Hybrid Functionals. *Mol. Phys.* **2018**, 116, 2497–2505.

[256] Ziogos, O. G.; Kubas, A.; Futera, Z.; Xie, W.; Elstner, M.; and Blumberger, J. HAB79: A New Molecular Dataset for Benchmarking DFT and DFTB Electronic Couplings Against High-Level Ab Initio Calculations. *J. Chem. Phys.* **2021**, 155, 234115.

[257] Farazdel, A.; Dupuis, M.; Clementi, E.; and Aviram, A. Electric Field Induced Intramolecular Electron Transfer in Spiro pi-Electron Systems and Their Suitability as Molecular Electronic Devices. A Theoretical Study. *J. Am. Chem. Soc.* **1990**, 112, 4206–4214.

[258] Calzado, C. J.; Malrieu, J.-P.; and Sanz, J. F. Physical Factors Governing the Amplitude of the Electron Transfer Intergral in Mixed-Valence Compounds. *J. Phys. Chem. A* **1998**, 102, 3659–3667.

[259] Calzado, C. J. and Sanz, J. F. Ab Initio Calculations of the Electron-Transfer Matrix Element in Cu(I)-Cu(II) Mixed-Valence Compounds. *J. Am. Chem. Soc.* **1998**, 120, 1051–1061.

[260] Wells, M. C. and Lucchese, R. R. Multidimensional Configuration-Space Models of the Electronic Factor in Electron Transfer by Superexchange: Implications for Models of Biological Electron Transfer. *J. Phys. Chem. A* **1999**, 103, 7345–7356.

[261] Pati, R. and Karna, S. P. Ab Initio Hartree-Fock Study of Electron Transfer in Organic Molecules. *J. Chem. Phys.* **2001**, 115, 1703–1715.

[262] Mo, Y.; Wu, W.; and Zhang, Q. Study of Intramolecular Electron Transfer with a Two-State Model Based on the Orbital Deletion Procedure. *J. Chem. Phys.* **2003**, 119, 6448–6456.

[263] Smith, D. M. A.; Rosso, K. M.; Dupuis, M.; Valiev, M.; and Straatsma, T. P. Electronic Coupling Between Heme Electron-Transfer Centers and Its Decay with Distance Depends Strongly on Relative Orientation. *J. Phys. Chem. B* **2006**, 110, 15582–15588.

[264] Spencer, J.; Scalfi, L.; Carof, A.; and Blumberger, J. Confronting Surface Hopping Molecular Dynamics with Marcus Theory for a Molecular Donor-Acceptor System. *Faraday Discuss.* **2016**, 195, 215–236.

[265] Spencer, J.; Gajdos, F.; and Blumberger, J. FOB-SH: Fragment Orbital-Based Hopping for Charge Carrier Transport in Organic and Biological Molecules and Materials. *J. Chem. Phys.* **2016**, 145, 64102.

[266] Cherepanov, D. A.; Shelaev, I. V.; Gostev, F. E.; Mamedov, M. D.; Petrova, A. A.; Aybush, A. V.; Shuvalov, V. A.; Semenov, A. Y.; and Nadtochenko, V. A. Mechanism of Adiabatic Primary Electron Transfer in Photosystem I: Femtosecond Spectroscopy upon Excitation of Reaction Center in the Far-Red Edge of the QY Band. *Biochim. Biophys. Acta Bioenerg.* **2017**, 1858, 895–905.

[267] Giannini, S.; Carof, A.; Ellis, M.; Yang, H.; Ziogos, O. G.; Ghosh, S.; and Blumberger, J. Quantum Localization and Delocalization of Charge Carriers in Organic Semiconducting Crystals. *Nat. Comm.* **2019**, 10, 3843.

[268] Nematiaram, T. and Troisi, A. Modeling Charge Transport in High-Mobility Molecular Semiconductors: Balancing Electronic Structure and Quantum Dynamics Methods withthe Help of Experiments. *J. Chem. Phys.* **2020**, 152, 190902.

[269] Gajdos, F.; Valner, S.; Hoffmann, F.; Spencer, J.; Breuer, M.; Kubas, A.; Dupuis, M.; and Blumberger, J. Ultrafast Estimation of Electronic Couplings for Electron Transfer Between p-Conjugated Organic Molecules. *J. Chem. Theory Comput.* **2014**, 10, 4653–4660.

[270] Ziogos, O. G. and Blumberger, J. Ultrafast Estimation of Electronic Couplings for Electron Transfer between pi-Conjugated Organic Molecules. II. *J. Chem. Phys.* **2021**, 155, 244110.

[271] Mulliken, R. S. Molecular Compounds and Their Spectra. II. *J. Am. Chem. Soc.* **1952**, 74, 811–824.

[272] Reimers, J. R. and Hush, N. S. Electronic Properties of Transition-Metal Complexes Determined from Electroabsorption (Stark) Spectroscopy. 2. Mononuclear Complexes of Ruthenium(II). *J. Phys. Chem.* **1991**, 95, 9773–9781.

[273] Creutz, C.; Newton, M. D.; and Sutin, N. Metal-Ligand and Metal-Metal Coupling Elements. *J. Photochem. Photobiol. A: Chem.* **1994**, 82, 47–59.

[274] Cave, R. J. and Newton, M. D. Generalization of the Mulliken-Hush Treatment for the Calculation of Electron Transfer Matrix Elements. *Chem. Phys. Lett.* **1996**, 249, 15–19.

[275] Cave, R. J. and Newton, M. D. Calculation of Electronic Coupling Matrix Elements for Ground and Excited State Electron Transfer Reactions: Comparison of the Generalized Mulliken-Hush and Block Diagonalization Methods. *J. Chem. Phys.* **1997**, 106, 9213–9226.

[276] Cukier, E.; Daniels, S.; Vinson, E.; and Cave, R. J. Are Hydrogen Bonds Unique Among Weak Interactions in Their Ability to Mediate Electronic Coupling? *J. Phys. Chem. A* **2002**, 106, 11240–11247.

[277] Yi, B.-H.; Li, X.-Y.; Yang, S.-Y.; and Duan, X.-H. Theoretical Investigation of Charge Transfer Excitation and Charge Recombination in Acenaphthylene-Tetracyanoethylene Complex. *Int. J. Quant. Chem.* **2003**, 94, 23–35.

[278] Chen, H.-C. and Hsu, C.-P. Ab Initio Characterization of Electron Transfer Coupling in Photoinduced Systems: Generalized Mulliken-Hush with Configuration-Interaction Singles. *J. Phys. Chem. A* **2005**, 109, 11989–11995.

[279] Pieniazek, P. A.; Arnstein, S. A.; Bradforth, S. E.; Krylov, A. I.; and Sherrill, C. D. Benchmark Full Configuration Interaction and Equation-of-Motion Coupled-Cluster Model with Single and Double Substitutions for Ionized Systems Results for Prototypical Charge Transfer Systems: Noncovalent Ionized Dimers. *J. Chem. Phys.* **2007**, 127, 164110.

[280] Voityuk, A. A. Electronic Couplings for Photoinduced Electron Transfer and Excitation Energy Transfer Computed Using Excited States of Noninteracting Molecules. *J. Phys. Chem. A* **2017**, 121, 5414–5419.

[281] Kubas, A. How the Donor/Acceptor Spin States Affect the Electronic Coupling in Molecular Charge-Transfer Processes? *J. Chem. Theory Comput.* **2021**.

[282] Voityuk, A. A. and Rosch, N. Quantum Chemical Modeling of Electron Hole Transfer Through pi Stacks of Normal and Modified Pairs of Nucleobases. *J. Phys. Chem. B* **2002**, 106, 3013–3018.

[283] Hsu, C.-P.; You, Z.-Q.; and Chen, H.-C. Characterization of the Short-Range Couplings in Excitation Energy Transfer. *J. Phys. Chem. C* **2008**, 112, 1204–1212.

[284] Hsu, C.-P. The Electronic Couplings in Electron Transfer and Excitation Energy Transfer. *Acc. Chem. Res.* **2009**, 42, 509–518.

[285] Ramos, F. C.; Nottoli, M.; Cupellini, L.; and Mennucci, B. The Molecular Mechanism of Light Adaptation in Light-Harvesting Complexes of Purple Bacteria Revealed by a Multiscale Modeling. *Chem. Sci.* **2019**, 10, 9650–9662.

[286] Tejeda-Ferrari, M. E.; Brown, C. L.; Coutinho, G. C. C. C.; Gomes de Sa, G. A.; Palma, J. L.; Llansola-Portoles, M. J.; Kodis, G.; Mujica, V.; Ho, J.; Gust, D.; Moore, T. A.; and Moore, A. L. Electronic Structure and Triplet-Triplet Energy Transfer in Artificial Photosynthetic Antennas. *Photochem. Photobiol.* **2019**, 95, 211–219.

[287] Cupellini, L.; Corbella, M.; Mennucci, B.; and Curutchet, C. Electronic Energy Transfer in Biomacromolecules. *WIREs Comput. Mol. Sci.* **2019**, 9, 1392.

[288] Roy, P. P.; Kundu, S.; Valdiviezo, J.; Bullard, G.; Fletcher, J. T.; Liu, R.; Yang, S.-J.; Zhang, P.; Beratan, D. N.; Therien, M. J.; Makri, N.; and Fleming, G. R. Synthetic Control of Exciton Dynamics in Bioinspired Cofacial Porphyrin Dimers. *J. Am. Chem. Soc.* **2022**, 144, 6298–6310.

[289] Yost, S. R.; Hontz, E.; Yeganeh, S.; and Van Voorhis, T. Triplet vs Singlet Energy Transfer in Organic Semiconductors: The Tortoise and the Hare. *J. Phys. Chem. C* **2012**, 116, 17369–17377.

[290] Fornari, R. P.; Rowe, P.; Padula, D.; and Troisi, A. Importance and Nature of Short-Range

Excitonic Interactions in Light Harvesting Complexes and Organic Semiconductors. *J. Chem. Theory Comput.* **2017**, 13, 3754–3763.

[291] Price, M. B.; Hume, P. A.; Ilina, A.; Wagner, I.; Tamming, R. R.; Thorn, K. E.; Jiao, W.; Goldingay, A.; Conaghan, P. J.; Lakhwani, G.; Davis, N. J. L. K.; Wang, Y.; Xue, P.; Lu, H.; Chen, K.; Zhan, X.; and Hodgkiss, J. M. Free Charge Photogeneration in a Single Component High Photovoltaic Efficiency Organic Semiconductor. *Nat. Comm.* **2022**, 13, 2827.

[292] Polo, V.; Kraka, E.; and Cremer, D. Electron Correlation and the Self-Interaction Error of Density Functional Theory. *Mol. Phys.* **2002**, 100, 1771–1790.

[293] Mori-Sanchez, P.; Cohen, A. J.; and Yang, W. Localization and Delocalization Errors in Density Functional Theory and Implications for Band-Gap Prediction. *Phys. Rev. Lett.* **2008**, 100, 146401.

[294] Tsuneda, T. and Hirao, K. Self-Interaction Corrections in Density Functional Theory. *J. Chem. Phys.* **2014**, 140, 513.

[295] Hait, D. and Head-Gordon, M. Delocalization Errors in Density Functional Theory Are Essentially Quadratic in Fractional Occupation Number. *J. Phys. Chem. Lett.* **2018**, 9, 6280–6288.

[296] Wu, Q. and Van Voorhis, T. Extracting Electron Transfer Coupling Elements from Constrained Density Functional Theory. *J. Chem. Phys.* **2006**, 125, 164105.

[297] Wu, Q. and Van Voorhis, T. Direct Calculation of Electron Transfer Parameters Through Constrained Density Functional Theory. *J. Phys. Chem. A* **2006**, 110, 9212–9218.

[298] Oberhofer, H. and Blumberger, J. Electronic Coupling Matrix Elements From Charge Constrained Density Functional Theory Calculations Using a Plane Wave Basis Set. *J. Chem. Phys.* **2010**, 133, 244105.

[299] Senthilkumar, K.; Grozema, F. C.; Bickelhaupt, F. M.; and Siebbeles, L. D. A. Charge Transport in Columnar Stacked Triphenylenes: Effects of Conformational Fluctuations on Charge Transfer Integrals and Site Energies. *J. Chem. Phys.* **2003**, 119(18), 9809–9817.

[300] Oberhofer, H. and Blumberger, J. Insight into the Mechanism of the Ru2+-Ru3+ Electron Self-Exhchange Reaction from Quantitative Rate Calculations. *Angew. Chem. Int. Ed.* **2010**, 49, 3631–3634.

[301] Oberhofer, H. and Blumberger, J. Revisiting Electronic Couplings and Incoherent Hopping Models for Electron Transport in Crystalline C60 at Ambient Temperatures. *Phys. Chem. Chem. Phys.* **2012**, 14, 13846–13852.

[302] Gajdos, F.; Oberhofer, H.; Dupuis, M.; and Blumberger, J. On the Inapplicability of Electron-Hopping Models for the Organic Semiconductor Phenyl-C61-butyric Acid Methyl Ester (PCBM). *J. Phys. Chem. Lett.* **2013**, 4, 1012–1017.

[303] Szabo, A. and Ostlund, N. S. *Modern Quantum Chemistry: Introduction to Advanced Electronic Structure Theory.* Dover Publications, **1996**.

[304] Kondov, I.; Cizek, M.; Benesch, C.; Wang, H.; and Thoss, M. Quantum Dynamics of Photoinduced Electron-Transfer Reactions in Dye-Semiconductor Systems: First-Principles Description and Application to Coumarin 343-TiO2. *J. Phys. Chem. C* **2007**, 111, 11970–11981.

[305] Futera, Z. and Blumberger, J. Correction to "Electronic Couplings for Charge Transfer across Molecule/Metal and Molecule/Semiconductor Interfaces: Performance of the Projector Operator-Based Diabatization Approach". *J. Phys. Chem. C* **2022**, 126, 3301–3303.

[306] VandeVondele, J.; Krack, M.; Mohamed, F.; Parrinello, M.; Chassaing, T.; and Hutter, J. Quickstep: Fast and Accurate Density Functional Calculations Using a Mixed Gaussian and Plane Waves Approach. *Comp. Phys. Comm.* **2005**, 167, 103–128.

[307] Hutter, J.; Iannuzzi, M.; Schiffmann, F.; and VandeVondele, J. CP2K: Atomistic Simulations of Condensed Matter Systems. *WIREs Comput. Mol. Sci.* **2014**, 4, 15–25.

[308] Kuhne, T. D.; Iannuzzi, M.; Del Ben, M.; Rybnik, V. V.; Seewald, P.; Stein, F.; Laino, T.; Khaliullin, R. Z.; Schutt, O.; Schiffmann, F.; Golze, D.; Wilhelm, J.; Chulkov, S.; Bani-Hashemian, M. H.; Weber, V.; Borstnik, U.; Taillefumier, M.; Jakobovits, A. S.; Lazzaro, A.; Pabst, H.; Muller, T.; Schade, R.; Guidon, M.; Andermatt, S.; Holmberg, N.; Schenter, G. K.; Hehn, A.; Bussy, A.; Belleflamme, F.; Tabacchi, G.; Gloss, A.; Lass, M.; Bethune, I.; Mundy, C. J.; Plessl, C.; Watkins, M.; VandeVondele, J.; Krack, M.; and Hutter, J. CP2K: An Electronic Structure and Molecular Dynamics Software Package - Quickstep: Efficient and Accurate Electronic Structure Calculations. *J. Chem. Phys.* **2020**, 152, 194103.

[309] Perdew, J. P.; Burke, K.; and Ernzerhof, M. Generalized Gradient Approximation Made Simple. *Phys. Rev. Lett.* **1996**, 77(18), 3865–3868.

[310] Perdew, J. P.; Burke, K.; and Ernzerhof, M. Errata: Generalized Gradient Approximation Made Simple [Phys. Rev. Lett. 77, 3865 (1996)]. *Phys. Rev. Lett.* **1997**, 78, 1396.

[311] Rohrdanz, M. A.; Martins, K. M.; and Herbert, J. M. A Long-Range-Corrected Density Functional that Performs Well for Both Ground-State Properties and Time-Dependent Density Functional Theory Excitation Energies, Including Charge-Transfer Excited States. *J. Chem. Phys.* **2009**, 130, 54112.

[312] Becke, A. D. Density-Functional Thermochemistry. V. Systematic Optimization of Exchange-Correlation Functionals. *J. Chem. Phys.* **1997**, 107, 8554–8560.

[313] Chai, J.-D. and Head-Gordon, M. Systematic Optimization of Long-Range Corrected Hybrid Density Functionals. *J. Chem. Phys.* **2008**, 128, 84106.

[314] Ghan, S.; Kunkel, C.; Reuter, K.; and Oberhofer, H. Improved Projection-Operator Diabatization Schemes for the Calculation of Electronic Coupling Values. *J. Chem. Theory Comput.* **2020**.

[315] Jiang, X.; Futera, Z.; Ali, M. E.; Gajdos, F.; von Rudorff, G. F.; Carof, A.; Breuer, M.; and Blumberger, J. Correction to "Cysteine Linkages Accelerate Electron Flow through Tetra-Heme Protein STC". *J. Am. Chem. Soc.* **2022**, 144, 7010–7012.

[316] Trasatti, S. The Absolute Electrode Potential: An Explanatory Note. *Pure Appl. Chem.* **1986**, 58(7), 955–966.

[317] Anderson, A. B. and Albu, T. V. Ab Initio Determination of Reversible Potentials and Activation Energies for Outer-Sphere Oxygen Reduction to Water and the Reverse Oxidation Reaction. *J. Am. Chem. Soc.* **1999**, 121, 11855–11863.

[318] Winget, P.; Weber, E. J.; Cramer, C. J.; and Truhlar, D. G. Computational Electrochemistry: Aqueous One-Electron Oxidation Potentials for Substituted Anilines. *Phys. Chem.*

Chem. Phys. **2000**, 2, 1231–1239.

[319] Lewis, A.; Bumpus, J. A.; Truhlar, D. G.; and Cramer, C. J. Molecular Modeling of Environmentally Important Processes: Reduction Potentials. *J. Chem. Edu.* **2004**, 81(4), 596–603.

[320] Moens, J.; Geerlings, P.; and Roos, G. A Conceptual DFT Approach for the Evaluation and Interpretation of Redox Potentials. *Chem. Eur. J.* **2007**, 13, 8174–8184.

[321] Jaque, P.; Marenich, A. V.; Cramer, C. J.; and Truhlar, D. G. Computational Electrochemistry: The Aqueous Ru3+/Ru2+ Reduction Potential. *J. Phys. Chem. C* **2007**, 111, 5783–5799.

[322] Kelly, C. P.; Cramer, C. J.; and Truhlar, D. G. Single-Ion Solvation Free Energies and the Normal Hydrogen Electrode Potential in Methanol, Acetonitrile, and Dimethyl Sulfoxide. *J. Phys. Chem. B* **2007**, 11, 408–422.

[323] Guerard, J. J. and Arey, J. S. Critical Evaluation of Implicit Solvent Models for Predicting Aqueous Oxidation Potentials of Neutral Organic Compounds. *J. Chem. Theory Comput.* **2013**, 9, 5046–5058.

[324] Matsui, T. and Song, J.-W. A Density Functional Theory-Based Scheme to Compute the Redox Potential of a Transition Metal Complex: Applications to Heme Compound. *Molec* **2019**, 24, 819.

[325] Diers, J. R.; Kirmaier, C.; Taniguchi, M.; Lindsey, J. S.; Bocian, D. F.; and Holten, D. A Perspective on the Redox Properties of Tetrapyrrole Macrocycles. *Phys. Chem. Chem. Phys.* **2021**, 23, 19130–19140.

[326] Miertus, S.; Scrocco, E.; and Tomasi, J. Electrostatic Interaction of a Solute with a Continuum. A Direct Utilizatoin of Ab Initio Molecular Potentials for the Prevision of Solvent Effects. *Chem. Phys.* **1981**, 55, 117–129.

[327] Klamt, A. and Schuurmann, G. COSMO: A New Approach to Dielectric Screening in Solvents with Explicit Expressions for the Screening Energy and its Gradient. *J. Chem. Soc. Perkin Trans. 2* **1993**, pages 799–805.

[328] Klamt, A. Conductor-like Screening Model for Real Solvents: A New Approach to the Quantitative Calculation of Solvation Phenomena. *J. Phys. Chem.* **1995**, 99, 2224–2235.

[329] Cances, E.; Mennucci, B.; and Tomasi, J. A New Integral Equation Formalism for the Polarizable Continuum Model: Theoretical Background and Applications to Isotropic and Anisotropic Dielectrics. *J. Chem. Phys.* **1997**, 107(8), 3032–3041.

[330] Kelly, C. P.; Cramer, C. J.; and Truhlar, D. G. SM6: A Density Functional Theory Contiuum Solvation Model for Calculating Aqueous Solvation Free Energies of Neutrals, Ions, and Solute-Water Clusters. *J. Chem. Theory Comput.* **2005**, 1, 1133–1152.

[331] Tomasi, J.; Mennucci, B.; and Cammi, R. Quantum Mechanical Continuum Solvation Models. *Chem. Rev.* **2005**, 105, 2999–3093.

[332] Nelsen, S. F.; Blackstock, S. C.; and Kim, Y. Estimation of Inner Shell Marcus Terms for Amino Nitrogen Compounds by Molecular Orbital Calculations. *J. Am. Chem. Soc.* **1987**, 109, 677–682.

[333] Nelsen, S. F.; Adamus, J.; and Wolff, J. J. Comparison of Intramolecular Electron Transfer Rate Constant with Hush Theory for an Organic Intervalence Compound. *J. Am. Chem.*

Soc. **1994**, 116, 1589–1590.

[334] Lopez-Estrada, O.; Laguna, H. G.; Barrueta-Flores, C.; and Amador-Bedolla, C. Reassessment of the Four-Point Approach to the Electron-Transfer Marcus–Hush Theory. *ACS Omega* **2018**, 3, 2130–2140.

[335] Levitt, M. and Warshel, A. Computer Simulation of Protein Folding. *Nature* **1975**, 253, 694–698.

[336] Singh, U. C. and Kollman, P. A. A Combined Ab Initio Quantum Mechanical and Molecular Mechanical Method for Carrying out Simulations on Complex Molecular Systems: Applications to the CH3Cl + Cl- Exchange Reaction and Gas Phase Protonation of Polyethers. *J. Comput. Chem.* **1986**, 7(6), 718–730.

[337] Field, M. J.; Bash, P. A.; and Karplus, M. A Combined Quantum Mechanical and Molecular Mechanical Potential for Molecular Dynamics Simulations. *J. Comput. Chem.* **1990**, 11(6), 700–733.

[338] Maseras, F. and Morokuma, K. IMOMM: A New Integrated Ab Initio Molecular Mechanics Geometry Optimization Scheme of Equilibrium Structures and Transition States. *J. Comput. Chem.* **1995**, 16(9), 1170–1179.

[339] Gao, J. Hybrid Quantum and Molecular Mechanical Simulations: An Alternative Avenue to Solvent Effects in Organic Chemistry. *Acc. Chem. Res.* **1996**, 29, 298–305.

[340] Cui, Q. and Karplus, M. Molecular Properties from Combined QM/MM Methods. I. Analytical Second Derivative and Vibrational Calculations. *J. Chem. Phys.* **2000**, 112(3), 1133–1149.

[341] Senn, H. M. and Thiel, W. QM/MM Methods for Biomolecular Systems. *Angew. Chem. Int. Ed.* **2009**, 48, 1198–1229.

[342] Aschi, M.; Spezia, R.; Di Nola, A.; and Amadei, A. A First-Principles Method to Model Perturbed Electronic Wavefunctions: The Effect of an External Homogeneous Electric Field. *Chem. Phys. Lett.* **2001**, 344, 374–380.

[343] Spezia, R.; Aschi, M.; Di Nola, A.; and Amadei, A. Extension of the Perturbed Matrix Method: Application to a Water Molecule. *Chem. Phys. Lett.* **2002**, 365, 450–456.

[344] Amadei, A.; D'Alessandro, M.; and Aschii, M. Statistical Mechanical Modeling of Chemical Reactions in Complex Systems: The Reaction Free Energy Surface. *J. Phys. Chem. B* **2004**, 108, 16250–16254.

[345] Amadei, A.; D'Alessandro, M.; D'Abramo, M.; and Aschi, M. Theoretical Characterization of Electronic States in Interacting Chemical Systems. *J. Chem. Phys.* **2009**, 130, 84109.

[346] Zanetti-Polzi, L.; Del Galdo, S.; Daidone, I.; D'Abramo, M.; Barone, V.; Aschi, M.; and Amadei, A. Extending the Perturbed Matrix Method Beyond the Dipolar Approximation: Comparison of Different Levels of Theory. *Phys. Chem. Chem. Phys.* **2018**, 20, 24369–24378.

[347] Reynolds, C. A.; King, P. M.; and Richards, G. W. Computed Redox Potentials and the Design of Bioreductive Agents. *Nature* **1988**, 334, 80–82.

[348] Ryde, U. Combined Quantum and Molecular Mechanical Calculations on Metalloproteins. *Curr. Opin. Chem. Biol.* **2003**, 7, 136–142.

[349] van den Bosch, M.; Swart, M.; Snijders, J. G.; Berendsen, H. J. C.; Mark, A. E.; Oostenbrink, C.; van Gunsteren, W. F.; and Canters, G. W. Calculation of the Redox Potential of the Protein Azurin and Some Mutants. *ChemBioChem* **2005**, 6, 738–746.

[350] Sattelle, B. M. and Sutcliffe, M. J. Calculating Chemically Accurate Redox Potentials for Engineered Flavoproteins from Classical Molecular Dynamics Free Energy Simulations. *J. Phys. Chem. A* **2008**, 112, 13053–13057.

[351] Kamerlin, S. C. L.; Haranczyk, M.; and Warshel, A. Progress in Ab Initio QM/MM Free-Energy Simulations of Electrostatic Energies in Proteins: Accelerated QM/MM Studies of pKa, Redox Reactions and Solvation Free Energies. *J. Phys. Chem. B* **2009**, 113, 1253–1272.

[352] Guerard, J. J.; Tentscher, P. R.; Seijo, M.; and Arey, J. S. Explicit Solvent Simulations of the Aqueous Oxidation Potential and Reorganization Energy for Neutral Molecules: Gas Phase, Linear Solvent Response, and Non-Linear Response Contributions. *Phys. Chem. Chem. Phys.* **2015**, 17, 14811–14826.

[353] Saito, K.; Mandal, M.; and Ishikita, H. Redox Potentials Along the Redox-Active Low-Barrier H-Bonds in Electron Transfer Pathways. *Phys. Chem. Chem. Phys.* **2020**, 22, 25467–25473.

[354] Nicholson, M. I. G.; Bueno, P. R.; and Feliciano, G. T. Ab Initio QM/MM Simulation of Ferrocene Homogeneous Electron-Transfer RReaction. *J. Phys. Chem. A* **2021**, 125, 25–33.

[355] Cascella, M.; Magistrato, A.; Tavernelli, I.; Carloni, P.; and Rothlisberger, U. Role of Protein Frame and Solvent for the Redox Properties of Azurin from Pseudomonas aeruginosa. *Proc. Nat. Acad. Sci.* **2006**, 103, 19641–19646.

[356] Blumberger, J. Free Energies for Biological Electron Transfer From QM/MM Calculation: Method, Application and Critical Assessment. *Phys. Chem. Chem. Phys.* **2008**, 10, 5651–5667.

[357] Vazquez-Duhalt, R.; Aguila, S. A.; Arrocha, A. A.; and Ayala, M. QM/MM Molecular Modeling and Marcus Theory in the Molecular Design of Electrodes for Enzymatic Fuel Cells. *ChemElectroChem* **2014**, 1, 496–513.

[358] Kontkanen, O. V.; Biriukov, D.; and Futera, Z. Applicability of Perturbed Matrix Method for Charge Transfer Studies at Bio/Metallic Interfaces: A Case of Azurin. *Phys. Chem. Chem. Phys.* **2023**, 25, 12479–12489.

[359] Quek, S. Y.; Venkataraman, L.; Choi, H. J.; Louie, S. G.; Hybertsen, M. S.; and Neaton, J. B. Amine-Gold Linked Single-Molecule Circuits: Experiment and Theory. *Nano Lett.* **2007**, 7(11), 3477–3482.

[360] Baer, R.; Livshits, E.; and Salzner, U. Tuned Range-Separated Hybrids in Density Functional Theory. *Ann. Rev. Phys. Chem.* **2010**, 61, 85–109.

[361] Stein, T.; Eisenberg, H.; Kronik, L.; and Baer, R. Fundamental Gaps in Finite Systems from Eigenvalues of a Generalized Kohn-Sham Method. *Phys. Rev. Lett.* **2010**, 105, 266802.

[362] Kronik, L.; Stein, T.; Refaely-Abramson, S.; and Baer, R. Excitation Gaps of Finite-Sized Systems from Optimally Tuned Range-Separated Hybrid Functionals. *J. Chem. Theory Comput.* **2012**, 8, 1515–1531.

[363] Futera, Z.; Sodeyama, K.; Burda, J. V.; Einaga, Y.; and Tateyama, Y. A Double-QM/MM Method for Investigating Donor-Acceptor Electron-Transfer Reactions in Solution. *Phys. Chem. Chem. Phys.* **2014**, 16, 19530–19539.

[364] Futera, Z. and Burda, J. V. Reaction Mechanism of Ru(II) Piano-Stool Complexes: Umbrella Sampling QM/MM MD Study. *J. Comput. Chem.* **2014**, 35, 1446–1456.

[365] Futera, Z.; Watanabe, T.; Einaga, Y.; and Tateyama, Y. First Principles Calculation Study on Surfaces and Water Interfaces of Boron-Doped Diamond. *J. Phys. Chem. C* **2014**, 118, 22040–22052.

[366] Carof, A.; Giannini, S.; and Blumberger, J. Detailed Balance, Internal Consistency, and Energy Conservation in Fragment Orbital-Based Surface Hopping. *J. Chem. Phys.* **2017**, 147, 214113.

[367] Joachim, C. and Ratner, M. A. Molecular Electronics: Some Views on Transport Junctions and Beyond. *Proc. Nat. Acad. Sci.* **2005**, 102(25), 8801–8808.

[368] Noy, A. Bionanoelectronics. *Adv. Mater.* **2011**, 23, 807–820.

[369] Zhang, A. and Lieber, C. M. Nano-Bioelecronics. *Chem. Rev.* **2016**, 116, 215–257.

[370] Bostick, C. D.; Mukhopadhyay, S.; Pecht, I.; Sheves, M.; Cahen, D.; and Lederman, D. Protein Bioelectronics: A Review of What We Do and Do Not Know. *Rep. Prog. Phys.* **2018**, 81, 26601.

[371] Yates, N. D. J.; Fascione, M. A.; and Parkin, A. Methodologies for "Wiring" Redox Proteins/Enzymes to Electrode Surfaces. *Chem. Eur. J.* **2018**, 24, 12164–12182.

[372] Hitaishi, V. P.; Clement, R.; Bourassin, N.; Baaden, M.; de Poulpiquet, A.; Sacquin-Mora, S.; Ciaccafava, A.; and Lojou, E. Controlling Redox Enzyme Orientation at Planar Electrodes. *Catal.* **2018**, 8, 192.

[373] Mazurenko, I.; Hitaischi, V. P.; and Lojou, E. Recent Advances in Surface Chemistry of Electrodes to Promote Direct Enzymatic Bioelectrocatalysis. *Curr. Opin. Electrochem.* **2020**, 19, 113–121.

[374] Fenter, P.; Cheng, L.; Rihs, S.; Machesky, M.; Bedzyk, M. J.; and Sturchio, N. C. Electrical Double-Layer Structure at the Rutile-Water Interface as Observed in Situ with Small-Period X-Ray Standing Waves. *J. Coll. Interface. Sci.* **2000**, 225, 154–165.

[375] Huang, P.; Pham, T. A.; Galli, G.; and Schwegler, E. Allumina(0001)/Water Interface: Structural Properties and Infrared Spectra from First-Principles Molecular Dynamics Simulations. *J. Phys. Chem. C* **2014**, 118, 8944–8951.

[376] Ning, Y.; Wei, M.; Yu, L.; Yang, F.; Chang, R.; Liu, Z.; Fu, Q.; and Bao, X. Nature of Interface Confinement Effect in Oxide/Metal Catalysts. *J. Phys. Chem. C* **2015**, 119, 27556–27561.

[377] Futera, Z. and English, N. J. Electric-Field Effects on Adsorbed-Water Structural and Dynamical Properties at Rutile- and Anatase-TiO2 Surfaces. *J. Phys. Chem. C* **2016**, 120, 19603–19612.

[378] von Rudorff, G. F.; Jakobsen, R.; Rosso, K. M.; and Blumberger, J. Fast Interconversion of Hydrogen Bonding at the Hematite (001) Liquid Water Interface. *J. Phys. Chem. Lett.* **2016**, 7, 1155–1160.

[379] McBriarty, M. E.; von Rudorff, G. F.; Stubbs, J. E.; Eng, P. J.; Blumberger, J.; and

Rosso, K. M. Dynamic Stabilization of Metal Oxide-Water Interfaces. *J. Am. Chem. Soc.* **2017**, 139, 2581–2584.

[380] Quaranta, V.; Behler, J.; and Hellstrom, M. Structure and Dynamics of the Liquid-Water/Zinc-Oxide Interface from Machine Learning Potential Simulations. *J. Phys. Chem. C* **2019**, 123, 1293–1304.

[381] Siepmann, J. I. and Sprik, M. Influence of Surface Topology and Electrostatic Potential on Water/Electrode Systems. *J. Chem. Phys.* **1995**, 102, 511–524.

[382] Heinz, H.; Jha, K. C.; Luettmer-Strathmann, J.; Farmer, B. L.; and Naik, R. R. Polarization at Metal-Biomolecular Interfaces in Solution. *J. R. Soc. Interface* **2011**, 8, 220–232.

[383] Iori, F. and Corni, S. Including Image Charge Effects in the Molecular Dynamics Simulations of Molecules on Metal Surfaces. *J. Comput. Chem.* **2008**, 29, 1656–1666.

[384] Iori, F.; Di Felice, R.; Molinari, E.; and Corni, S. GoIP: An Atomistic Force-Field to Describe the Interaction of Proteins With Au(111) Surfaces in Water. *J. Comput. Chem.* **2009**, 30, 1465–1476.

[385] Wright, L. B.; Rodger, P. M.; Corni, S.; and Walsh, T. R. GoIP-CHARMM: First-Principles Based Force Fields for the Interaction of Proteins with Au(111) and Au(100). *J. Chem. Theory Comput.* **2013**, 9, 1616–1630.

[386] Wright, L. B.; Rodger, P. M.; Walsh, T. R.; and Corni, S. First-Principle-Based Force Field for the Interaction of Proteins with Au(100)(5x1): An Extension of GolP-CHARMM. *J. Phys. Chem. C* **2013**, 117, 24292–24306.

[387] Wright, L. B.; Merrill, N. A.; Knecht, M. R.; and Walsh, T. R. Structure of Arginine Overlayers at the Aqueous Gold Interface: Implications for Nanoparticle Assembly. *Appl. Mater. Interfaces* **2014**, 6, 10524–10533.

[388] Wright, L. B.; Palafox-Hernandez, J. P.; Rodger, P. M.; Corni, S.; and Walsh, T. R. Facet Selectivity in Gold Binding Peptides: Exploiting Interfacial Water Structure. *Chem. Sci.* **2015**, 6, 5204–5214.

[389] Charchar, P.; Christofferson, A. J.; Todorova, N.; and Yarovsky, I. Understanding and Designing the Gold-Bio Interface: Insights from Simulations. *Small* **2016**, 12, 2395–2418.

[390] Ozboyaci, M.; Kokh, D. B.; Corni, S.; and Wade, R. C. Modeling and Simulation of Protein-Surface Interactions: Achievements and Challenges. *Quart. Rev. Biophys.* **2016**, 49, 1.

[391] Futera, Z. and Blumberger, J. Adsorption of Amino Acids on Gold: Assessing the Accuracy of the GolP-CHARMM Force Field and Parametrization of Au-S Bonds. *J. Chem. Theory Comput.* **2019**, 15, 613–624.

[392] Andreoni, W.; Curioni, A.; and Gronbeck, H. Density Functional Theory Approach to Thiols and Disulfides on Gold Au(111) Surface and Clusters. *Int. J. Quant. Chem.* **2000**, 80, 598–608.

[393] Gronbeck, H.; Curioni, A.; and Andreoni, W. Thiols and Disulfides on the Au(111) Surface: The Headgroup-Gold Interaction. *J. Am. Chem. Soc.* **2000**, 122, 3839–3842.

[394] Xue, Y.; Li, X.; Li, H.; and Xhang, W. Quantifying Thiol-Gold Interactions Towards the Efficient Strength Control. *Nat. Comm.* **2014**, 5, 4348.

[395] Chi, Q.; Ford, M. J.; Halder, A.; Hush, N. S.; Reimers, J. R.; and Ulstrup, J. Sulfur Ligand Mediated Electrochemistry of Gold Surfaces and Nanoparticles: What, How, and Why. *Curr. Opin. Electrochem.* **2017**, 1, 7–15.

[396] Futera, Z. and English, N. J. Influence of External Static and Alternating Electric Fields on Water from Long-Time Non-Equilibrium Ab Initio Molecular Dynamics. *J. Chem. Phys.* **2017**, 147, 31102.

[397] Kuhne, T. D.; Krack, M.; Mohamed, F. R.; and Parrinello, M. Efficient and Accurate Car-Parrinello-like Approach to Born-Oppenheimer Molecular Dynamics. *Phys. Rev. Lett.* **2007**, 98, 66401.

[398] Kuhne, T. D.; Krack, M.; and Parrinello, M. Static and Dynamical Properties of Liquid Water From First Principles by a Novel Car-Parrinello-like Approach. *J. Chem. Theory Comput.* **2009**, 5, 235–241.

[399] Kolafa, J. Time-Reversible Always Stable Predictor-Corrector Method for Molecular Dynamics of Polarizable Molecules. *J. Comput. Chem.* **2004**, 25, 335–342.

[400] Futera, Z.; Tse, J. S.; and English, N. J. Possibility of Realizing Superionic Ice VII in External Electric Fields of Planetary Bodies. *Sci. Adv.* **2020**, 6, eaaz2915.

[401] Futera, Z. and English, N. J. Water Breakup at Fe_2O_3–Hematite/Water Interfaces: Influence of External Electric Fields from Nonequilibrium Ab Initio Molecular Dynamics. *J. Phys. Chem. Lett.* **2021**, 12, 6818–6826.

[402] Futera, Z. and English, N. J. Dielectric Properties of Ice VII under the Influence of Time-Alternating External Electric Fields. *Phys. Chem. Chem. Phys.* **2022**, 24, 56–62.

[403] Dion, M.; Rydberg, H.; Schroder, E.; Langreth, D. C.; and Lundqvist, B. I. Van der Waals Density Functional for General Geometries. *Phys. Rev. Lett.* **2004**, 92(24), 246401.

[404] Roman-Perez, G. and Soler, J. M. Efficient Implementation of a van der Waals Density Functional: Application to Double-Wall Carbon Nanotubes. *Phys. Rev. Lett.* **2009**, 103, 96102.

[405] Klimes, J.; Bowler, D. R.; and Michaelides, A. Chemical Accuracy for the van der Waals Density Functional. *J. Phys.: Condens. Matter* **2010**, 22, 22201.

[406] Bankura, A.; Karmakar, A.; Carnevale, V.; Chandra, A.; and Klein, M. L. Structure, Dynamics, and Spectral Diffusion of Water from First Principles Molecular Dynamics. *J. Phys. Chem. C* **2014**, 118, 29401–29411.

[407] English, N. J. Structural Properties of Liquid Water and Ice Ih form Ab-Initio Molecular Dynamics with a Non-Local Correlation Functional. *Energies* **2015**, 8, 9383–9391.

[408] Gillan, M. J.; Alfe, D.; and Michaelides, A. Perspective: How Good is DFT for Water? *J. Chem. Phys.* **2016**, 144, 130901.

[409] English, N. J. and MacElroy, J. M. D. Hydrogen Bonding and Molecular Mobility in Liquid Water in External Electromagnetic Fields. *J. Chem. Phys.* **2003**, 119, 11806–11813.

[410] Dunaeva, A. N.; Antsyshkin, D. V.; and Kuskov, O. L. Phase Diagram of H2O: Thermodynamic Functions of the Phase Transitions of High-Pressure Ices. *Sol. Sys. Res.* **2010**, 44(3), 202–222.

[411] Millot, M.; Hamel, S.; Rygg, J. R.; Celliers, P. M.; Collins, G. W.; Coppari, F.; Fratanduono, D. E.; Jeanloz, R.; Swift, D. C.; and Eggert, J. H. Experimental Evidence for

Superionic Water Ice Using Shock Compression. *Nat. Phys.* **2018**, 14, 297–302.

[412] Cavazzoni, C.; Chiarotti, G. L.; Scandolo, S.; Tosatti, E.; Bernasconi, M.; and Parrinello, M. Superionic and Metallic States of Water and Ammonia at Giant Planet Conditions. *Science* **1999**, 283, 44–46.

[413] Nettlemann, N.; Helled, R.; Fortney, J. J.; and Redmer, R. New Indication for a Dichotomy in the Interior Structure of Uranus and Neptune from the Application of Modified Shape and Rotation Data. *Planet. Space Sci.* **2013**, 77, 143–151.

[414] Wan, C.; Fiebig, T.; Kelley, S. O.; Treadway, C. R.; Barton, J. K.; and Zewail, A. H. Femtosecond Dynamics of DNA-Mediated Electron Transfer. *Proc. Nat. Acad. Sci.* **1999**, 96, 6014–6019.

[415] He, T.-F.; Guo, L.; Guo, X.; Chang, C.-W.; Wang, L.; and Zhong, D. Femtosecond Dynamics of Short-Range Protein Electron Transfer in Flavodoxin. *Biochem.* **2013**, 52, 9120–9128.

[416] Zalis, S.; Heyda, J.; Sebesta, F.; Winkler, J. R.; Gray, H. B.; and Vlcek, A. Photoinduced Hole Hopping through Tryptophans in Proteins. *Proc. Nat. Acad. Sci.* **2021**, 118(11), 2024627118.

[417] Zheng, D.; Tao, M.; Yu, L.; Liu, X.; Xia, A.; and Wang, J. Ultrafast Photoinduced Electron Transfer in a Photosensitizer Protein. *CCS Chem.* **2022**, 4, 1217–1223.

[418] Yang, J.; Zhang, Y.; Lu, Y.; Wang, L.; Lu, F.; and Zhong, D. Ultrafast Dynamics of Nonequilibrium Short-Range Electron Transfer in Semiquinone Flavodoxin. *J. Phys. Chem. Lett.* **2022**, 13, 3202–3208.

[419] Lu, Y. and Zhong, D. Understanding Short-Range Electron-Transfer Dynamics in Proteins. *J. Phys. Chem. Lett.* **2019**, 10, 346–351.

[420] Lu, Y.; Kundu, M.; and Zhong, D. Effects of Nonequilibrium Fluctuations on Ultrafast Short-Range Electron Transfer Dynamics. *Nat. Comm.* **2020**, 11, 2822.

[421] Woiczikowski, P. B.; Steinbrecher, T.; Kubar, T.; and Elstner, M. Nonadiabatic QM/MM Simulations of Fast Charge Transfer in Escherichia cooli DNA Photolyase. *J. Phys. Chem. B* **2011**, 115, 9846–9863.

[422] Tavernelli, I. Nonadiabatic Molecular Dynamics Simulations: Synergies between Theory and Experiments. *Acc. Chem. Res.* **2015**, 48, 792–800.

[423] Dinpajooh, M.; Martin, D. R.; and Matyushov, D. V. Polarizability of the Active Site of Cytochrome c Reduces the Activation Barrier for Electron Transfer. *Sci. Rep.* **2016**, 6, 28152.

[424] Seyedi, S. and Matyushov, D. V. Ergodicity Breaking of Iron Displacement in Heme Protein. *Soft Matter* **2017**, 13, 8188–8201.

[425] Waskasi, M. M.; Newton, M. D.; and Matyushov, D. V. Impact of Temperature and Non-Gaussian Statistics on Electron Transfer in Donor-Bridge-Acceptor Molecules. *J. Phys. Chem. B* **2017**, 121, 2665–2676.

[426] Seyedi, S. and Matyushov, D. V. Termination of Biological Function at Low Temperature: Glass or Structural Transition? *J. Phys. Chem. Lett.* **2018**, 9, 2359–2366.

[427] Martin, D. R.; Dinpajooh, M.; and Matyushov, D. V. Polarizability of the Active Site in Enzymatic Catalysis: Cytochrome c. *J. Phys. Chem. C* **2019**, 123, 10691–10699.

[428] Matyushov, D. V. Reorganization Energy of Electron Transfer. *Phys. Chem. Chem. Phys.* **2023**.

[429] Terrettaz, S.; Cheng, J.; Miller, C. J.; and Guiles, R. D. Kinetic Parameters for Cytochrome c via Insulated Electrode Voltammetry. *J. Am. Chem. Soc.* **1996**, 118, 7857–7858.

[430] Fedurco, M.; Augustynski, J.; Indiani, C.; Smulevich, G.; Antaliik, M.; Bano, M.; Sedlak, E.; Glascock, M. C.; and Dawson, J. H. Electrochemistry of Unfolded Cytochrome c in Neutral and Acidic Urea Solutions. *J. Am. Chem. Soc.* **2005**, 127, 7638–7646.

[431] Shafiey, H.; Ghourchian, H.; and Mogharrab, N. How Does Reorganization Energy Change Upon Protein Unfolding? Monitoring the Structural Perturbations in the Heme Cavity of Cytochrome c. *Biophys. Chem.* **2008**, 134, 225–231.

[432] Alvarez-Paggi, D.; Zitare, U.; and Murgida, D. H. The Role of Protein Dynamics and Thermal Fluctuations in Regulating Cytochrome c/Cytochrome c Oxidase Electron Transfer. *Biochim. Biophys. Acta* **2014**, 1837, 1196–1207.

[433] Banci, L.; Bertini, I.; Huber, J. G.; Spyroulias, G. A.; and Turano, P. Solution Structure of Reduced Horse Heart Cytochrome c. *J. Biol. Inorg. Chem.* **1999**, 4, 21–31.

[434] Jiang, X.; Futera, Z.; and Blumberger, J. Ergodicity-Breaking in Thermal Biological Electron Transfer? Cytochrome C Revisited. *J. Phys. Chem. B* **2019**, 123, 7588–7598.

[435] Futera, Z.; Jiang, X.; and Blumberger, J. Ergodicity Breaking in Thermal Biological Electron Transfer? Cytochrome C Revisited II. *J. Phys. Chem. B* **2020**, 124, 3336–3342.

[436] Sepunaru, L.; Pecht, I.; Sheves, M.; and Cahen, D. Solid-State Electron Transport across Azurin: From a Temperature-Independent to a Temperature-Activated Mechanism. *J. Am. Chem. Soc.* **2011**, 133, 2421–2423.

[437] Li, W.; Sepunaru, L.; Amdursky, N.; Cohen, S. R.; Pecht, I.; Sheves, M.; and Cahen, D. Temperature and Force Dependence of Nanoscale Electron Transport via the Cu Protein Azurin. *ACS Nano* **2012**, 6(12), 10816–10824.

[438] Artes, J. M.; Diez-Perez, I.; and Gorostiza, P. Transistor-Like Behavior of Single Metalloprotein Junctions. *Nano Lett.* **2012**, 12, 2679–2684.

[439] Yu, X.; Lovrincic, R.; Sepunaru, L.; Li, W.; Vilan, A.; Pecht, I.; Sheves, M.; and Cahen, D. Insights into Solid-State Electron Transport through Proteins from Inelastic Tunneling Spectroscopy: The Case of Azurin. *ACS Nano* **2015**, 9(10), 9955–9963.

[440] Fereiro, J. A.; Porat, G.; Bendikov, T.; Pecht, I.; Sheves, M.; and Cahen, D. Protein Electronics: Chemical Modulation of Contacts Control Energy Level Alignment in Gold-Azurin-Gold Junctions. *J. Am. Chem. Soc.* **2018**, 140, 13317–13326.

[441] Kayser, B.; Fereiro, J. A.; Guo, C.; Cohen, S. R.; Sheves, M.; Pecht, I.; and Cahen, D. Transistor Configuration Yields Energy Level Control in Protein-Based Junctions. *Nanoscale* **2018**, 10, 21712–21720.

[442] Fereiro, J. A.; Bendikov, T.; Pecht, I.; Sheves, M.; and Cahen, D. Protein Binding and Orientation Matter: Bias-Induced Conductance Switching in a Mutated Azurin Junction. *J. Am. Chem. Soc.* **2020**, 142, 19217–19225.

[443] Fereiro, J. A.; Pecht, I.; Sheves, M.; and Cahen, D. Inelastic Electron Tunneling Spectroscopic Analysis of Bias-Induced Structural Changes in a Solid-State Protein Junction.

Small **2021**, 17, 2008218.

[444] King-Smith, R. D. and Vanderbilt, D. Theory of Polarization of Crystalline Solids. *Phys. Rev. B* **1993**, 47(3), 1651–1654.

[445] Wu, H.; Ghaani, M. R.; Futera, Z.; and English, N. J. Effects of Externally Applied Electric Fields on the Manipulation of Solvated-Chignolin Folding: Static- versus Alternating-Field Dichotomy at Play. *J. Phys. Chem. B* **2022**, 126, 376–386.

[446] Hughes, Z. E.; Wright, L. B.; and Walsh, T. Biomolecular Adsorption at Aqueous Silver Interfaces: First-Principles Calculations, Polarizable Force-Field Simulations, and Comparisons with Gold. *Langmuir* **2013**, 29, 13217–13229.

[447] Costa, D.; Savio, L.; and Pradier, C.-M. Adsorption of Amino Acids and Peptides on Metal and Oxide Surfaces in Water Environment: A Synthetic and Prospective Review. *J. Phys. Chem. B* **2016**, 120, 7039–7052.

[448] Schwaminger, S.; Blank-Shim, S. A.; Borkowska-Panek, M.; Anand, P.; Fraga-Garcia, P.; Fink, K.; Wenzel, W.; and Berensmeier, S. Experimental Characterization and Simulation of Amino Acid and Peptide Interactions with Inorganic Materials. *Eng. Life Sci.* **2018**, 18, 84–100.

[449] Malvankar, N. S.; Vargas, M.; Nevin, K.; Tremblay, P.-L.; Evans-Lutterodt, K.; Nykypanchuk, D.; Martz, E.; Tuominen, M. T.; and Lovley, D. R. Structural Basis for Metallic-Like Conductivity in Microbial Nanowires. *mBio* **2015**, 6.

[450] Breuer, M.; Rosso, K. M.; and Blumberger, J. Electron Flow in Multiheme Bacterial Cytochromes is a Balancing Act Between Heme Electroonic Interaction and Redox Potentials. *Proc. Nat. Acad. Sci.* **2014**, 111(2), 611–616.

[451] Park, J.-S.; Ohmura, T.; Kano, K.; Sagara, T.; Niki, K.; Kyogoku, Y.; and Akutsu, H. Regulation of the Redox Order of Four Hemes by pH in Cytochrome c3 from D. vulgaris Miyazaki F. *Biochim. Biophys. Acta* **1996**, 1293, 45–54.

[452] Harada, E.; Kumagai, J.; Ozawa, K.; Imabayashi, S.; Tsapin, A. S.; Healson, K. H.; Meyer, T. E.; Cusanovich, M. A.; and Akutsu, H. A Directional Electron Transfer Regulator Based on Heme-Chain Architecture in the Small Tetraheme Cytochrome c From Shewanella Oneidensis. *FEBS Lett.* **2002**, 532, 333–337.

[453] Fonseca, B. M.; Saraiva, I. H.; Paquete, C. M.; Soares, C. M.; Pacheco, I.; Salgueiro, C. A.; and Louro, R. O. The Tetraheme Cytochrome from Shewanella oneidensis MR-1 Shows Thermodynamic Bias for Functional Specificity of the Hemes. *J. Biol. Inorg. Chem.* **2009**, 14, 375–385.

[454] Futera, Z. Amino-acid Interactions with the Au(111) Surface: Adsorption, Band Alignment, and Interfacial Electronic Coupling. *Phys. Chem. Chem. Phys.* **2021**, 23, 10257–10266.

[455] Andersen, J. E. T.; Olesen, K. G.; Danilov, A. I.; Foverskov, C. E.; Moller, P.; and Ulstrup, J. Covalently Immobilised Cytochrome c Imaged by in Situ Scanning Tunneling Microscopy. *Bioelectrochem. Bioenerg.* **1997**, 44, 57–63.

[456] Bonanni, B.; Bizzarri, A. R.; and Cannistraro, S. Optimized Biorecognition of Cytochrome c 551 and Azurin Immobilized on Thiol-Terminated Monolayers Assembeld on Au(111) Substrates. *J. Phys. Chem. B* **2006**, 110, 14574–14580.

[457] Onoda, A.; Taniguchi, T.; Inoue, N.; Kamii, A.; and Hayashi, T. Anchoring Cytochrome b562 on a Gold Nanoparticle by a Heme-Heme Pocket Interaction. *Eur. J. Inorg. Chem.* **2016**, pages 3454–3459.

[458] Bizzarri, A. R. Topological and Dynamical Properties of Azurin Anchored to a Gold Substrate as Investigated by Molecular Dynamics Simulation. *Biophys. Chem.* **2006**, 122, 206–214.

[459] Corni, S. The Reorganization Energy of Azurin in Bulk Solution and in the Electrochemical Scanning Tunneling Microscopy Setup. *J. Phys. Chem. B* **2005**, 109, 3423–3430.

[460] Yoon, J.; Lee, T.; and Choi, J.-W. Development of Bioelectronic Devices Using Bionanohybrid Materials for Biocomputation System. *Micromachines* **2019**, 10, 347.

[461] Bayda, S.; Adeel, M.; Tuccinardi, T.; Cordani, m.; and Rizzolio, F. The History of Nanoscience and Nanotechnology From Chemical-Physical Applications of Nanomedicine. *Molec* **2020**, 25, 112.

[462] Blumberger, J. and Sprik, M. Ab Initio Molecular Dynamics Simulation of the Aqueous Ru2+/Ru3+ Redox Reactions: The Marcus Perspective. *J. Phys. Chem. B* **2005**, 109, 6793–6804.

[463] Kuharski, R. A.; Bader, J. S.; Chandler, D.; Sprik, M.; Klein, M.; and Impey, R. W. Molecular Model for Aqueous Ferrous-Ferric Electron Transfer. *J. Chem. Phys.* **1988**, 89(5), 3248–3257.

[464] Takagi, H. and Swaddle, T. W. The Aqueous Hexacyanoferrate(II/III) Self-Exchange Reaction at High Pressure. *Inorg. Chem.* **1992**, 31, 4669–4673.

[465] Rosso, K. M.; Smith, D. M. A.; and Dupuis, M. Aspects of Aqueous Iron and Manganese (II/III) Self-Exchange Electron Transfer Reactions. *J. Phys. Chem. A* **2004**, 108, 5242–5248.

[466] Ross, M.; Andersen, A.; Fox, Z. W.; Hong, K.; Lee, J.-H.; Cordones, A.; March, A. M.; Doumy, G.; Southworth, S. H.; Marcus, M. A.; Schoenlein, R. W.; Mukamel, S.; Govind, N.; and Khalil, M. Comprehensive Experimental and Computational Spectroscopic Study of Hexacyanoferrate Complexes in Water: From Infrared to X-Ray Wavelengths. *J. Phys. Chem. B* **2018**, 122, 5075–5086.

[467] Buckingham, M. A.; Hammoud, S.; Li, H.; Beale, C. J.; Sengel, j. T.; and Aldous, L. A Fundamental Study of the Thermoelectrochemistry of Ferricyanine/ferrocyanide: Cation, Concentration, Ratio, and Heterogeneous and Homogeneous Electrocatalysis Effects in Thermogalvanic Cells. *Sustain. Energy Fuels* **2020**, 4, 3388–3399.

[468] Nakagawa, I. and Shimanouchi, T. Infrared Spectroscopic Study on the Coordination Bond II Infrared Spectra of Octahedral Metal Cyanide Complexes. *Spectroch. Acta* **1962**, 18, 101–113.

[469] Klyuev, Y. A. Vibrational Spectra of Crystalline Potassium Ferri- and Ferrocyanide. *Zh. Prikl. Spektr.* **1965**, 3(1), 42–48.

[470] Dunsmuir, J. T. R. and Lane, A. P. The Infrared Spectra (40-3000 cm-1) of Potassium Hexacyanoferrate and Potassium Hexacyanocobaltate. *J. Chem. Soc. A* **1971**, 776, 776–780.

[471] Savatinova, I. and Uzunova, J. Vibrational Spectrum of the Anion [Fe(CN)6]4- in Ferro-

electric K4Fe(CN)6.3H2O. *Spectr. Lett.* **1977**, 10, 105–113.

[472] Seidel, R.; Thurmer, S.; Moens, J.; Geerlings, P.; Blumberger, J.; and Winter, B. Valence Photoemission Spectra of Aqueous Fe2+/3+ and [Fe(CN)6]4-/3- and Their Interpretation by DFT Calculations. *J. Phys. Chem. B* **2011**, 115, 11671–11677.

[473] Zahl, A.; van Eldik, R.; and Swaddle, T. W. Cation-Independent Electron Transfer Between Ferricyanide and Ferrocyaninide Ions in Aqueous Solution. *Inorg. Chem.* **2002**, 41, 757–764.

[474] Gangemi, C. M. A.; Pappalardo, A.; and Sfrazzetto, G. T. Assembling of Supramolecular Capsules with Resorcin[4]arene and Calix[4]arene Building Blocks. *Curr. Org. Chem.* **2015**, 19, 2281–2308.

[475] Pinalli, R.; Dalcanale, E.; Ugozzoli, F.; and Massera, C. Resorcinarene-based Cavitands as Building Blocks for Crystal Engineering. *CrystEngComm* **2016**, 18, 5788–5802.

[476] Payne, D. T.; Webre, W. A.; Matsushita, Y.; Zhu, N.; Futera, Z.; Labuta, J.; Jevasuwan, W.; Fukata, N.; Fossey, J. S.; D'Souza, F.; Ariga, K.; Schmitt, W.; and Hill, J. P. Multimodal Switching of a Redox-Active Macrocycle. *Nat. Comm.* **2019**, 10, 1007.

[477] MacGillivray, L. R. and Atwood, J. L. Cavity-Containing Materials Based Upon Resorcin[4]arenes by Discovery and Design. *J. Solid State Chem.* **2000**, 152, 199–210.

[478] Purse, B. W. and Rebek, J. J. Functional Cavitands: Chemical Reactivity in Structured Environments. *Proc. Natl. Acad. Sci. U.S.A.* **2005**, 102, 10777–10782.

[479] Kulikov, O. V.; Daschbach, M. M.; Yamnitz, C. R.; Rath, N.; and Gokel, G. W. Self-assembled Cogged Hexameric Nanotubes Formed From Pyrogallol[4]arenes with a Unique Branched Side Chain. *Chem. Commun.* **2009**, pages 7479–7499.

[480] Pochorovski, I. and Diederich, F. Development of Redox-Switchable Resorcin[4]arene Cavitands. *ACC Chem. Res.* **2014**, 47, 2096–2105.

[481] Patil, R. S.; Zhang, C.; and Attwood, J. L. Process Development for Separation of Conformers from Derivatives of Resorcin[4]arenes and Pyrogallol[4]arenes. *Chem. Eur. J.* **2016**, 22, 15202–15207.

[482] Payne, D. T.; Labuta, J.; Futera, Z.; Brezina, V.; Hanykova, L.; Chahal, M. K.; and Hill, J. P. Molecular Rotor Based on an Oxidized Resorcinarene. *Org. Chem. Front.* **2022**, 9, 39.

[483] Hill, J. P.; Karr, P. A.; Zuniga Uy, R. A.; Subbaiyan, N. K.; Futera, Z.; Ariga, K.; Ishihara, S.; Labuta, J.; and D'Souza, F. Analyte Interactions with Oxoporphyrinogen Derivatives: Computational Aspects. *Curr. Org. Chem.* **2022**, 26, 580–595.

[484] Himpsel, F. J.; Knapp, J. A.; VanVechten, J. A.; and Eastman, D. E. Quantum Photoyield of Diamond(111) - A Stable Negative-Affinity Emitter. *Phys. Rev. B* **1979**, 20(2), 624–627.

[485] Cui, J. B.; Ristein, J.; and Ley, L. Electron Affinity of the Bare and Hydrogen Covered Single Crystal Diamond (111) Surface. *Phys. Rev. Lett.* **1998**, 81(2), 429–432.

[486] Maier, F.; Riedel, M.; Mantel, B.; Ristein, J.; and Ley, L. Origin of Surface Conductivity in Diamond. *Phys. Rev. Lett.* **2000**, 85(16), 3472–3475.

[487] Ekimov, E. A.; Sidorov, V. A.; Bauer, E. D.; Mel'nik, N. N.; Curro, N. J.; Thompson, J. D.; and Stishov, S. M. Superconductivity in Diamond. *Nature* **2004**, 428, 542–545.

[488] Takano, Y.; Takenouchi, T.; Ischii, S.; Ueda, S.; Okutsu, T.; Sakaguchi, I.; Umezawa, H.; Kawarada, H.; and Tachiki, M. Superconducting Properties of Homoepitaxial CVD Diamond. *Diam. Rel. Mater.* **2007**, 16, 911–914.

[489] Kawano, A.; Ishiwata, H.; Iriyama, S.; Okada, R.; Yamaguchi, T.; Takano, Y.; and Kawarada, H. Superconductor-to-insulator in Boron-Doped Diamond Films Grown Using Chemical Vapor Deposition. *Phys. Rev. B* **2010**, 82, 85318.

[490] Fujishima, A.; Einaga, Y.; Rao, T. N.; and Tryk, D. A., editors. *Diamond Electrochemistry*. BKC, Tokyo, **2005**.

[491] Panizza, M.; Brillas, E.; and Comninellis, C. Application of Boron-Doped Diamond Electrodes for Wastewater Treatment. *J. Environ. Eng. Manage.* **2008**, 18(3), 139–153.

[492] Einaga, Y. Diamond Electrodes for Electrocheical Analysis. *J. Appl. Electrochem.* **2010**, 40, 1807–1816.

[493] Waldvogel, S. R. and Elsler, B. Electrochemical Synthesis on Boron-Doped Diamond. *Electrochim. Acta* **2012**, 82, 434–443.

[494] Yagi, I.; Notsu, H.; Kondo, T.; Tryk, D. A.; and Fujishima, A. Electrochemical Selectivity for Redox Systems at Oxygen-Terminated Diamond Electrodes. *J. Electroanal. Chem.* **1999**, 473, 173–178.

[495] Pleskov, Y. V. Electrochemistry of Diamond: A Review. *Russ. J. Electrochem.* **2002**, 38(12), 1275–1291.

[496] Panizza, M. and Cerisola, G. Application of Diamond Electrodes to Electrochemical Processes. *Electrochim. Acta* **2005**, 51, 191–199.

[497] Gelderman, K.; Lee, L.; and Donne, W. Flat-Band Potential of a Semiconductor: Using the Mott-Schottky Equation. *J. Chem. Edu.* **2007**, 84(4), 685–688.

[498] Tateyama, Y.; Futera, Z.; Ootani, Y.; Iizuka, S.; and Anh, L. T. Computational Aspects of Surface and Interface of BDD Electrode. In Einaga, Y., editor, *Diamond Electrodes*, pages 57–71. Springer, Singapore, **2022**.

[499] Agnihotri, A. S.; Varghese, A.; and M, N. Transition Metal Oxides in Electrochemical and Bio Sensing: A State-of-art Review. *Appl. Surf. Sci. Adv.* **2021**, 4, 100072.

[500] Fujishima, A. and Honda, K. Electrochemical Photolysis of Water at a Semiconductor Electrode. *Nature* **1972**, 238, 37–38.

[501] Diebold, U. The Surface Science of Titanium Dioxide. *Surf. Sci. Rep.* **2003**, 48, 53–229.

[502] Henderson, M. A. A Surface Science Perspective on TiO2 Photocatalysis. *Surf. Sci. Rep.* **2011**, 66, 185–297.

[503] Futera, Z. and English, N. J. Oscillating Electric-Field Effects on Adsorbed-Water at Rutile- and Anatase-TiO2 Surfaces. *J. Chem. Phys.* **2016**, 145, 204706.

[504] van Duin, A. C. T.; Dasgupta, S.; Lorant, F.; and Goddard, W. A. I. ReaxFF: A Reactive Force Field for Hydrocarbons. *J. Phys. Chem. A* **2001**, 105, 9396–9409.

[505] Kim, S.-Y.; Kumar, N.; Persson, P.; Sofo, J.; van Duin, A. C. T.; and Kubicki, J. D. Development of a ReaxFF Reactive Force Field for Titanium Dioxide / Water Systems. *Langmuir* **2013**, 29, 7838–7846.

[506] Futera, Z. and English, N. J. Exploring Rutile (110) and Anatase (101) TiO_2 Water

Interfaces by Reactive Force-Field Simulations. *J. Phys. Chem. C* **2017**, 121, 6701–6711.

[507] Rappe, A. K.; Casewit, C. J.; Colwell, K. S.; Goddard, W. A. I.; and Skiff, W. M. UFF, a Full Periodic Table Force Field for Molecular Mechanics and Molecular Dynamics Simulations. *J. Am. Chem. Soc.* **1992**, 114, 10024–10035.

[508] Nakano, A. Parallel Multilevel Preconditioned Conjugate-Gradient Approach to Variable-Charge Molecular Dynamics. *Comp. Phys. Comm.* **1997**, 104, 59–69.

[509] Glasscock, J. A.; Barnes, P. R. F.; Plumb, I. C.; and Savvides, N. Enhancement of Photoelectrochemical Hydrogen Production from Hematite Thin Films by the Introduction of Ti and Si. *J. Phys. Chem. C* **2007**, 111, 16477–16488.

[510] Hu, Y.-S.; Kleiman-Shwarsctein, A.; Forman, A. J.; Hazen, D.; Park, J.-N.; and McFarland, E. W. Pt-Doped alpha-Fe2O3 Thin Films Active for Photoelectrochemical Water Splitting. *Chem. Mater.* **2008**, 20, 3803–3805.

[511] English, N. J.; Rahman, M.; Wadnerkar, N.; and MacElroy, J. M. D. Photo-Active and Dynamical Properties of Hematite (Fe2O3)-Water Interfaces: An Experimental and Theoretical Study. *Phys. Chem. Chem. Phys.* **2014**, 16, 14445–14454.

[512] Tamirat, A. G.; Rick, J.; Dubale, A. A.; Su, W.-N.; and Hwang, B.-J. Using Hematite for Photoelectrochemical Water Splitting: A Review of Current Progress and Challenges. *Nanoscale Horiz.* **2016**, 1, 243–267.

[513] Rosso, K. M.; Smith, D. M. A.; and Dupuis, M. An Ab Initio Model of Electron Transport in Hematite (a-Fe2O3) Basal Planes. *J. Chem. Phys.* **2003**, 118, 6455–6466.

[514] von Rudorff, G. F.; Jakobsen, R.; Rosso, K. M.; and Blumberger, J. Hematite(001)-Liquid Water Interface from Hybrid Density Functional-Based Molecular Dynamics. *J. Phys.: Condens. Matter* **2016**, 28, 394001.

[515] Guthrie, M.; Boehler, R.; Molaison, J. J.; Haberl, B.; dos Santos, A. M.; and Tulk, C. Structure and Disorder in Ice VII on the Approach to Hydrogen-Bond Symmetrization. *Phys. Rev. B* **2019**, 99, 184112.

[516] Gu, Y.; Zhu, X.-L.; Jiang, L.; Cao, J.-W.; Qin, X.-L.; Yao, S.-K.; and Zhang, P. Comparative Analysis of Hydrogen Bond Vibrations in Ice VIII and VII. *J. Phys. Chem. C* **2019**, 123, 14880–14883.

[517] Shin, D.; Hwang, J.; and Jhe, W. Ice-VII-like Molecular Structure of Ambient Water Nanomeniscus. *Nat. Comm.* **2019**, 10, 286.

[518] Millot, M.; Coppari, F.; Rygg, J. R.; Barrios, A. C.; Hamel, S.; Swift, D. C.; and Eggert, J. H. Nanosecond X-Ray Diffraction of Shock-Compressed Superionic Water Ice. *Nature* **2019**, 569, 251–255.

[519] Yamane, R.; Komatsu, K.; Maynard-Casely, H. E.; Lee, S.; Booth, N.; and Kagi, H. Search for a Ferroelectrically Ordered Form of Ice VII by Neutron Diffraction under High Pressure and High Electric Field. *Phys. Rev. B* **2019**, 99, 174201.

[520] Zhu, W.; Huang, Y.; Zhu, C.; Wu, H.-H.; Wang, L.; Bai, J.; Yang, J.; Francisco, J. S.; Zhao, J.; Yuan, L.-F.; and Zeng, X. C. Room Temperature Electrofreezing of Water Yields a Missing Dense Ice Phase in the Phase Diagram. *Nat. Comm.* **2019**, 10, 1925.

[521] Futera, Z. and English, N. J. Pressure Dependence of Structural Properties of Ice VII: An Ab Initio Molecular-Dynamics Study. *J. Chem. Phys.* **2018**, 148, 204505.

[522] Noguchi, N. and Okuchi, T. Self-Diffusion of Protons in H2O Ice VII at High Pressures: Anomaly Around 10 GPa. *J. Chem. Phys.* **2016**, 144, 234503.

Article reprints

A double-QM/MM method for investigating donor–acceptor electron-transfer reactions in solution

Author contributions:

Zdenek Futera:	Methodology, software development, calculations, visualization, manuscript preparation
Keitaro Sodeyama:	Metholology, supervision, manuscript preparation
Jaroslav V. Burda:	Methodology, supervision
Yasuaki Einaga:	Funding acquisition
Yoshitaka Tateyama:	Conceptualization, supervision, manuscript preparation

Citation:

Phys. Chem. Chem. Phys. 16, 19530–19539 (2014)

DOI: 10.1039/c4cp020307b

Impact factor (2014): 4.62

Electronic Couplings for Charge Transfer across Molecule/Metal and Molecule/Semiconductor Interfaces: Performance of the Projector Operator-Based Diabatization Approach

Author contributions:

Zdenek Futera:	Conceptualization, software development, calculations, analyses, visualization, manuscript preparation
Jochen Blumberger:	Conceptualization, supervision, manuscript preparation

Citation:

J. Phys. Chem. C 121, 19677–19689 (2017)

DOI: 10.1021/acs.jpcc.7b06566

Impact factor (2017): 4.48

Erratum:

J. Phys. Chem. C 126, 3301–3303 (2022)

DOI: 10.1021/acs.jpcc.2c00450

Impact factor (2022): 4.13

Adsorption of Amino Acids on Gold: Assessing the Accuracy of the GolP-CHARMM Force Field and Parametrization of Au−S Bonds

Author contributions:

Zdenek Futera:	Conceptualization, calculations, analyses, visualization, manuscript preparation
Jochen Blumberger:	Conceptualization, supervision, manuscript preparation

Citation:

J. Chem. Theory Comput. 15, 613–624 (2019)

DOI: 10.1021/acs.jctc.8b00992

Impact factor (2019): 5.01

Influence of External Static and Alternating Electric Fields on Water from Long-Time Non-Equilibrium Ab Initio Molecular Dynamics

Author contributions:

Zdenek Futera:	Conceptualization, calculations, analyses, visualization, manuscript preparation
Niall J. English:	Conceptualization, supervision, funding acquisition

Citation:

J. Chem. Phys. 147, 031102 (2017)

DOI: 10.1063/1.4994694

Impact factor (2017): 2.80

Ergodicity-Breaking in Thermal Biological Electron Transfer? Cytochrome C Revisited

Author contributions:

Xiuyun Jiang:	MD simulations, QM/MM calculations, visualization, analyses, manuscript preparation
Zdenek Futera:	PMM calculations, analyses, manuscript preparation
Jochen Blumberger:	Conceptualization, supervision, funding acquisition, manuscript preparation

Citation:

J. Phys. Chem. B 123, 7588–7598 (2019)

DOI: 10.1021/acs.jpcb.9b05253

Impact factor (2019): 2.92

Cysteine Linkages Accelerate Electron Flow through Tetra-Heme Protein STC

Author contributions:

Xiuyun Jiang:	MD simulations, FODFT calculations, visualization, analyses, manuscript preparation
Zdenek Futera:	POD calculations, analyses, manuscript preparation
Md. Ehesan Ali:	MD simulations
Fruzsina Gajdos:	Software development, coupling calculations
Guido F. von Rudorff:	Software development, current calculations
Antoine Carof:	Software development, supervision
Marian Breuer:	Conceptualization, supervision, QM/MM calculations
Jochen Blumberger:	Conceptualization, supervision, funding acquisition, manuscript preparation

Citation:

J. Am. Chem. Soc. 139, 17237–17240 (2017)

DOI: 10.1021/jacs.7b08831

Impact factor (2017): 13.86

Erratum:

J. Am. Chem. Soc. 144, 7010–7012 (2022)

DOI: 10.1021/jacs.2c02709

Impact factor (2022): 16.38

Amino-Acid Interactions with the Au(111) Surface: Adsorption, Band Alignment, and Interfacial Electronic Coupling

Author contributions:

Zdenek Futera:	Conceptualization, methodology, calculations, visualization, manuscript preparation

Citation:

Phys. Chem. Chem. Phys. 23, 10257–10266 (2021)

DOI: 10.1039/d1cp00218j

Impact factor (2021): 3.60

Adsorption of Amino Acids at the Gold/Aqueous Interface: Effect of an External Electric Field

Author contributions:

Denys Biriukov:	Caclulations, analyses, visualization, manuscript preparation
Zdenek Futera:	Conceptualization, supervision, manuscript preparation

Citation:

J. Phys. Chem. C 125, 7856–7867 (2021)

DOI: 10.1021/acs.jpcc.0c11248

Impact factor (2017): 4.13

Reorganization Free Energy of Copper Proteins in Solution, in Vacuum, and on Metal Surfaces

Author contributions:

O. Vilhelmiina Kontkanen:	QM/MM calculations, analyses, visualization, manuscript preparation
Denys Biriukov:	MD simulations, analyses, visualization, manuscript preparation
Zdenek Futera	Conceptualization, supervision, funding acquisition, manuscript preparation

Citation:

J. Chem. Phys. 156, 175101 (2022)

DOI: 10.1063/5.0085141

Impact factor (2022): 3.49

Coherent Electron Transport across a 3 nm Bioelectronic Junction Made of Multi-Heme Proteins

Author contributions:

Zdenek Futera:	DFT calculations, current modeling, analyses, visualization, manuscript preparation
Ichiro Ide:	UPS measurements
Ben Kayser:	Current measurements
Kavita Garg:	Current measurements
Xiuyun Jiang:	Current modeling
Jessica H. van Wonderen:	Protein-structure preparation
Julea N. Butt:	Conceptualization, supervision
Hisao Ishii:	Conceptualization, supervision
Israel Pecht:	Conceptualization, supervision
Mordechai Sheves:	Conceptualizatoin, supervision
David Cahen:	Conceptualization, supervision
Jochen Blumberger:	Conceptualization, supervision, funding acquisition, manuscript preparation

Citation:

J. Phys. Chem. Lett. 11, 9766–9774 (2020)

DOI: 10.1021/acs.jpclett.0c02686

Impact factor (2020): 6.21

Multimodal Switching of a Redox-Active Macrocycle

Author contributions:

Daniel T. Payne:	Synthesis, NMR measurements, analyses, manuscript preparation
Whitney A. Webre:	Electrochemical analyses
Yoshitaka Matsushita:	X-ray diffraction, structure determination
Nianyong Zhu:	X-ray diffraction measurements, structure determination
Zdeněk Futera:	MD simulations, DFT calculations
Jan Labuta:	Conceptualization, NMR measurements, analyses, manuscript preparation
Wipakorn Jevasuwan:	ESR data analyses
Naoki Fukata:	ESR data analyses
John S. Fossey:	Conceptualization, supervision
Francis D'Souza:	Electrochemical analyses, supervision
Katsuhiko Ariga:	Supervision, funding acquisition
Wolfgang Schmitt:	X-ray diffraction measurements, supervision
Jonathan P. Hill:	Conceptualization, supervision, manuscript preparation, funding acquisition

Citation:

Nat. Commun. 10, 1007 (2019)

DOI: 10.1038/s41467-019-08978-5

Impact factor (2019): 11.88

First Principles Calculation Study on Surfaces and Water Interfaces of Boron-Doped Diamond

Author contributions:

Zdenek Futera:	DFT calculations, analyses, visualization, manuscript preparation
Takeshi Watanabe:	Experimental measurements
Yasuaki Einaga:	Conceptualization, funding acquisition
Yoshitaka Tateyama:	Conceptualization, supervision, manuscript preparation

Citation:

J. Phys. Chem. C 118, 22040–22052 (2014)

DOI: 10.1021/jp506046m

Impact factor (2014): 5.01

Water Breakup at Fe_2O_3−Hematite/Water Interfaces: Influence of External Electric Fields from Nonequilibrium Ab Initio Molecular Dynamics

Author contributions:

Zdenek Futera:	DFT simulations, analyses, visualization, manuscript preparation
Niall J. English:	Conceptualization, supervision, funding acquisition, manuscript preparation

Citation:

J. Phys. Chem. Lett. 12, 6818–6826 (2021)

DOI: 10.1021/acs.jpclett.1c01479

Impact factor (2021): 6.89

Possibility of Realizing Superionic Ice VII in External Electric Fields of Planetary Bodies

Author contributions:

Zdenek Futera:	MD simulations, analyses, visualization, manuscript preparation
John S. Tse:	Conceptualization, manuscript preparation
Niall J. English:	Conceptualization, supervision, funding acquisition, manuscript preparation

Citation:

Sci. Adv. 6, eaaz2915 (2020)

DOI: 10.1126/sciadv.aaz2915

Impact factor (2020): 13.93